Influence of the Kuroshio Large Meander on the Climate around Japan Using a Regional Climate Model

January 2016

Kazuyo MURAZAKI

Influence of the Kuroshio Large Meander on the Climate around Japan Using a Regional Climate Model

A Dissertation Submitted to
the Graduate School of Life and Environmental Sciences,
the University of Tsukuba
in Partial Fulfillment of the Requirements
for the Degree of Doctor of Environmental Studies
(Doctoral Program in Sustainable Environmental Studies)

Kazuyo MURAZAKI

Table of Contents

Abstract

As a global warming problem becomes apparent in recent years, detailed regional information about climate variation around Japan is required from the various quarters such as water resources, flood control, renewable energy and agricultural production.

Kuroshio, a western boundary warm current that carries heat in large quantities from the equatorial western Pacific Ocean to Japan, is an important factor influencing the atmospheric phenomena such as boundary layer stability, convection, cyclone activity surrounding Japan. However, thus far, research has focused primarily on the cold season, and the effects of the Kuroshio large meander (LM) on climate throughout the year have not been studied enough since turbulent heat flux from the ocean is relatively weak in the warmer season.

In order to present the more accurate predictions of climate change in the Japanese region, investigation of the influence of the Kuroshio LM on the regional climate in each season and the understanding the mechanism are essential. Therefore, we performed a 20-year numerical experiment using a high-resolution North Pacific Ocean general circulation model (NPOGCM) and a 20 km-resolution regional climate model (RCM20) to clarify the detailed impact of the Kuroshio LM on the climate around Japan.

First, a 26-year integration using the RCM20 nested within Japanese 25-year Reanalysis (JRA-25) was conducted to obtain downscaled climate data around Japan. We confirmed the reproducibility of monthly mean precipitation and the daily precipitation frequency were significantly well. We also performed a one-year sea surface temperature (SST) sensitivity experiment to investigate the atmospheric dependency of the SST resolution. Furthermore, two kinds of 10-year integration were simulated using a coupled atmosphere-ocean regional climate model (CRCM) to project climate change around Japan with more sophisticated

atmosphere-ocean interaction. The results indicate that the upgrade to the resolution of the SST is influences on the climate around Japan but the elaboration from one-way to two-way does not necessarily improve the reproducibility of SST in the entire model area.

Finally, using RCM20 and NPOGCM, a long-term numerical experiment was conducted to quantitatively estimate the impact of the Kuroshio LM. The results showed NPOGCM reproduced the two primary quasi-stationary states, straight path (SP) and LM, although the periods during which each state prevailed differed from those indicated by the observational data. Using the simulated SST result as a boundary condition, a 20-year RCM20 experiment (OGCM-run) over the period 1985–2004 was conducted. To remove the climate change factors except the SST as much as possible, the result was compared with a control run (JRA-run) which used coarse SST dataset as a boundary condition.

An 8-year composite analysis of the atmospheric circulations of the RCM20 simulation for the Kuroshio LM and SP showed that in every seasons, the cold SST pool caused substantial decreases in the upward surface turbulent heat flux, the frequency of precipitation, and the frequency of steep horizontal gradients in equivalent potential temperature (EPT) over the ocean. The difference in the rate of frequency change of high intensity rainfall events between the OGCM-run and the JRA-run around the cold SST was approximately 30-35 % for summer and 20-25 % for winter.

We also investigated the mechanism of how the cold pool influences neighboring convection activity. The result indicates that the cold SST pool has two distinct effects on atmospheric convection and rainfall frequency.

First is atmospheric properties change, such as EPT, as a result of decreases in latent and sensible heat fluxes. A decreasing vertical gradient in EPT over the cold SST pool creates increased atmospheric stability in the lower boundary layer, and a decreasing the frequency of

horizontal gradient of EPT at the northern edge of the cold pool suggests that the frequency of active weather fronts decreases there.

Second is moisture flux change as a result of increase in sea level pressure (SLP) on the cold SST pool. The increase in SLP causes a divergent area over the cold SST pool and thereby changes surface wind strength via the pressure adjustment mechanism. Change of moisture flux occurring as a consequence of wind and evaporation has an influence on the rainfall frequency in the domain away from the cold SST pool. In winter, the high atmospheric pressure anomaly due to the cold SST pool moves to the lee side of the seasonal wind. The change in wind is strengthened in the same direction as a seasonal wind and is offset in the opposite direction. This result is consistent with the preceding studies.

Conversely, this study showed that the influence of the cold pool area was extended to Kanto on the Tokai district coast and the lee side of the periodic wind in summer, which has been scarcely investigated thus far. Our results suggest the possibility that the occurrence frequency of precipitation also changes in the warmer season as a perspective of the SST variation between the Kuroshio LM and SP.

There were also significant changes in monthly averaged surface temperature and the monthly amount of precipitation in the coastal region on the Pacific Ocean side of Japan, which were sometimes beyond the range of a normal year. This suggests that the change in the Kuroshio path might have the important information in the seasonal weather forecasting.

This research indicated that the cold SST pool caused by the Kuroshio LM influences on atmospheric convection around Japan not only in winter but also in other seasons. In addition, the research suggested that the two factors, EPT and SLP, have important roles for the mechanism to cause the change. These results will contribute to the studies of regional climate system around Japan such as the interaction between the Kuroshio and atmosphere.

List of Figures

List of Tables

CHAPTER 1 Introduction

1.1 Definition of "regional climate" and approach of modeling

"Regional climate" means the climate that is inherent to the area from several km to 1,000 km scale. It is activated by external meso-scale forcings such as topography, a shoreline, sea surface temperature (SST), a lake, vegetation, soil and the urbanization. In contrast, "global climate" is a climate influenced from the phenomenon of the large-scale atmosphere more than the scale of 1000 km such as westerly jet, Asian monsoon and Hadley circulation (Yoshino 1968). The main external forcings are radiation, aerosol, a contrast between continent and ocean and large-scale ocean variation including El Niño-Southern Oscillation (ENSO).

As a global warming problem become obvious, reality grasp of global warming and decision of the countermeasure has been indispensable according to Intergovernmental Panel on Climate Change (IPCC) report (Solomon et al. 2007). Experiments of the global warming prediction using general circulation models (GCMs) came to be conducted as a document with scientific grounds necessary for the judgment materials. The GCMs have adopted various processes and have been used for not only the global climate change prediction but also studies of mechanism of climate systems. For example, global atmospheric model, ocean model, aerosol model and ozone model are coupled in Meteorological Research Institute – Earth System Model (MRI-ESM). In addition to that, the ESM is taking into account various physical process such as land surface process and carbon cycle (Yukimoto et al. 2011).

However, there is a limit of computer performances and resources to conduct long-term numerical experiments with more detailed scale. Dynamical downscaling is one of the methods to obtain finer resolution data from the coarse data of GCM output or re-analysis data by means of using a nesting regional climate model (RCM). In this method, to investigate more detailed climate changes, large-scale climate changes are responsible for the GCM, and focused only a certain specific region of interest by performing in nested the RCM.

The technique to perform nesting of a regional model in a GCM has been already adopted early in the field of the weather forecast. Giorgi and Bites (1989) applied this technique to several 10 days integration on the western United States for the first time. After that, dynamical downscaling had been used worldwide, for example, in the Europa (Christensen et al. 1998), Oceania (Walsh and McGregor 1995) and Asia (Liu et al. 1994; Hirakuchi and Giorgi 1995; Kato et al. 1999; Kida 1991; Sasaki et al. 1995).

While, there are two points that should be noted when RCMs are used for the dynamical downscaling. First, when the result on which GCM depend has the bias and the trend, nesting RCM cannot correct it, and a bad result is obtained (Giorge and Marinucci 1996; Solomon et al. 2007). That is, though RCM can improve the predictive value by the factor of the meso-scale forcings, if the accuracy of the boundary condition becoming a precondition is not guaranteed, reliability of downscaling result would lower.

Second, there is a problem of uncertainty of inhering in RCM. Even if the boundary condition is the observation value, it is impossible that an area model reproduces the climate of the past perfectly, since the results depend how to deal with discontinuous portion near the boundary, internal variability of the RCM (Alexandru et al. 2007). In addition a result would vary according to the difference in parameterization scheme or numerical computation scheme between RCMs even if the resolutions are the same (Ishizaki et al. 2012).

Therefore, the improvement of the model and development of reduction technique of the uncertainty have been still progress. Nevertheless, RCMs are still useful tools for not only the global climate change experiment but also the research field elucidating a factor with the influence and the mechanism for a regional climate. RCM can reproduce transient atmospheric phenomena when it uses a re-analysis data as a boundary condition, which is difficult to reproduce for GCMs. In addition, RCM can perform the sensitivity experiments for the investigation of mechanisms or impacts of a factor which affects regional climate in meso-scale (Eastman et al. 2001; Liang et al. 2005; Yoshimura and Kanamitsu 2009). In this research, a RCM was used as a tool for investigation of the SST impact on the regional climate.

1.2 Interaction between atmosphere and ocean in the mid-latitude

Between the atmosphere and ocean, heat and water vapor are exchanged mutually through the surface of the ocean. Since heat is transported deeply among the ocean, coefficient of heat diffusion (1 x 10^{-4}～10^{-2} m^2 s^{-1}) is larger than that in the land (1 x 10^{-7} m^2 s^{-1}). There is much quantity of the downward short wave radiation in the tropics and subtropics, while latent and sensitive heat fluxes from ocean to atmosphere are relatively small comparing to the short wave radiation. Heat is transported poleward by ocean currents and atmospheric circulations and disturbances.

In the mid-high latitude, heat is supplied from ocean to atmosphere through the ocean surface. Latent and sensitive heat flux of bulk formula in the ocean surface described by Kondo (1975) as follows,

$$H = c_p \rho C_H U (T_s - T) \qquad (1-1)$$

$$E = \rho C_E U (q_s - q) \qquad (1-2)$$

where, H is sensitive heat flux, E is latent heat flux, C_p is specific heat at constant pressure, ρ means atmospheric density, C_H and C_E means sensitive and latent bulk transport coefficients, respectively, U means wind speed, T is surface temperature, q means mixing ratio, T_S means SST, q_s means surface saturated mixing ratio at T_S, Here, the heat flux from the ocean to atmosphere sets to be positive direction.

Sensitive heat flux is proportion to the difference between SST and surface air temperature as shown in equation (1-1). The value in winter is bigger than that in summer, because, air temperature decreases significantly in the mid-high latitude. Latent heat flux is proportion to humidity difference between sea surface and atmosphere, thus it becomes bigger as atmosphere is more dry as shown in equation (1-2).

Ocean supplies heat to atmosphere in the mid-high latitude by turbulent heat flux of the warm currents, while atmosphere drives the ocean currents by wind stress accompanied with atmospheric general circulation. Such large scale ocean circulation by wind forcing is called wind driven circulation, which influences on surface ocean current up to several hundreds meters depth. In the tropics, trade wind blows from east to west and westerly blows from west to east in the mid latitude. This negative (positive) wind curl causes clockwise (unclockwise) subtropical ocean circulation in the northern (southern) hemisphere.

Figure 1.1 shows the major ocean currents in the world. West side currents of the subtropical gyre of each ocean are called " western boundary currents (WBC)" and are known to be stronger than the east side of the gyre. For instance, the Kuroshio flows on the west side of the North Pacific and the Gulf stream flows to the west side of North Atlantic for the north. In the southern hemisphere, there is a strong southward flow as a Brazilian current on the west side of South Atlantic Ocean and the East Australian Current in the west side of the South Pacific Ocean.

Stommel (1948) clearly explained the intensified WBC mechanism under isodensity current in a rectangle ocean basin. He showed that asymmetric flow appears when it takes account of β effect, which is not appeared under constant Coriolis force. In the low latitude, the ocean receives the wind stress from trade wind, and the ocean receives the wind stress of westerly jet in the mid-latitude (Fig. 1.2).

The ocean current is forced to the right direction to the movement direction by Ekman transport. As result of that, sea surface height rises, and downward motion occurs the inside of subtropical gyre. The balance between geostrophic flow and this downward motion is called Sverdrup balance and describe as follows,

$$\beta v = f\frac{\partial w}{\partial z} \qquad (1-3)$$

where, f is Coriolis parameter, w is vertical speed at z is vertical co-ordinate, v is meridional speed. The Coriolis parameter f at latitude θ_0 can be written *by* β-plain approximation in a

local coordinate x-y system as follows,

$$f = f_0 + \beta y \qquad (1-4)$$

where, $\beta \approx \frac{2\omega}{R} cos\theta_0$, $f_0 \approx 2\omega\, sin\theta_0$, ω is the angular speed of Earth's rotation. The positive Y-axis is northward. Here, the water column in the subtropical gyre shrinks due to the Ekman pumping, as a result, the light hand term $\frac{\partial w}{\partial z}$ becomes negative. Since β and f_0 are positive, the southward flow ($v < 0$) happens for the balance of the both side of the equation (1-3). This flow is called Sverdrup transport. In the Northern Hemisphere, most of the subtropical gyre in the mid-latitude flows slowly to the south, and near the equator, the meridional motion is nearly equal to zero and it flows westward. To compensate inflow to the south of the wide area together in the narrow area, a strong northward flow forms at the west side boundary in each ocean.

The reason that a strong flow occurs to the west side boundary of the ocean can also be explained by Sverdrup transportation and the frictional effect around the west and east side of boundary. Pacific anticyclonic wind stress drives ocean current; that is, the ocean current obtains negative vorticity ($\zeta_w < 0$). Since the absolute vorticity is preserved, the ocean current obtains negative vorticity at the west side of the boundary as the planetary vorticity f increases due to the change in latitude from low to high ($\zeta_f < 0$). When friction exists in both side of boundary, the ocean current obtains a positive viscous vorticity ($\zeta_r > 0$), that is, on the west side of the boundary, $\zeta_w < 0$, $\zeta_f < 0$, and $\zeta_r > 0$, respectively. Therefore, a large positive value of viscous vorticity ζ_r is required to balance these three terms. This implies that the strong northward flow occurs at the west side of the boundary. On the other hand, the ocean current obtains positive vorticity ($\zeta_f > 0$) due to the change in latitude from high to low on the east side of the boundary, that is, $\zeta_w < 0$, $\zeta_f > 0$, and $\zeta_r > 0$, respectively. It means that ζ_r does not need to become large for the balance of these three terms. This implies that the southward flow around the east side of the boundary is relatively weak.

Various interactions between atmosphere and ocean occur in the WBC region where large

amount of heat are transported from tropics. Figure 1.3 shows schematic figure of ocean influences on climate in the WBC region (Kwon et al. 2010). One of the remarkable atmospheric-ocean interactions in the tropics is ENSO. The change of SST influences on supply of water vapor to the atmosphere even if it is quiet small. The change of the amount of water vapor causes activity of cumulus, and it causes large atmospheric variability in the midlatitude through the atmospheric general circulation anomaly forced to the convection. This phenomena is called “teleconection” (Nakamura et al. 2008; Trenberth et al. 1998; Liu and Alexander 2007; Kwon et al. 2010).

The anomaly of general atmospheric circulation by teleconection changes westerly jet and synoptic scale turbulences in the mid-latitude. The disturbances changes wind strength and direction on the ocean surface. The influences extend to not only mixing layer but also thermocline. That is, SST anomaly in tropical region could changes SST anomaly in the distant area through the atmospheric circulation. This mechanism is called “atmospheric bridge” (Klein et al. 1995; Alexander et al. 2007).

On the other hand, the WBC influences the atmosphere directly by the strong turbulent heat flux through the sea surface. It changes the direction to the east at the mid latitude. The “ extention flow” characterized the remarkable SST incline of the north south direction. This meridional baroclinicity of SST plays an important role for activities of transient wave disturbances and the formation of westerly on the ocean (Nakamura and Sampe 2004; Nakamura et al. 2008). Nakamura et al. (2008) investigated storm track activity in the average circulation environment under the steep meridional gradient of SST at the mid latitude as a boundary condition. They showed that maximum storm track activity little shifted pole ward from the SST front, and the axis of the storm track locked on the SST front. On the other hands, in the experiment under the gradual SST distribution, pole ward heat transport, the index of the turbulent activity in the mid latitude, decreases from 1/3 to 1/4 of the gradient SST experiment and the axis of the storm track does not concentrate at specific latitude. They suggested that relived baroclinicity of atmosphere due to the gradual SST distribution causes decrease of

available potential energy.

The influence of SST front reaches to not only planetary boundary layer but also free troposphere through the strong atmospheric convection (refered in Kelly 2010). Minobe et al. (2008) revealed the impact of the Gulf stream on the whole troposphere using satellite data, re-analysis data and atmospheric model. They showed that wind convergence occurs in the marine atmospheric boundary layer (MABL) over the Gulf stream, where lower cloud generates and precipitation occurs. The upward motion reaches to the upper troposphere, where wind of the divergence occurs. Similar results were obtained in the Agulhas Return Current (Liu et al. 2007), Kurosio Extension (Tokinaga 2009).

1.3 Influence of Kuroshio on the atmosphere

As described in the previous section, the discharge of heat by the western boundary current exerts various influences on the mid-latitude atmosphere. This section focused on the effect of the Kuroshio, the North Pacific WBC, on the atmosphere.

Kuroshio is a warm western boundary current that transfers substantial amounts of heat from the western tropical Pacific to the mid-latitude region of the western North Pacific. It flows east-northeastward along the Pacific Ocean side of the Japanese islands and then moves off the Japanese coast to the east at around 35 °N, forming the eastward jet known as the Kuroshio Extension (KE).

The influences on atmosphere over the Kuroshio region (including turbulent heat flux, rainfall, the wind) are similar to those of the other WBC region, but there are different points (Kelly et al. 2010). First, East Asian monsoon influences on atmosphere strongly in the region (Yoshiike and Kawamura 2009; Iizuka et al. 2013). Second, the Kuroshio that goes to north from East China Sea (ECS) diverges to the Sea of Japan and the Pacific Ocean side because the Japanese Islands exist (Kelly et al. 2010). Finally, cold SST distribution that reflected the terrain effect in winter is formed because depth in the vicinity of the continental shelf of ECS is shallow.

As a result, strong SST inclination is formed between warm Kuroshio (Xie et al. 2002).

Kuroshio has large influences on the Meiyu-baiu frontal zone characterizing the East Asia monsoon (Xie et al. 2002; Sasaki et al. 2012; Xu et al. 2011; Miyama et al. 2012; Kuwano-Yoshida et al. 2013; Kunoki et al. 2015). Meiyu-baiu appears from June through the middle of July and often brings heavy rain damage to East Asia. Unlike a normal weather front, the Meiyu-baiu front is characterized by a large gradient of equivalent potential temperature (EPT) rather than that of the air temperature (Ninomiya 1984). The southwest lower-level wind around the subtropical high and the southwest low-level wind from the South China Sea and Indonesia peninsula supply water vapor in the Meiyu-baiu precipitation zone. In addition to the moisture convergence, other important factors for the maintenance and strengthening of the Meiyu-baiu front have been suggested by a number of studies (Ueda et al. 1995; Sampe and Xie 2010, Kuwano-Yosida et al. 2013). Ueda et al. (1995) suggested that the Meiyu-baiu termination is connected to the onset of convection over the subtropical northwestern Pacific. Sampe and Xie (2010) investigated the relationship between the position of the westerly jet and the rainfall zone from a thermodynamic viewpoint to understand the large-scale formation of the baiu front. Using analysis data and the LBM experiment, they showed that the upward motion which is excited by the warm advection from the south flank of the Tibetan plateau induces convective activity; as a result, it forms the Meiyu-baiu rainy zone. When upper westerlies shift to the north of the SST front, the evaporation supply from the sea surface decreases rapidly. This causes the sudden weakening of the baiu rain front after the passing of the rainy season (Kuwano-Yosida et al. 2013). These results suggest that the SST is related closely to the formation and disappearance of the Meiyu-baiu rain front.

Moreover, various investigations are reported about the influence that Kuroshio and Kuroshio Extention (KE) give to the atmosphere as the observation technology advances (Nonaka and Xie 2003; Bond and Cronin 2008; Tanimoto et al. 2009, Tokinaga et al. 2009; Liu and Xie 2013).

Tokinaga et al. (2009) examined atmospheric three-dimensional structure around the KE

front by analyzing the observation with a satellite and a ship measurement, and clarified the influence of the KE front on clouds. In winter, sensible plus latent heat flux that exceeded 450 W m^{-2} was observed in KE. This heat flux warmed MABL and induced the atmospheric convection on the south side of the KE front. As a result, higher clouds and active lightning were observed. In early summer, southerly warm advection suppressed turbulent heat flux, and low clouds were observed on the south side of KE front and sea fog occurs on the north side of the KE front.

Tanimoto et al. (2009) also reported the results of the atmospheric sounding campaign to clarify the effects of the KE front on the structure of MABL and low clouds. They observed that as baiu front across the KE front to the north, warm humid air from the south was suddenly cooled and thick fog layer formed there. As the baiu front had moved away to the south, cold humid air from north caused highly unstable MABL in the warmer flank of the SST front. As a result, solid cloud deck was observed in the inversion. On the other hand, in the colder flank of the SST front, stability was almost neutral. Therefore, vertical mixing was relatively small. Altitude of cloud base decreases monotonically from the side of warm SST to the cold SST flank. Stratus cloud replaced with broken clouds scattering with lower cloud base. The results suggest the SST front has influences on synoptic scale phenomena such as baiu frontal zone fluctuation, and that it brings a change to the static stability of the boundary layer and generation of cloud and fog.

Sasaki et al. (2012) examined the influence of the Kuroshio in the ECS on the baiu rain band using satellite observations and reanalysis data. They showed that strengthened precipitation, high surface wind speed, energetic evaporation, and wind convergence on the Kuroshio region, and also showed that the vertical wind speed and diabatic heating due to the convergence have maximum peaks at the middle level of troposphere. In addition, they showed that the reinforcement of precipitation disappeared in the experiment which was removed the influence of the Kuroshio artificially. These results are consistent with those of Miyama et al. (2012) which investigated a rainband on the ECS in May 2010.

Kunoki et al. (2015) were reported that instability of the boundary layer, increase of

turbulent heat flux, the development of MABL and supply of evaporation in the Kuroshio during the observation campaign in the ship which went in June, 2012.

Kuroshio and KE also influences on explosive cyclone with a high development rate. Yoshiike and Kawamura (2009) investigated East Asia monsoon strength and association with the explosive cyclone activity using re-analysis data in the winter season and showed that the activity of the cyclone centered near Japan when monsoon activity was active. This observation fact was confirmed by Iizuka et al. (2013) using a regional atmospheric model. They concluded that Kuroshio and KE caused atmospheric baroclinicity at the time of strong monsoon condition, and that reinforcement of the evaporation supply from the ocean increases the frequency of the explosive cyclone in this area.

1.4 Mechanism of Kuroshio large meander and its influence on the atmosphere

Kuroshio is known for its meandering behavior; it sometimes deviates from its straight path (SP), along the coast of Japan, and meanders to the southeast, away from the coast (Fig.1.4). This flow pattern is known as the Kuroshio large meander (LM). Various researchers have studied the mechanism of Kuroshio flow variation, and these became clear that there are some factors for the formation process of the Kuroshio LM (Kawabe 1995; Qiu 2003; Tsujino et al. 2006; Usui et al. 2008).

Usui et al. (2013) investigated the long-term variability of the Kuroshio path south of Japan, and suggested that duration of the Kuroshio LM strongly depends on the Kuroshio transport. They suggested that low transport leads to a long duration of the Kuroshio LM by an ocean data assimilation system. They also revealed that stable KE state is an important factor for sustained Kuroshio LM.

Tsujino et al. (2013) clarified the Kuroshio formation mechanism by a historical OGCM simulation. They suggested that three important factors for the LM formation, that is, propagation of a pair of small cyclonic and anti-cyclonic eddy from the upstream of the Kuroshio,

enhancement of the small meander by merging cyclonic eddy from the east, and accumulation of warm Kuroshio water from upstream. Strong SST gradient of Kuroshio, as mentioned in the previous section, could have various influences on atmospheric phenomena such as precipitation, wind, static stability and disturbances in the mid-latitudes. However, research of the influence on the atmosphere by the change of the Kuroshio path just started recently, and has not been clear enough.

Recently, the Kuroshio LM influences on the atmosphere such as precipitation and temperature around Japan started to be investigated. Kuroshio LM brings a cold eddy on the north side of the meander area. It is pointed out that the influence reaches widely though the area is limited from the Kii peninsula offing to the west of Izu Islands.

For example, Nakamura et al. (2012) examined the behavior of cyclone tracks using an observational 40-year wintertime sea level pressure (SLP) dataset. They suggested that cyclone tracks shift southward and that cyclone development rates are decreased during Kuroshio LM periods. They also showed that the correlation between snowfalls in Kanto area and the Kuroshio LM is high.

Hayasaki et al. (2013) used a high-resolution coupled general circulation model (CGCM) to investigate cyclone activity in winter over the Kuroshio. They showed that the cold eddy pool of the Kuroshio LM prevents the rapid developing of the cyclone, and found that these results agreed well with the analysis of observational data reported by Nakamura et al. (2012).

However, thus far, the research has focused primarily on cold seasons, and considerably less is known about the effects of the Kuroshio LM on climate throughout the year. One of the reasons is that the air-sea heat flux is relatively weak in the warmer seasons. It is therefore more difficult to detect the atmospheric impact of the Kuroshio LM, except in cold seasons. Although most of the previous studies focus on a Kuroshio LM area, and have not been investigated enough about the influence that a Kuroshio LM gives to the climates such as the rainfall, temperature of Japan islands.

This study aims to estimate the impact of the Kuroshio LM quantitatively and to clarify the mechanism how the cold pool influences on the neighboring convection activity. To represent the narrow structure of the Kuroshio and its variation in terms of oceanic and atmospheric characteristics, it was necessary to use a spatial resolution of 0.2° or higher, since the width of the current and the radius of curvature of the Kuroshio LM is approximately 1°. The RCM used by Murazaki et al. (2005) and Sasaki et al. (2006) performs better when used with high resolution SST than when used with low-resolution SST. We therefore used an updated version of the high-resolution North Pacific Ocean General Circulation Model (NPOGCMv.2) and a 20 km resolution RCM (RCM20) developed by the Meteorological Research Institute (MRI) of Japan.

A long-term integration driven by JRA-25 (Japanese Re-Analysis 25 years) atmospheric forcing was conducted using NPOGCMv.2 that can resolve the Kuroshio and the accompanying SST change. A 20-year integration with RCM20 was performed using the SST simulated by NPOGCMv.2 as a lower boundary condition and JRA-25 as a lateral boundary condition.

In this study, the SST of an ocean model simulation was used because a physically consistent field in the upper ocean, which comprises SST, subsurface water temperature, oceanic current, can be obtained with high horizontal resolution for the whole JRA-25 period without missing value. To the best of our knowledge, such a dataset based only on observations is currently unavailable. To detect detailed atmospheric responses to the change in the Kuroshio path, we compared these results with those of another long-term integration run performed by Murazaki et al. (2010), which used RCM20 with observational low-resolution SST data as the lower boundary condition.

This thesis is organized as follows. Chapter 2 mentions model description in this study. Chapter 3 shows the evaluation of RCM20, and describes the results of sensitivity experiments regarding SST-resolution dependency and atmosphere-ocean interaction. Chapter 4 describes the impacts of the Kuroshio LM on the climate around Japan in every season using RCM20 and NPOGCM. Discussion is presented in Chapter 5. Finally, Chapter 6 presents summary and

conclusions.

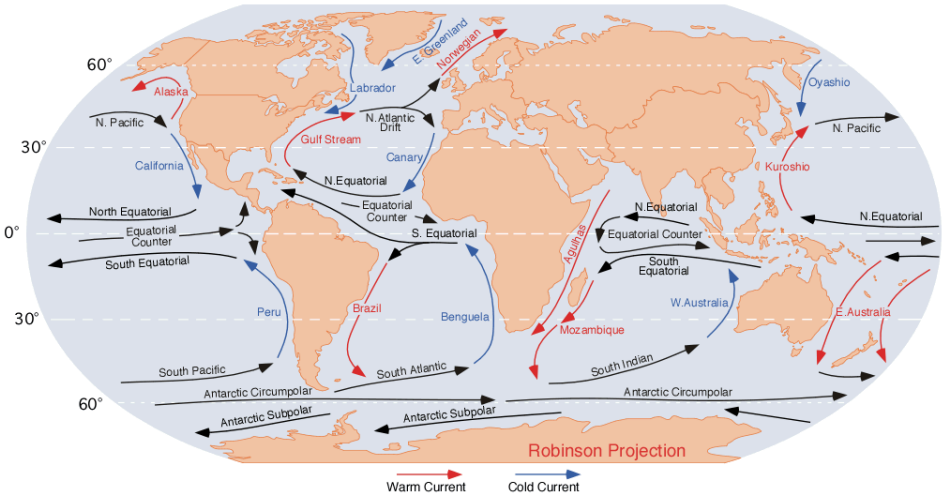

Fig.1.1 Main ocean cuurents in the world. The quotation is from Pidwirny (2006).

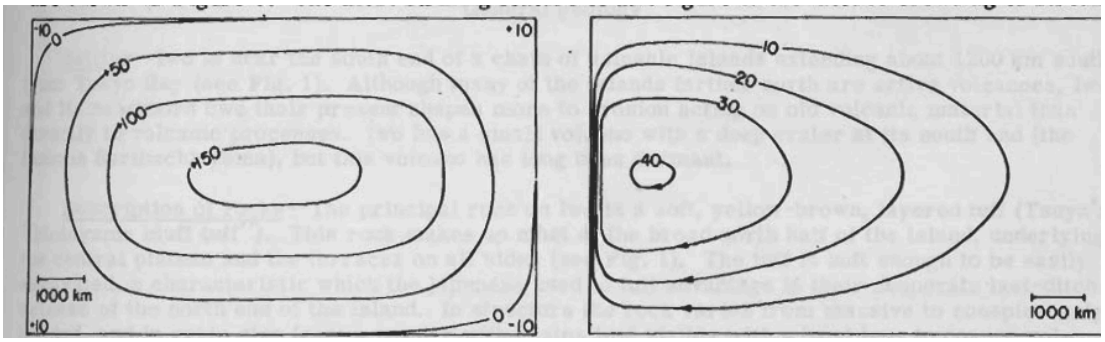

Fig. 1.2 Stream line for the case of (a) uniformly rotating oceans, and (b) Coriolis force is a linear function of latitude. The quotation is from Stommel (1948).

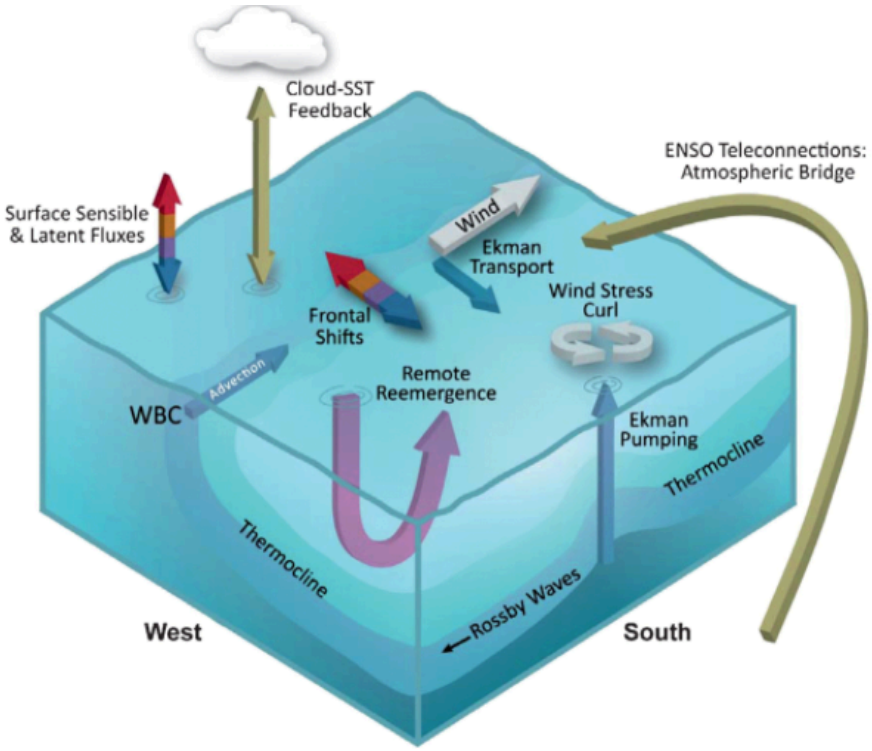

Fig. 1.3 Schematic figure of the process that has an influence on the SST variability in the WBC area. The quotation is from Kwon et al. (2010)

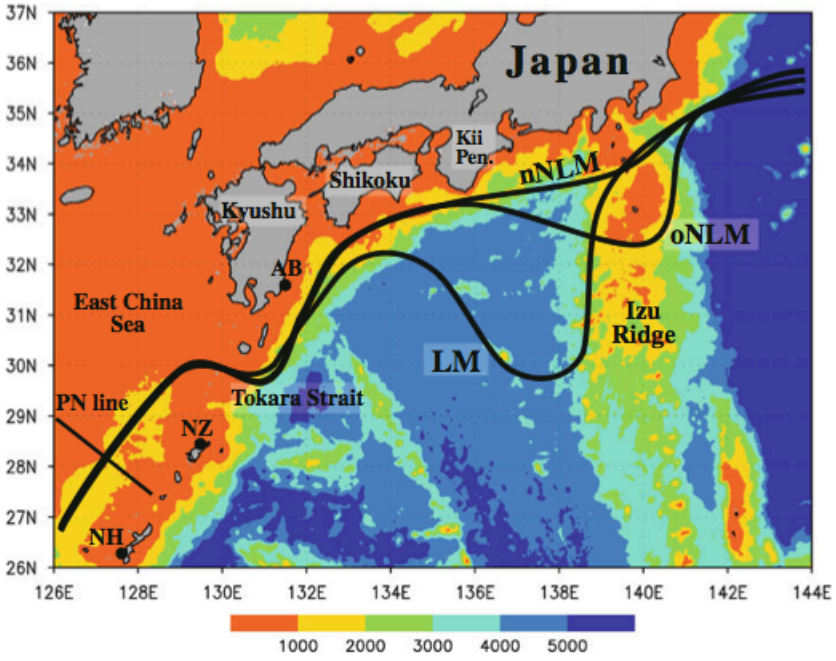

Fig. 1.4 Bathymetry and three stable Kuroshio path; LM: Large meander, NLM: non-large meander (SP: straight path in this thesis). NLM is categorized to two kinds of paths (n: nearshore and o: offshore). The quotation is from Usui et al. (2013).

CHAPTER 2 Data and models

2.1 Observational data

A lateral boundary condition used in this study is Japan 25-year reanalysis (JRA-25) dataset. This dataset consists of reanalysis data from 1979–2004 at 6-hourly time intervals. It was produced by the Japan Meteorological Agency (JMA) and the Central Research Institute of the Electric Power Industry (CRIEPI) (Onogi et al. 2007). The resolution for the atmospheric data was 1.25° × 1.25°. The JRA-25 dataset also includes the 1.125° resolution SST dataset (hereafter, JRA-SST) based on central *in situ* observation-based estimates (COBE) of SST produced by the JMA (Ishii et al, 2005; Onogi et al. 2007).

In the section 3.1, we used the data sets obtained from Automated Meteorological Data Acquisition System (AMeDAS) stations and the Radar-AMeDAS composite data. The AMeDAS stations are located at an average interval of 17 km apart throughout Japan and the spatial grid resolution of Radar-AMeDAS data sets is 5 km. To evaluate climate distribution of precipitation, we also used 1-km mesh climatic data developed by JMA. This dataset is based on multivariate analysis of weather observation data, with topographical factors as explanatory variables.

In the section 3.2, a merged satellite and *in situ* data global daily SST (MGDSST) was used as a lower boundary condition. The resolution is 0.25 ° × 0.25 ° (Kurihara et al. 2006). We also used it in the section 4.2 for comparison of the model result.

2.2 Regional climate model

An atmospheric model used in this study is RCM20. RCM20 is based on a regional spectral model originally developed by the JMA as a short-range forecast model (NPD/JMA 1997). The model used in this study has a 20 km horizontal mesh with 36 hybrid vertical levels and covers Japan in the same way as described by Sasaki et al. (2006). The model includes the Mellor and

Yamada (1982) level-2 scheme for vertical diffusion, the Arakawa and Shubert (1974) cumulus convection and convection adjustment schemes, a short-wave radiation scheme (Lacis and Hansen 1974), a long-wave radiation scheme (Sugi et al. 1990), and a ground surface process (Takayabu et al. 2004). A spectral boundary coupling method proposed by Kida et al. (1991) was used for the long-term simulations. In this method, the large-scale results of the outer model and the small-scale results of the inner nested model are combined in wave number space. This has the advantage of a smooth long-term integration, avoiding contradictions between an outer coarse-mesh model and a nested model with respect to large-scale fields. A detailed description of RCM20 can be found in Sasaki et al. (2000).

Figure 2.1 illustrates the topography of JRA–25 and RCM20. In RCM20 (Fig. 2.1b), altitudes of mountains in central Japan are closer to the real altitudes than in JRA–25, although there is still a discrepancy in altitude between RCM20 and the real topography.

2.3 Coupled atmosphere-ocean regional climate model

In the section 3.3, we used a high-resolution, Coupled Atmosphere-Ocean Regional Climate Model (MRI-CRCM), which was described by Sasaki et al. (2006). The atmospheric component of MRI-CRCM is RCM20 which was described in the previous section. The ocean component of the MRI-CRCM is the NPOGCM based on the Meteorological Research Institute Community Ocean Model (MRI.COM), described by Ishikawa et al. (2005) and showed its performance by Ishizaki and Motoi (1999) and Tsujino and Yasuda (2004). The model domain is from 15 °S to 65 °N in latitude and from 100 °E to 75 °W in longitude with horizontal resolution of 1/4 ° longitude, 1/6 ° latitude, and 48 vertical layers. It uses the bulk formula developed by Large and Pond (1982) for heat, momentum and fresh water exchange processes between the ocean and the atmosphere.

The outer model used in the experiments is the MRI-CGCM2 at a resolution of about 2.8° in longitude and latitude with 30 layers. For further detail on MRI-CGCM2, see Yukimoto et al. (2001). The MRI-CGCM2 generated data from two kinds of experiments: a present climate

simulation and a 110-year simulation using the IPCC SRES A2 emission scenario initialized in 1990. During the two ten-year periods (1991 to 2000 and 2061 to 2070), atmospheric fields are sampled from the MRI-CGCM2 simulation at a frequency of six hours for input into the CRCM. We use two-step nesting due to the coarser grid size of the MRI-CGCM2 (Fig. 2.2). First, a 60 km-resolution Regional Climate Model is nested with the MRI-CGCM2 results; likewise, a 20 km-resolution Japan region RCM is nested with a 60 km-resolution RCM. The 60km-resolution East Asian region RCM has the same model structure except for the grid size and the grid number.

As to the ocean component, the ocean and atmosphere interact only in a 20km-resolution RCM domain. Outside this region, the ocean model used the results by 60km-resolution RCM in East Asian region and the MRI-CGCM2 for the rest of domain as atmospheric forcings. Initial oceanic state is given by the result of the CGCM-run which has performed long time calculations started from 1981 with the IPCC SRES A2 scenario following a 20-year spin-up with climatological forcings (Sato et al. 2006). Using the results of the year 1990 and 2070, we performed a present climate run and a future projection run (section 3.3.1 and 3.3.2).

2.4 High-resolution ocean model

In Chapter 4 and 5, North Pacific Ocean general circulation model v.2 (NPOGCMv.2) was used to acquire high-resolution SST data. It is the updated version of the ocean component of CRCM described in section 2.2, and is based on the MRI.COM, which was described by Ishikawa et al. (2005) and evaluated by Ishizaki and Motoi (1999) and Tsujino and Yasuda (2004). The model domain covers the area from 15 °S to 65 °N and from 100 °E to 75 °W with 34 vertical layers and a horizontal resolution of 1/4° in longitude and 1/6° in latitude. Around Japan (25–50 °N, 120–160 °E), the resolution is 1/10° in both the longitude and latitude. The model includes a bulk formula for calculating surface flux developed by Kondo (1975), a vertical mixing scheme based on Mellor and Yamada's (1982) level 2.5 scheme (Mellor and Blumberg

2004), and a horizontal mixing scheme with biharmonic operators. High-accuracy advection schemes are used for the tracers, UTOPIA (Leonard et al. 1993) for the horizontal and QUICKEST (Leonard 1979) for the vertical direction, as well as for momentum (Ishizaki and Motoi 1999). In addition to the main mixing scheme, two kinds of additional mixing are imposed. First, to reproduce the low SST in summer along the Kuril Islands (Nakamura et al. 2004), a tidal mixing parameterization based on St. Laurent et al. (2002) is used. Second, to reduce the strong fluctuation of the Kuroshio at the southern coast of Japan, a harmonic viscosity is added for momentum dissipation over steep bottom topography, with a viscosity coefficient of $2.5 \times 10^2 \cos\varphi$ m^2 s^{-1}, where φ is the latitude.

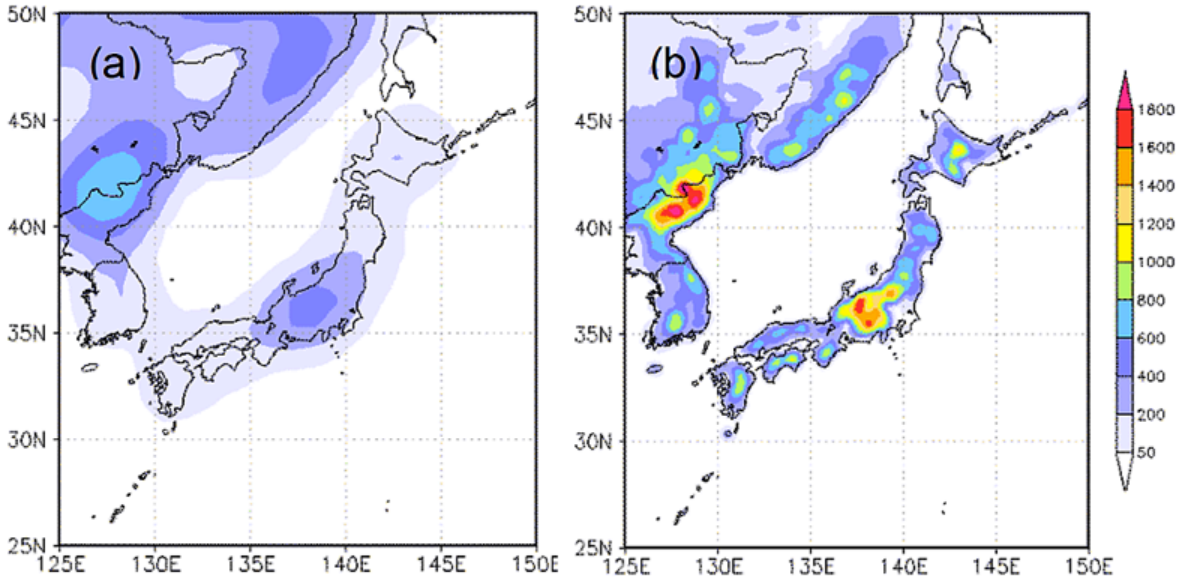

Fig. 2.1 Topography of (a) JRA–25 and (b) RCM20. Units are meters (m).

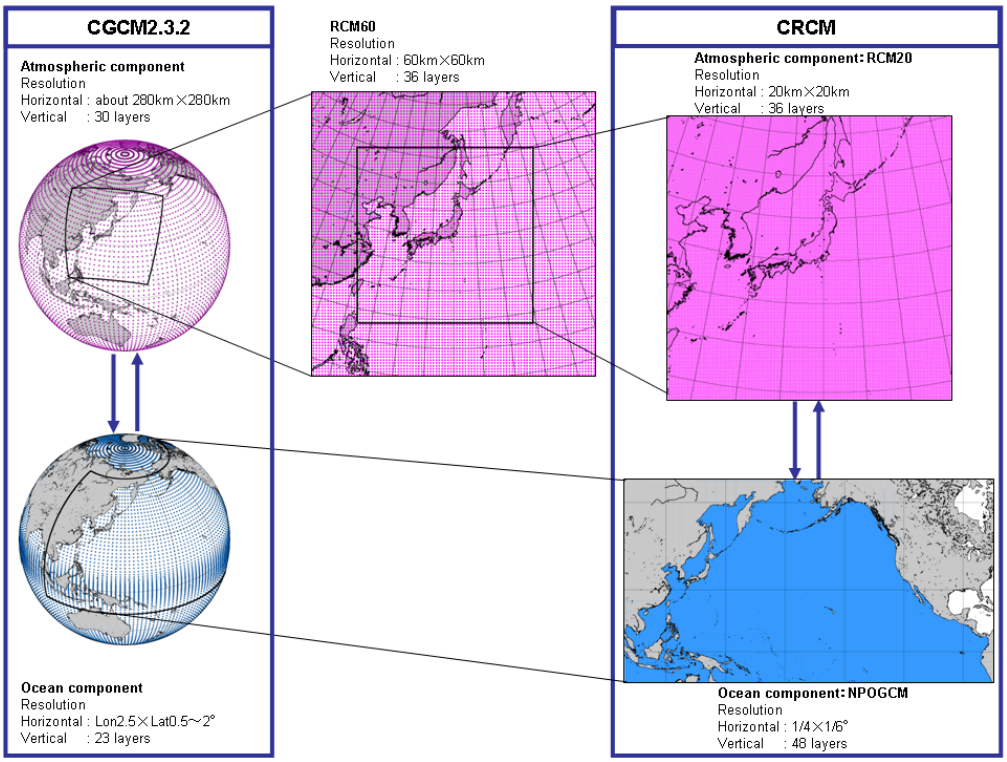

Fig. 2.2 Conception diagram of the MRI-CRCM .The quotation is from JMA (2008).

CHAPTER 3 Evaluation of RCM20 and the sensitivity experiments

3.1 Dynamical downscaling of JRA-25 precipitation over Japan using the MRI-Regional climate model

To understand the mechanism of the air-sea interaction on the regional scale, three-dimensional high-resolution grid data covering both land and ocean areas with a uniform grid are indispensable. Re-analysis data is useful to complement non-uniform observational data, but the resolution in these sources is not high enough to investigate the climate around Japan.

In this section, a continuous 26-year dynamical downscaling of a re-analysis data using RCM20 was conducted to study regional climate change around Japan. The accuracy of downscaling results was examined using the observed precipitation data. Downscaled precipitation data performed well at both monthly and daily time scales, including extreme events. Data also correlated well with observed inter-annual variability of daily precipitation frequencies for heavy rain events over Japan. These results demonstrate the high capacity of RCM20 for dynamical downscaling and the suitability of the data for investigating regional climate change. The results were also used as a control run in the RCM20 experiment using NPOGCMv.2 (Chapter 4).

3.1.1 Quality of downscaled data

To compare the model results with observations, we used the data sets obtained from AMeDAS stations and the Radar-AMeDAS composite data. To evaluate climate distribution of precipitation, we also used 1-km mesh climatic data developed by JMA. This dataset is based on multivariate analysis of weather observation data, with topographical factors as explanatory variables. For comparison, precipitation data from JRA–25 were interpolated on the RCM20

grid.

Figure 3.1 presents the monthly precipitation for January. Comparison with the observed climate data clearly demonstrates an apparent precipitation peak on the Sea of Japan side, which is on the windward side of the Japan islands, (Fig. 3.1c). This climatic distribution is not clear in Fig. 3.1b. However, some problems still remain. RCM20 results show an unrealistic wavy pattern in Fig. 3.1c as a result of the characteristics of the spectral atmospheric model. Furthermore, the precipitation peaks are sensitive to topography effects, which cause irregular distributions of precipitation over areas close to the Sea of Japan.

Figure 3.2 depicts monthly precipitation for July. The Bonin high is usually accompanied by a moisture rich, southwesterly wind, so the precipitation peak appears over the western part of the Japan islands (Fig. 3.2a). This feature is represented in both results (Figs. 3.2 b and c), but the RCM20 results provide a more detailed distribution than those of JRA–25.

The climate of Japan varies widely from region to region with the southern areas of Japan having subtropical climates, while the northern areas experience sub-frigid climates. In order to evaluate the efficacy of the model in capturing these climatic differences, statistical evaluation was performed with seven climatic areas using the methods from Sasaki's paper (2006), as shown in Fig.3.3.

Figure 3.4 compares the model bias, correlation coefficient and root mean square error (RMSE) of monthly mean precipitation periods from 1979 to 2004 for the seven climatic areas. Because of its topographical enhancements, RCM20 significantly improved the scores for these areas, particularly for the Sea of Japan in the cold season (Fig. 3.4 a, e and i). JRA–25 showed bias overestimation in area 7 and large underestimation in the remaining areas, whereas RCM20 showed significantly improved performance in all areas except area 7. RCM20 performed better because it more accurately represents topography and uses a more realistic precipitation distribution. JRA-25 underestimated precipitation in area 1 for every month, while RCM20 substantially improved both bias and RMSE of precipitation (Fig. 3.4 a and b). RCM20 also

improved bias and RMSE (except for winter) in area 2 (Fig 3.4 c and d). When compared to the observational data, precipitation was overestimated by RCM20 in the plains regions. A possible explanation is that the snow cloud beyond the mountain range increased rainfall, as RCM20 topography is lower than actual topography. Further investigations in this regard are indicated. In areas 3 and 5, enhanced topography in RCM20 again significantly mitigated the underestimation of JRA-25 in winter (Fig. 3.4 e, f, i and j). The large underestimations in areas 4, 5 and 6 in the warm season were somewhat improved, but some bias remained (Fig. 3.4 g, h, i, j, k and l). In contrast, the RCM20 bias in area 7 was even larger than that of JRA–25. The negative bias of surface temperature in this area is likely to suppress convection and was possibly caused by the SST distribution.

3.1.2 Examples of remarkable phenomenon

The timing and intensity of precipitation on a daily scale are also important for downscaling climate data. Figures 3.6 and 3.8 represent typical failure and success examples of extreme events. On this day, a stationary front extended eastward over Japan. Figure 3.5 shows the weather map and satellite image on September 11, 2000 produced by JMA. Figure 3.6 represents a model failure example. It shows the amount of precipitation (a), along with the data from JRA-25 (b) and simulation from RCM20 (c). The front increased its activity with time because of a typhoon located at approximately 500 km southwest of Japan and produced more than 400 mm day^{-1} of rainfall at Tokai area as indicated by the arrow in Fig. 3.6 a. As shown in Fig. 3.6 b, the precipitation peak of JRA–25 is approximately 100 km northwest from the actual peak in the observation data. RCM20 simulates a similar precipitation distribution to JRA-25 (Fig. 3.6c). The similarity in precipitation distributions shared by both JRA-25 and RCM20 indicates that any apparent discrepancies between the outer data (JRA-25) and the observations at a large scale, such as the location of a front, are difficult to improve by the downscaling using RCM20.

Figure 3.7 and 3.8 show an example, where the models accurately simulated the precipitation distribution that occurred on August 21, 2001. A typhoon track the Pacific side of

central Japan and heavy rain peak can be seen on the southeast side of western Japan in Fig. 3.8 a. RCM20 significantly improves these rain peaks compared to JRA-25. For a geopotential height of 850 hPa, the RCM20 result is quite similar to that of JRA–25, suggesting that the large-scale characteristics of the free atmosphere are quite similar to JRA–25. Although the simulated large-scale phenomena are similar in RCM20 and JRA-25, RCM20 presents a more realistic precipitation.

3.1.3 Statistics on heavy rainfall

In order to statistically compare observation data with model results, we established 0.5 by 0.5 degree grid boxes that covered Japan. We then took into account the grid boxes that had two or more AMeDAS stations and two or more grid points of the RCM20 (Fig. 3.9). Daily precipitation amounts were calculated for each box. We defined the averaged station precipitation value in a box as the 'observed grid box value', and the averaged RCM20 (JRA-25) grid point value in a box as the 'RCM20 (JRA-25) grid box value'. The number of boxes that met each criterion for daily precipitation amount were summed up as specific area for 26 years (9497 days) and normalized by the total number of boxes. We defined this value as the Precipitation frequency Coverage Rate (PCR), which relates to the frequency and spread of a given precipitation intensity.

$$PCR(y) = \frac{\sum_{i=1}^{N} OR(i,y)}{\sum_{i=1}^{N} TR(i,y)} \qquad (3\text{-}1)$$

where, OR(i,y) (i=1,365 or 366; y=1979, 2004) is the number of grid boxes in which box-averaged daily precipitation that meets the criteria, TR(i,y) is the total number of the grid boxes over Japan on day "i" in year "y".

Figure 3.10 presents the PCR categorized by daily precipitation intensity. We classified the PCR according to climatic differences, as shown in Fig. 3.3, then grouped the data into four

regions: the Sea of Japan side (area 1 and 3); the Pacific side (area 2 and 4); Western Japan (area 5 and 6); and the Nansei Islands (area 7). On the Sea of Japan side, the PCR from RCM20 (Fig. 3.10 a) corresponds well to that from AMeDAS. On the Pacific side (Fig. 3.10 b), there is a discrepancy in PCR between RCM20 and AMeDAS at high precipitation intensity exceeding 150 mm day^{-1}. A similar result can be seen in Western Japan, (Fig. 3.10 c). Both RCM20 and AMeDAS PCRs in Western Japan and on the Pacific side (Fig. 3.10b and Fig. 3.10c) show relatively high daily precipitation intensities compared to the Sea of Japan side (Fig. 3.10 a). The PCR values from JRA–25 (Figs. 3.10 a, 3.10 b, and 3.10 c) are consistently low, with daily precipitation intensity rarely exceeding 50 mm day^{-1}. There are no clear climatic differences in the precipitation distributions simulated by JRA–25 in Figs. 3.10 a, 3.10 b, and 3.10 c. It is only in Fig. 3.10 d, which shows the PCR of the Nansei Islands region, that JRA-25 shows a different precipitation range and one that matches quite closely to the daily precipitation range of 100 mm day^{-1} from AMeDAS. This area is covered by ocean dotted with islands. Therefore, the simulations by RCM20 could not be expected orographic effects. Furthermore, as previously mentioned, RCM20 has a cold bias, which adversely affects convection in the model. Despite the bias, the PCR from RCM20 is still more accurate than that from JRA-25 for precipitation intensities greater than 150 mm day^{-1}. These results indicate that RCM20 can simulate longer term trends in daily precipitation intensity quite accurately and only fails systematically, when faced with extreme rainfall events of greater than 150 mm day^{-1}.

The year-to-year variations in PCR with daily precipitation exceeding 50 mm day^{-1} and 200 mm day^{-1} are evaluated in Fig. 3.11. Figure 3.11 a shows that RCM20 accurately simulates PCRs with precipitation intensity exceeding 50 mm day^{-1}. For example, the heavy rain years of 1993, 1998 and 2004 are well simulated. The correlation coefficient between the PCRs from RCM20 and AMeDAS is 0.91, which is considerably stronger than the JRA–25 result of 0.48. However, RCM20 is less robust when it comes to heavy rainfall events, when daily precipitation exceeds 200mm day^{-1}. Indeed, Fig. 3.11 b indicates that RCM20 underestimates the number of these high rainfall days with the correlation coefficient of 0.67. Nevertheless, this result is still

better than that of JRA-25.

3.1.4 Comparison with other models

In the previous section, we showed the evaluation results of the RCM20. Here, This section shows the precipitation accuracy of RCM20 in comparison experiment with other models based on Ishizaki et al. (2012). The evaluation models in their study are MRI-RCM20, MRI-NHRCM, NIED-RAMS (Regional atmospheric modeling system; Pielke et al. 1992) and TSKB-RAMS, TSKB-WRF (weather research and forecasting model; Skamarock et al. 2008). NIED-RAMS was developed by NIED (National Research Institute for Earth Science and Disaster Prevention), and TKSB-RAMS and TKSB-WRF were developed by the University of Tsukuba.

The JRA-25 downscaling experiments were performed with these 20 km-resolution models. All models except RCM20 were non-hydrostatic models. Ishizaki et al. (2012) created the Taylor diagram of each model according to a definition of Taylor (2001) (Fig.3.12). The Talor diagram plotted RMSE, correlation and skill score in one figure. When the result of the model completely accords with observation it is marked at X point in the figure. Compared to the other models, the RCM20 has high accuracy, particularly in winter. The RCM20 is a hydrostatic model, therefore the calculation cost is lower than other models. This result shows that RCM20 has an excellent cost performance as 20km resolution regional climate model.

3.2 Influence of high-resolution SST data on the atmosphere around Japan area

In the previous section, a 26-year integration using RCM20 nested within JRA–25 was conducted and was evaluated the results. that RCM20 is useful for downscaling coarse-resolution global climate data to fine-resolution regional climate data. The downscaled data is helpful to investigate regional climate change. For example, the data help us to understand the mechanisms behind increases in the frequency of heavy rain.

In this section, we investigated the SST resolution dependency of the RCM20 since the resolution of the JRA-SST (about 1°) is not enough to represent ocean currents such as Kuroshio. A year-long numerical integration was conducted using RCM20 with high-resolution of the SST (0.25°) data as a boundary condition.

3.2.1 Experimental design and the SST datasets

The model and the lateral boundary conditions in this study were RCM20 and JRA-25, which were the same as those used in the section 3.1. Two kinds of experiments were conducted with different SST data. One was the MGDSST-run, which used the fine resolution MGDSST data, as a lower boundary condition. The other was the JRA-run, which was conducted using downscaled data from section 3.1. The experiment started on December 22, 1999, and analysis was performed for the year following January 1, 2000.

Comparing the monthly mean SST of MGDSST in March to JRA-SST, the MGDSST showed that a cold SST area spread over the south, in the northeast Sea of Japan near the continent (Fig. 3.13). On the other hand, the warm current in the Sea of Japan went north along the Japanese islands. The MGDSST analysis shows that in the Pacific Ocean, Oyashio, with cold SST, is represented around the Sanriku coast, and warm SSTs appeared with the Kuroshio in the around Nansei Islands. In September, the Tsushima current, the warm current in the Sea of Japan, appears clearly, furthermore, the cold SST around the Chishima Islands and the warm SST with the KE are also well represented in the MGDSST analysis (Fig. 3.14).

Figure 3.15 indicates the time series of the SST averaged over the area of the square marked in Fig. 3.13a. There is no significant difference between MGDSST and JRA-SST throughout the year. However, MGDSST fluctuates when looked at on a daily time scale. MGDSST is in good agreement with JRA-SST over the period from May to September on the Sea of Japan side (square A in Fig. 3.13a). However, MGDSST is lower over the period from October to April, and the difference becomes especially remarkable from February to April (Fig. 3.15a). In the Pacific Ocean area, the area averaged SST taken in the Pacific Ocean (square B of Fig. 3.13a)

indicated a relatively good agreement in summer and winter, but MGDSST was lower than JRA-SST in spring and autumn (Fig. 3.15b). JRA-SST was created from observation data, but the original analysis scale was 600 km, thus the resolution was too rough to express the detailed ocean currents (Kuragano et al. 2007).

3.2.2 Response of atmosphere

In this section, the atmospheric differences between the MGDSST-run and JRA-run in 2000 are described in every season. Figure 3.16 shows the SST difference between the MGDSST-run and JRA-run. The positive changes appeared on the coastal side of the Sea of Japan in all seasons. The reasons are, as mentioned in the previous section, the improvement of the resolution in imaging the ocean current and the coastline.

Figures 3.17-3.21 depict the differences in surface temperature, sensitive heat flux, latent heat flux, wind, and precipitation between the MGDSST-run and the JRA-run. These atmospheric elements roughly corresponded to the distribution of the difference in the SST, except for precipitation. That is, in the area where the SST difference is positive, surface temperature rises, sensitive and latent heat fluxes increase, and the wind is strengthened. These changes in winter are relatively larger than those in the other seasons. In summer, the changes are quite small and mainly occurred in the ocean. On the other hand, the change in precipitation occurs not only the area where the SST shows large changes, but also over land areas.

Figure 3.22 indicates the surface temperature change and the change in the ratio of precipitation in seven climatic areas, as shown in Fig. 3.3. There are large warming changes in surface temperature in the Sea of Japan (areas 1 and 3), while the temperature tends to be cooler in the Pacific Ocean (areas 4 and 6). Especially negative changes occurr on the Nansei Islands throughout the seasons. As to precipitation (Fig. 3.22b), there are many cases that show changes within ± 20 %, excluding the Nansei Islands (area 7). The area containing the Nansei Islands has a large monthly variation in precipitation. These results suggest that the SST expression, such as warm currents, significantly influences the atmospheric elements. To investigate the regional

climate around Japan, it is necessary to pay attention to the influence of SST.

3.3 Reproducibility of the SST in the OGCM with different atmospheric forcings

In this section, the results of a present-day and a future projection experiment with the MRI-CRCM were presented to demonstrate how differences in atmosphere forcings change SST in the ocean model. As previously mentioned in section 2.3, the MRI-CRCM experiments used the MRI-CGCM2 generated data from two kinds of experiments: a present climate run (1991 to 2000) and future projection run (2061 to 2070). For comparison, we analyzed the result of MRI-CGCM2 of the same period (CGCM-run).

3.3.1 Present climate run

We compared the simulated SST of the CRCM and CGCM-runs for the present climate against observation. Figure 3.23 depicts the correlation between observed and simulated results of 10-year averaged annual mean SST for the whole domain of the CRCM. Although the model tends to overestimate SST by 1–4° C in regions with average temperatures < 24°C and to underestimate SST by 1° C in regions with average temperatures > 24 °C, the coefficient of correlation is satisfactory (0.987). Annual average SST of the CRCM results is 19.17°C, which is close to the observational data (19.25 °C).

Figure 3.24 shows 10-year averaged SST in winter and summer in the CGCM-run, CRCM -run and observational data. In winter, the CGCM-run has a positive SST bias in the Sea of Japan, which was reduced but not eliminated in the CRCM-run. The model overestimated SST by 3–5°C over the southern part of the Maritime province (133 °E / 42 °N) and the eastward offshore area of northern Japan (142 °E/ 40 °N). In summer, this bias disappeared in both simulations. However, a negative bias in the Pacific Ocean is present in the CRCM-run.

To examine the monthly SST biases of the simulations in the Pacific Ocean and Sea of

Japan, 10-year mean monthly SST time series (see squares A and B in Fig. 3.24 b) are averaged for these areas (Fig. 3.25). In area A, a positive bias appears in the cold season, possibly because the Tsushima Current. This is considered a source of warm water influx for the Sea of Japan, with an observed annual mean transport estimated at 2.0–3.0 Sv (1 Sv = 106 m^3 s^{-1}) (Isobe 1994; Jacobs et al. 2001; Takikawa et al. 2003). The CGCM run yielded 2.8 Sv and the CRCM run 2.2 Sv. As SST bias for the Sea of Japan improves by 10-20 % in the CRCM-run, this might be the driver behind the reduction of the Tsushima Current transport in this model; that is to say, the high resolution coupling causes positive feedback to SST distribution. Another possible reason is a warm surface air temperature bias over the Sea of Japan in winter as simulated by the MRI-CGCM2. During winter, cold continental winds blow to the Japanese Islands across the Sea of Japan. Cold air masses at temperatures below -30 °C often exists on the continent at that time, which are warmed in transit by the sea surface, leading to a steep gradation of temperature between land and sea. This is difficult for MRI-CGCM2 to represent due to lack of sufficient resolution.

This surface air temperature bias affects SST not only in the CGCM run but also in the CRCM simulation, since CRCM receives large-scale information from the outer model. In summer, a negative bias of ~ -2 °C relative to observations exists in the CRCM run on the Pacific Ocean side (Fig. 3.25 b, area B). Sasaki et al. (2006) have also pointed out this error. They suggested a causal relationship to an underestimate of the amount of rainfall. Since there are no cold biases in the CGCM-run, the cause is unlikely to be CGCM2 atmospheric forcing. This problem should be a focus of future research.

3.3.2 Future projection

In this subsection, we demonstrate the differences between the CGCM-RUN. Figures 3.26 (a) and (c) indicate that summer (winter) averaged SST increases by 1 to 4 °C (1 to 6 °C) around Japan; the increase is especially remarkable east of Hokkaido (148 °E/ 41 °N). These results are quite similar to those of the CGCM-run, which simulated a warming pool in this area (Figs. 3.26

(b) and (d)). Fig. 3.26 (c) indicates a positive warming signal (4 to 6 ° C) in winter over the south of Hokkaido similar to Fig. 3.26 (d), a difference can be seen off Sanriku (143 °E/ 39 °N) where the increase in SST becomes weak or even negative. This was not seen in the results of the CGCM-run.

It is interesting that there is a remarkable contrast between the warming area east of Hokkaido and the cooling area off Sanriku, even though the absolute value is small. This difference can possibly be induced by the high resolution of the CRCM wind field, which drives the ocean component of the CRCM.

The charts in Fig. 3.27 show 10-year mean surface wind of future projection run in winter calculated by the CRCM and the CGCM-run. It is obvious that the CRCM simulates detailed wind-distribution that could not be represented by the MRI-CGCM2. Due to topography and convective systems, wind direction differs from one grid to another. It could be causes difference of SST distribution and its changes in the future because it deeply connected each other.

Figures 3.28 show 10-year averaged surface wind speed changes in winter between future and present climate by the CRCM and MRI-CGCM2. Comparing Fig. 3.28 (a) to Fig. 3.28 (b), the CRCM can represent wind speed more clearly and in greater detail. Nonaka et al. (2003) identified the relation between changes in SST and in wind speed. They confirmed interaction between the ocean and atmosphere through convective activity of atmosphere over the Kuroshio south of Japan and its extension using satellite microwave measurements. They suggested that increased wind speed is related to warm SST anomalies, namely, increased in SST reduces the atmospheric static stability, which intensifies the vertical mixing, as result of that, faster wind aloft down to the surface. In our result, increased wind speed is seen over the high warming area the sea east of Hokkaido (148 °E/ 41 °N) and off Sanriku (143 °E/ 39 °N). SST increase is weaker in Fig. 3.26 (c) than in Fig. 3.26 (d) along a band of decreasing wind speed that extends from western Hokkaido (145 °E/ 42 °N) in a southeast direction. Although this region is located in the north of the Kuroshio Current area, the positive correlation between the ocean and the atmosphere is likely to be applied to these regions in our experiments. This result suggests

that the detailed future SST increase is strongly related to change in detailed surface wind fields.

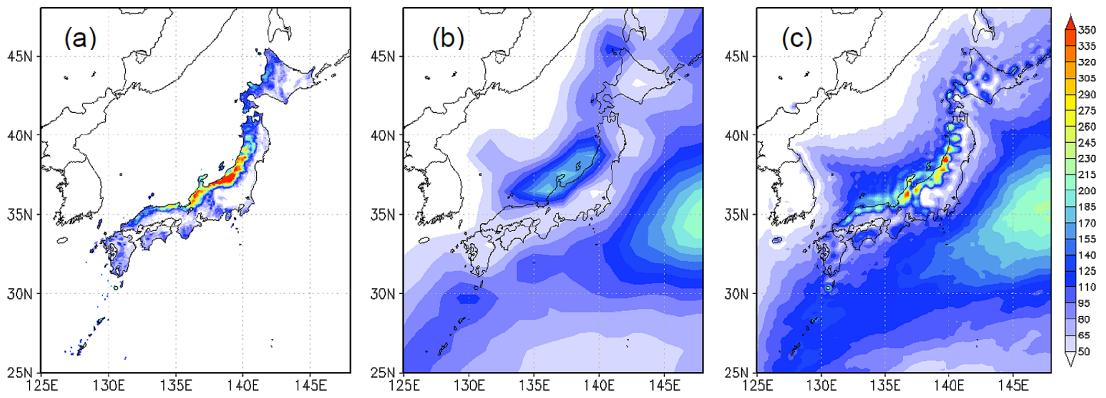

Fig.3.1 Monthly precipitation in January, (a) mesh climatic data from 1971 to 2000. (b) JRA-25 (c) RCM20.

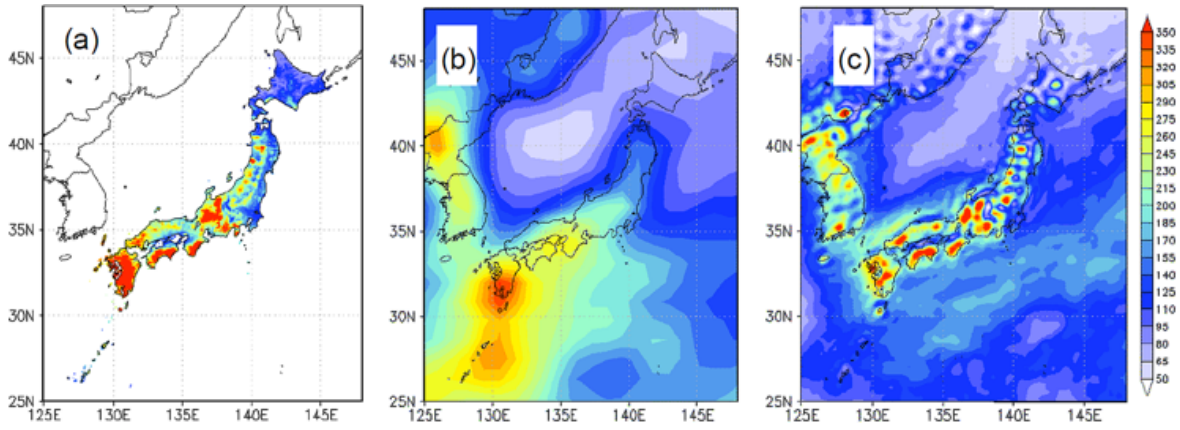

Fig. 3.2 Same as Fig.3.1 except for July.

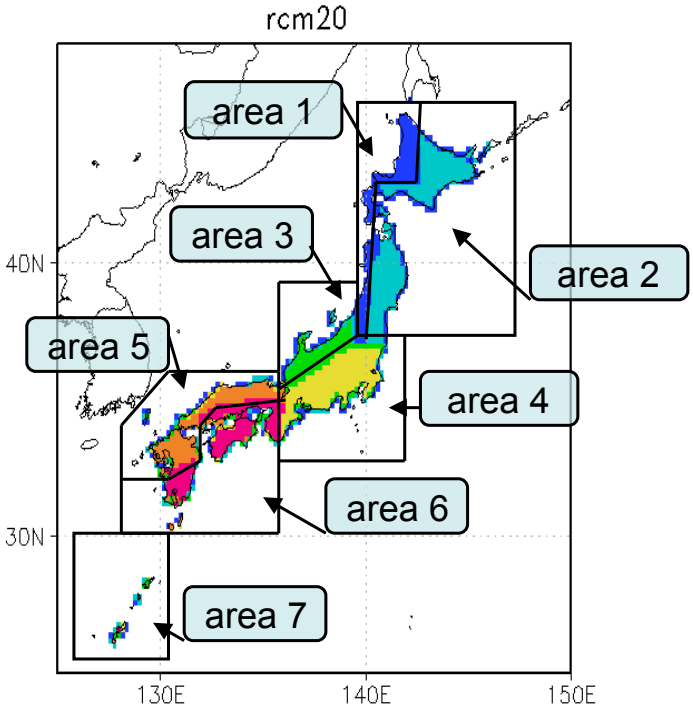

Fig. 3.3 Climatic areas for analysis. area 1: cold, snowfall in winter; cool in summer; area 2: cold and dry in winter, cool in summer; area 3: heavy snowfall in winter; area 4: dry in winter, wet in summer; area 5: rain or occasionally snowfall in winter, much rain in summer; area 6: dry in winter, much rain in summer; area 7: oceanic type of climate, warm and humid during all seasons (Sasaki et al. 2006, reconstruction by the author).

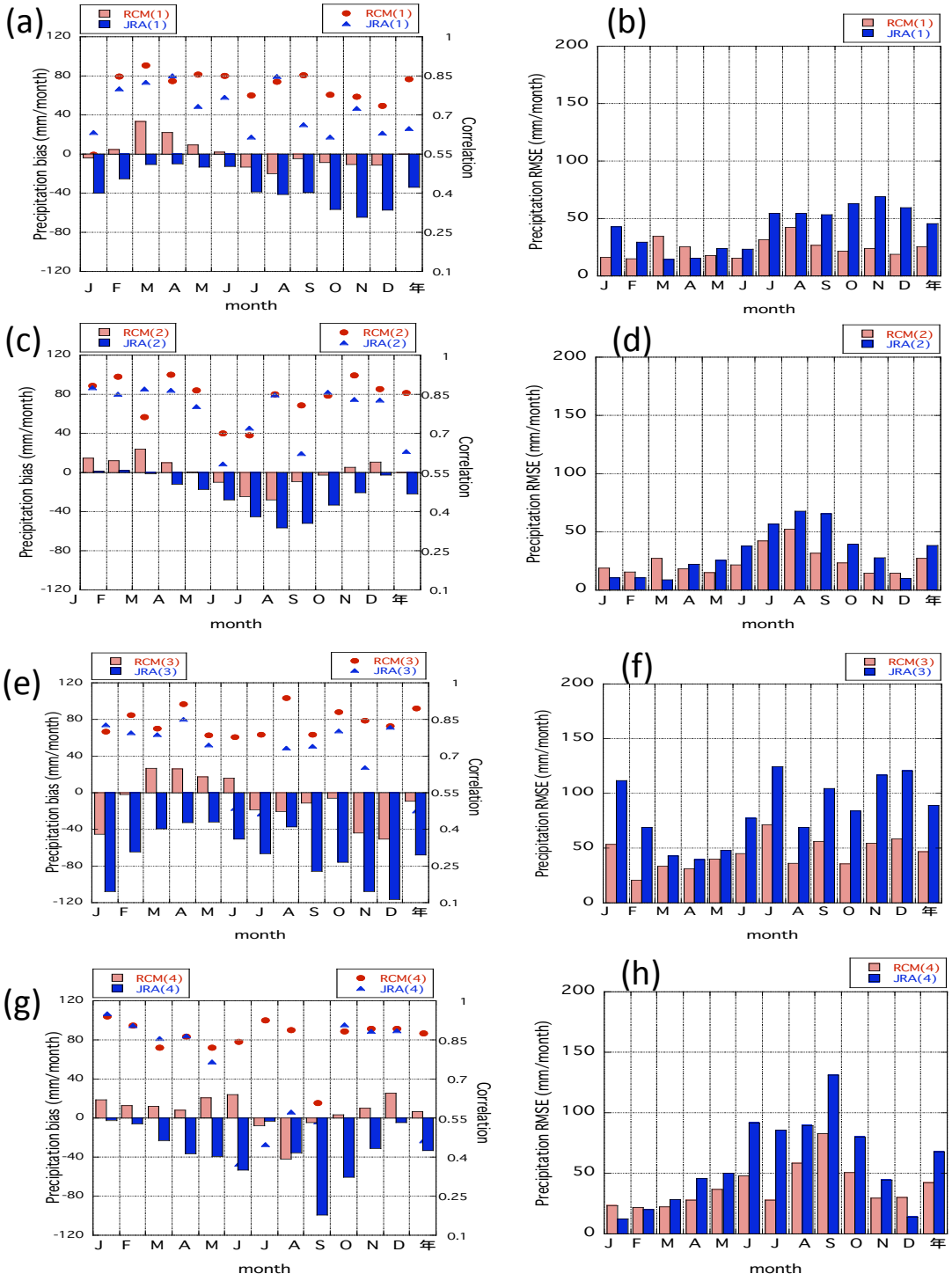

Fig.3.4 Statistical scores of monthly precipitation averaged over seven climatic areas. Bias (column in the left side panels), correlation coefficient (squares and circles in the left side panels) and RMSE (column in the right side panels) between AMeDAS and both RCM20 (red) and JRA–25 (blue). “All” on horizontal axis means averaged all over Japan. Units are mm precipitation per month. (a) and (b) area 1, (c) and (d) area 2, (e) and (f) area 3, (g) and (h) area 4.

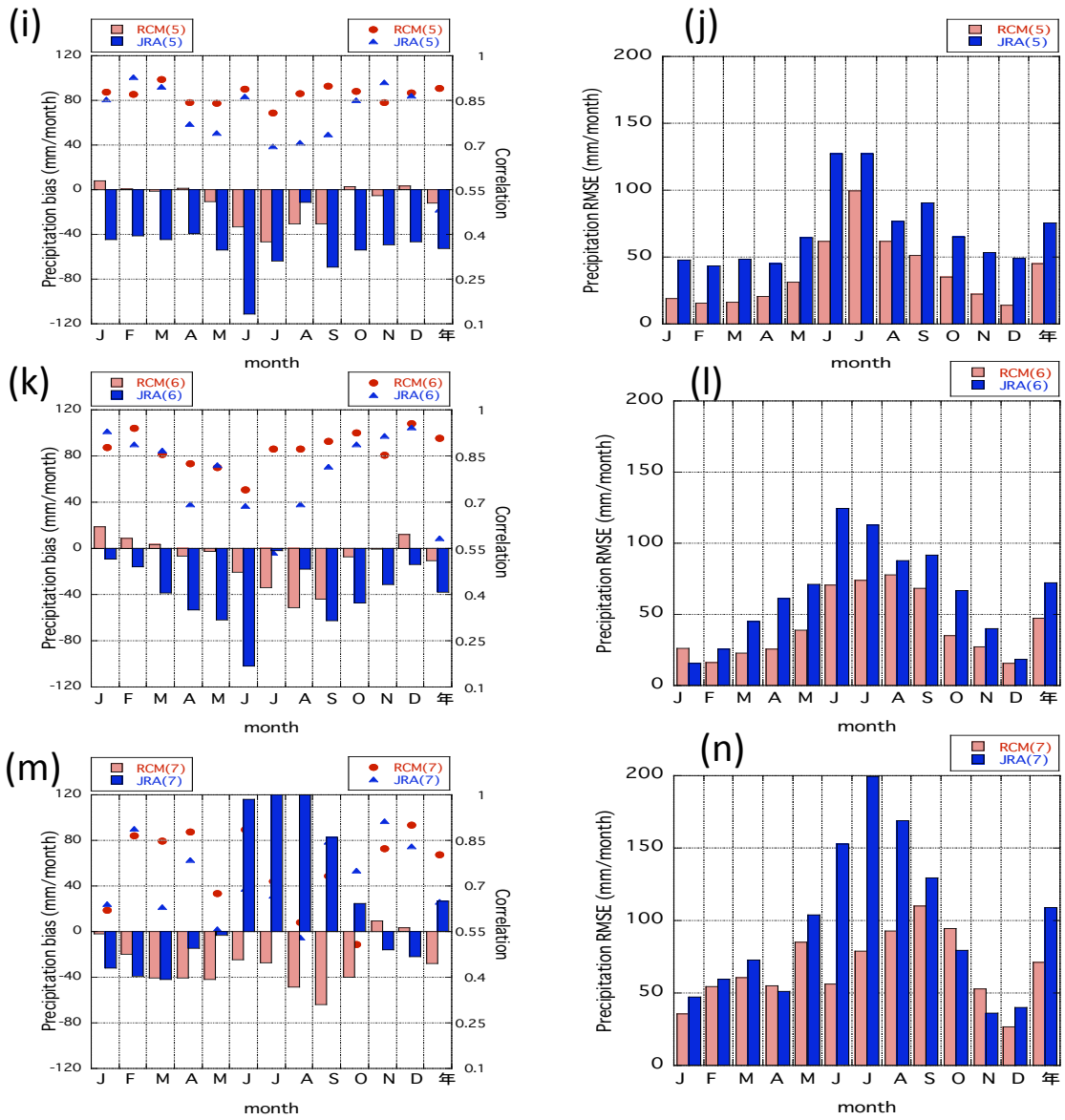

Fig.3.4 continued. (i) and (j) area5, (k) and (l) area 6, (m) and (n) area 7.

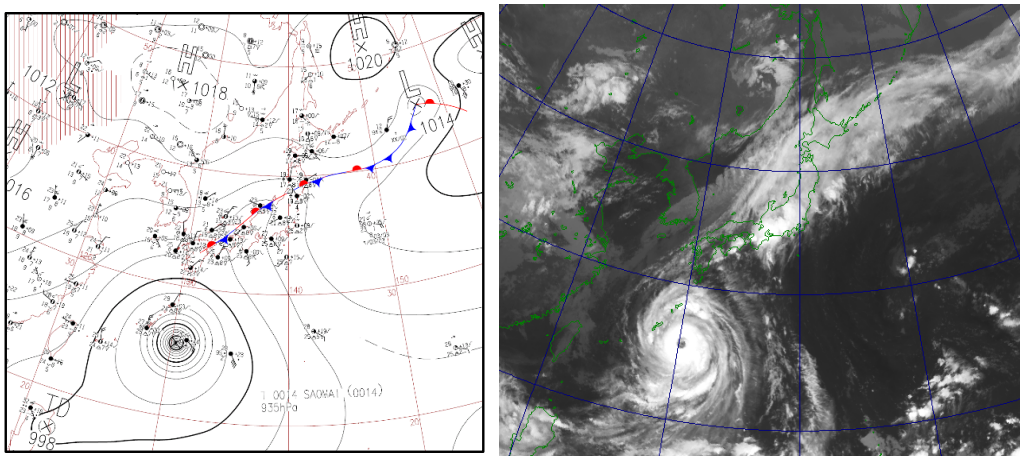

Fig.3.5　Weather map and satellite infrared imagery on September11, 2000 (Provided by JMA).

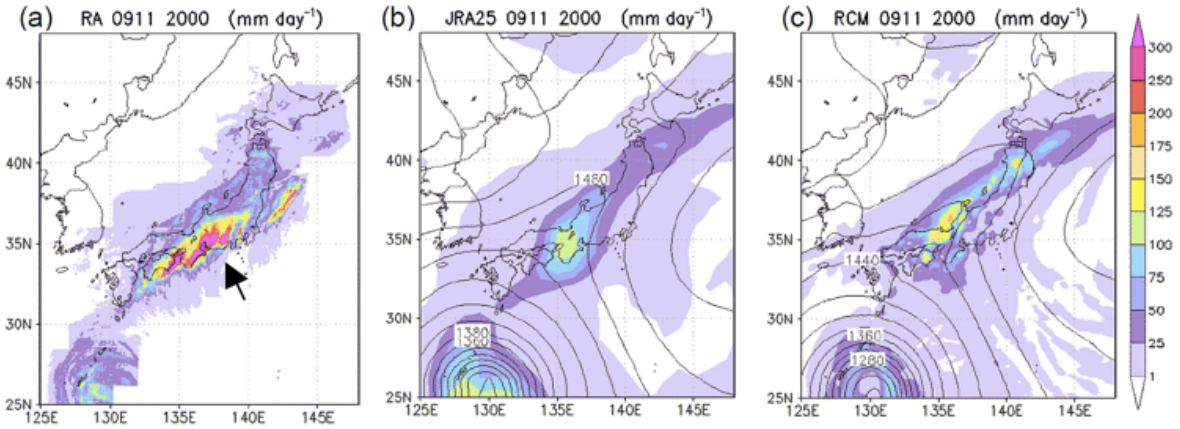

Fig.3.6 Precipitation amount (mm day^{-1}) and geopotential height (m) at 850 hPa on September 11, 2000 using observation (Radar-AMeDAS composite data), (b) JRA–25 and (c) RCM20 data. Arrow indicates Tokai area.

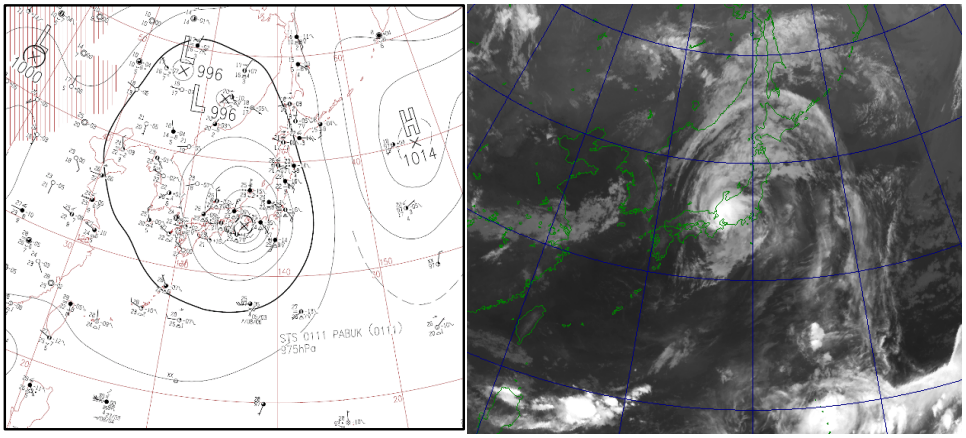

Fig.3.7 Weather map and satellite infrared imagery on August 21, 2001 (Provided by JMA).

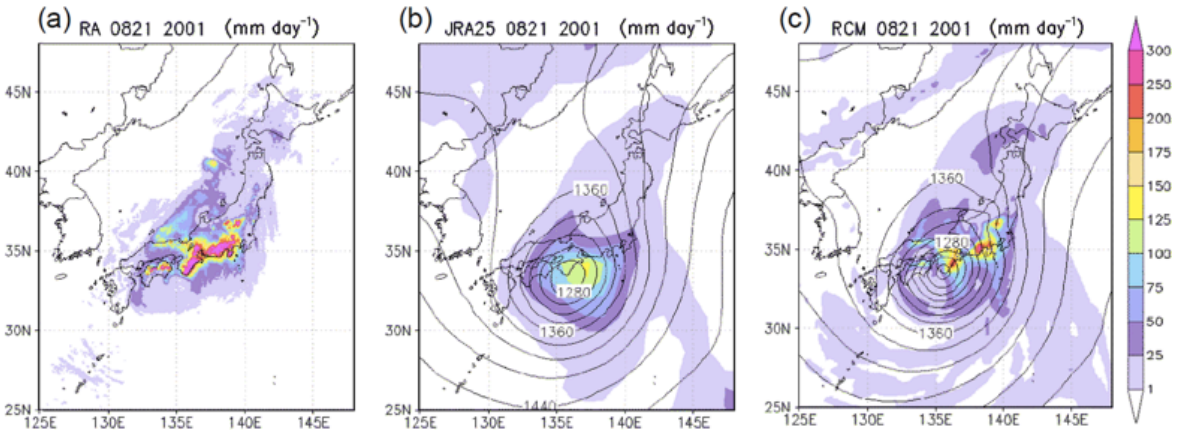

Fig.3.8 Precipitation amount (mm day^{-1}) and geopotential height (m) at 850 hPa on August 21, 2001 using observation (Radar-AMeDAS composite data), (b) JRA–25, and (c) RCM20 data.

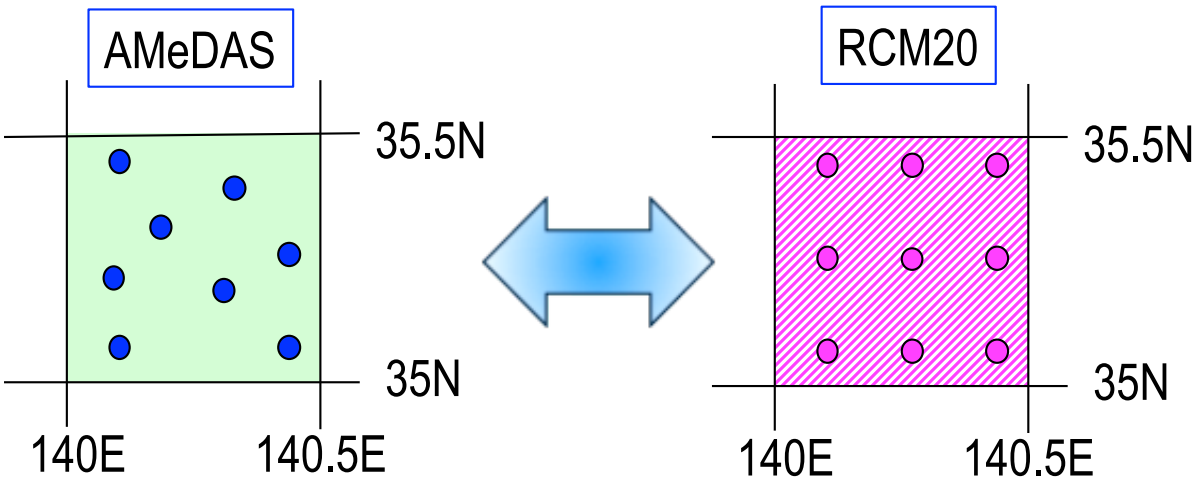

Fig.3.9 Conception diagram of grid box.

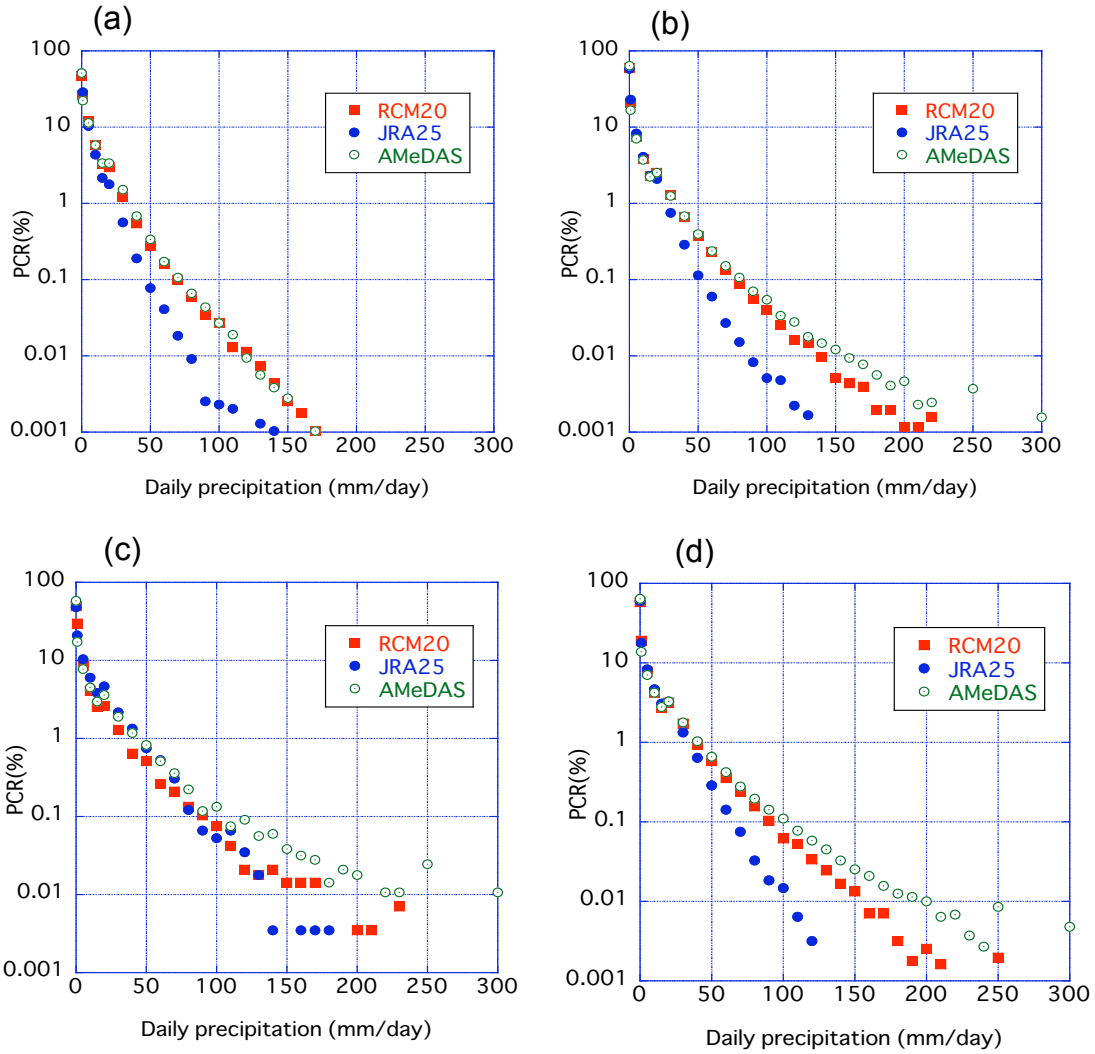

Fig. 3.10 Regional comparison of PCR as a function of daily precipitation intensity in RCM20 (red), JRA–25 (blue), and AMeDAS (green) in (a) the Sea of Japan side, (b) the Pacific Ocean side, (c) Western Japan and (d) the Nansei Islands area.

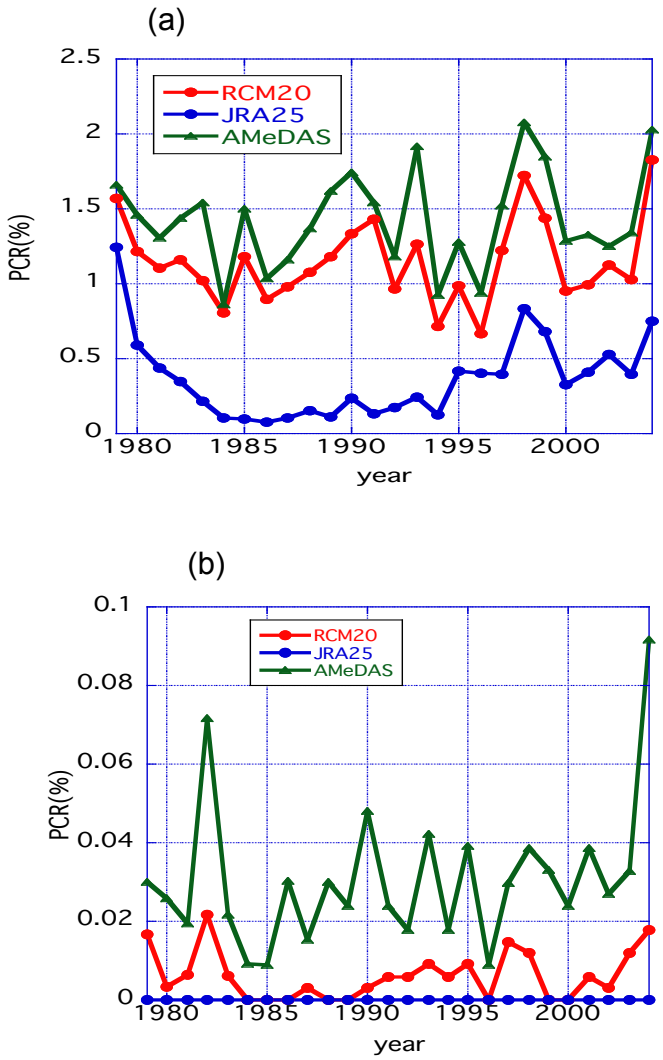

Fig. 3.11 Time series of PCR in Japan area exceeding (a) 50 mm day^{-1} and (b) 200 mm day^{-1} in daily precipitation intensity with RCM20 (red), JRA–25 (blue) and AMeDAS (green) data.

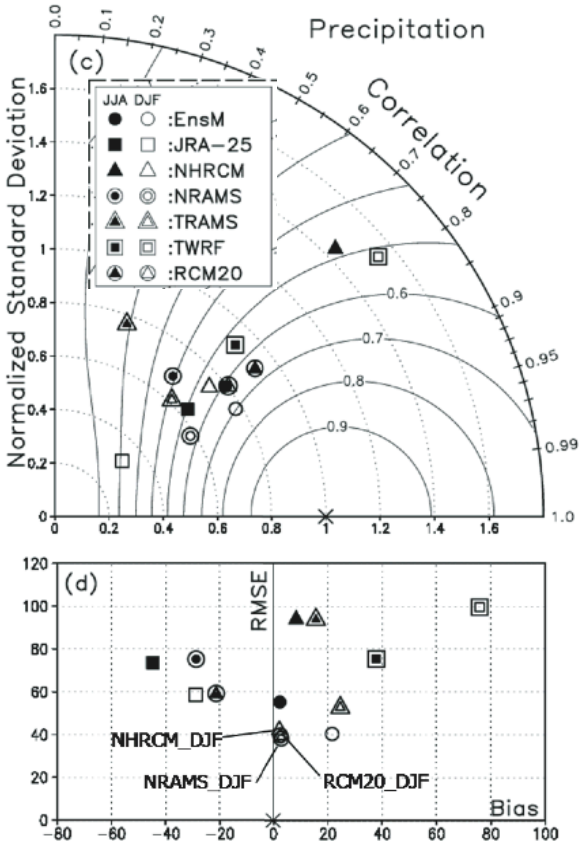

Fig. 3.12 (c) The Taler diagram and (d) bias-RMSE scatter diagram for precipitation. The contour indicates Taylor's skill score. (The quotation is from Ishizaki et al, 2012)

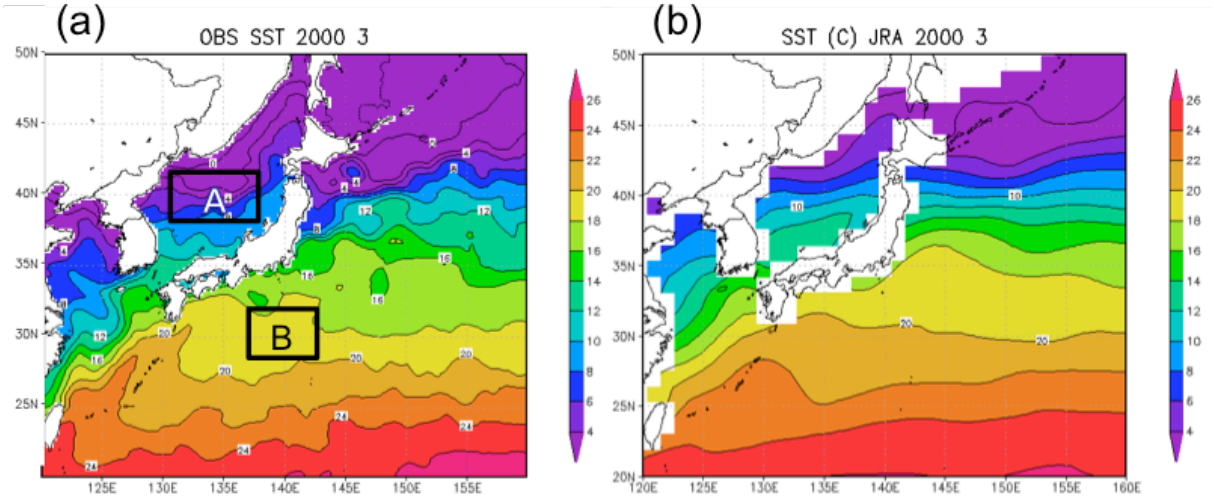

Fig. 3.13 Monthly mean SST in March, 2000 (a) MGDSST and (b) JRA-SST. The unit is °C.

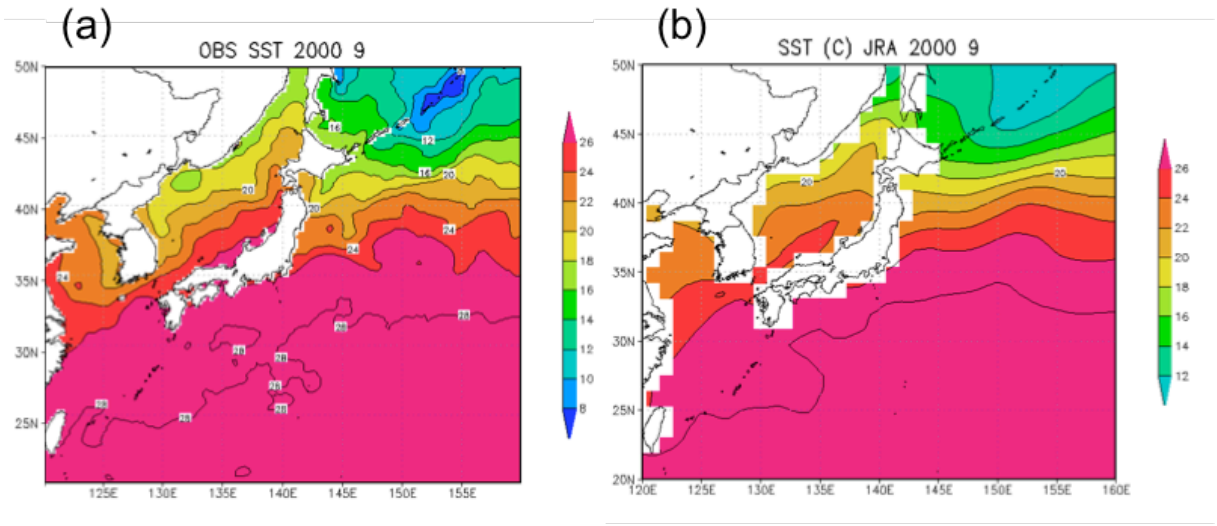

Fig. 3.14 Monthly mean SST in September, 2000 (a) MGDSST and (b) JRA-SST. The unit is °C.

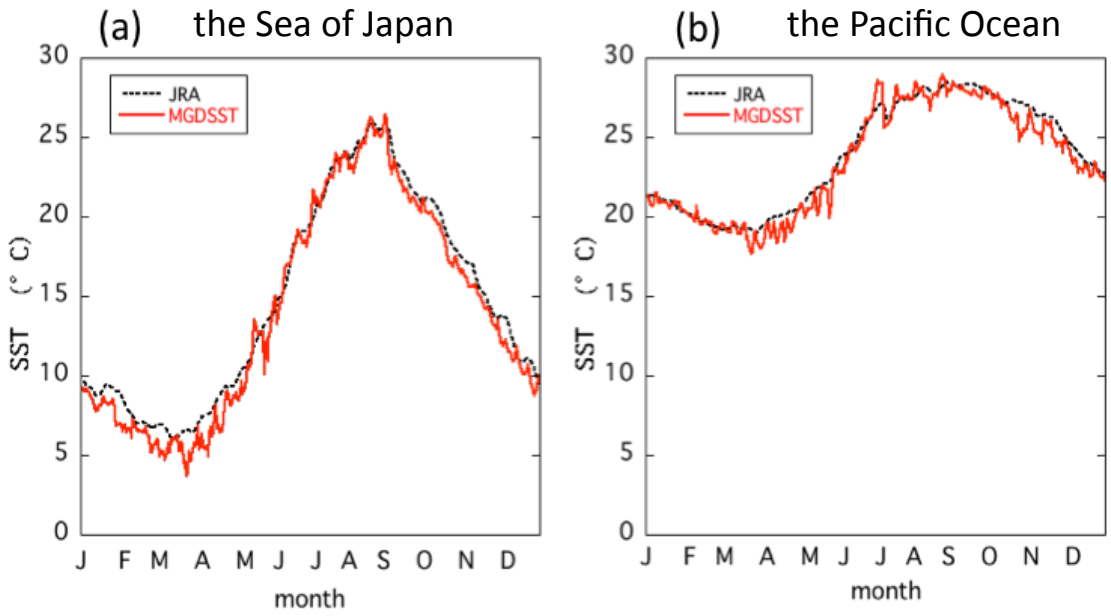

Fig. 3.15 Time series of SST averages over (a) Sea of Japan (area A in Fig. 3.13 a) and (b) Pacific Ocean (area B in Fig.3.13 a). Red lines: MGDSST. Black lines: SST of JRA-25.

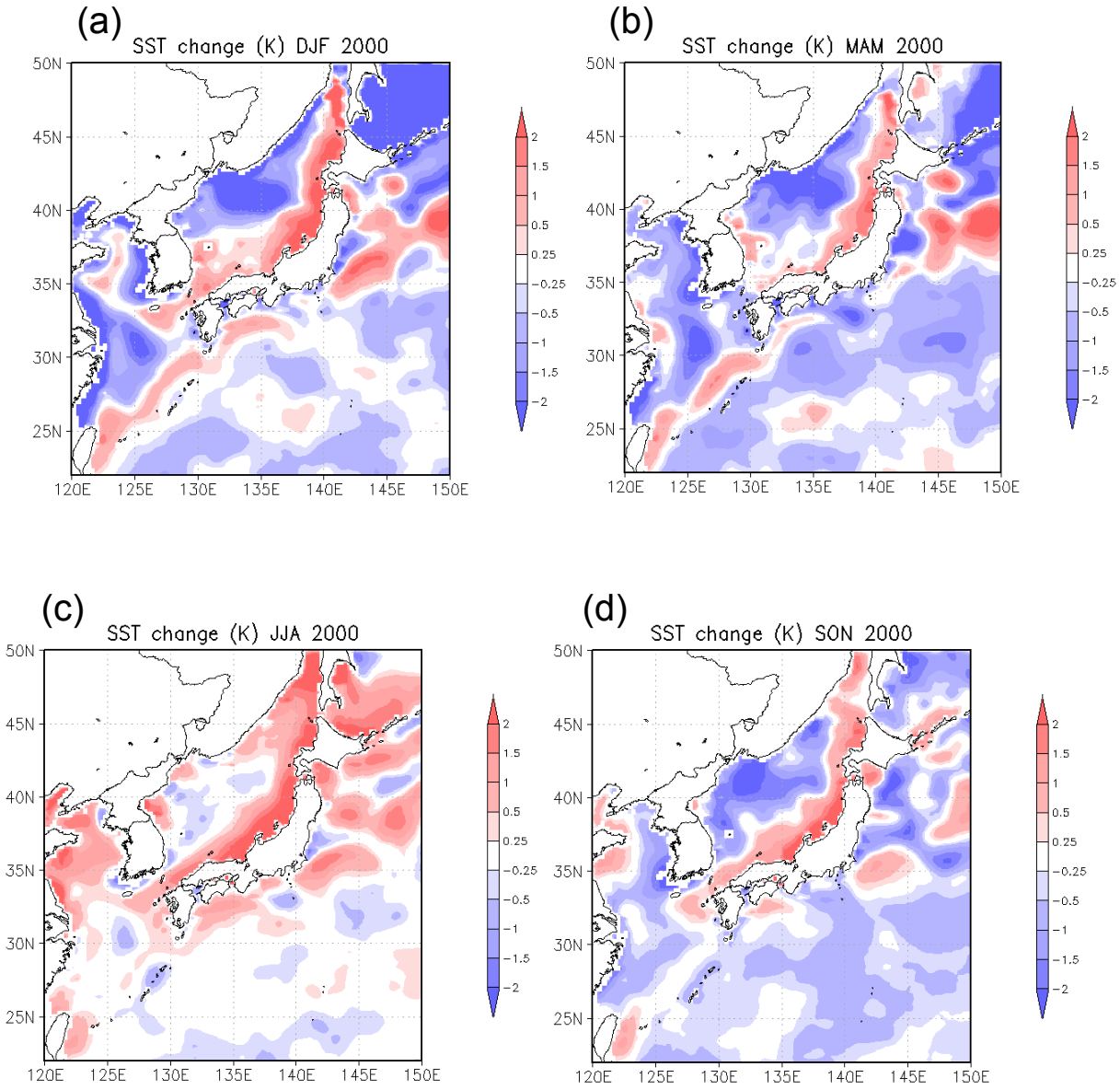

Fig. 3.16 Differences in SST between MGDSST and JRA-SST in (a) winter, (b) spring, (c) summer and (d) fall. The unit is °C.

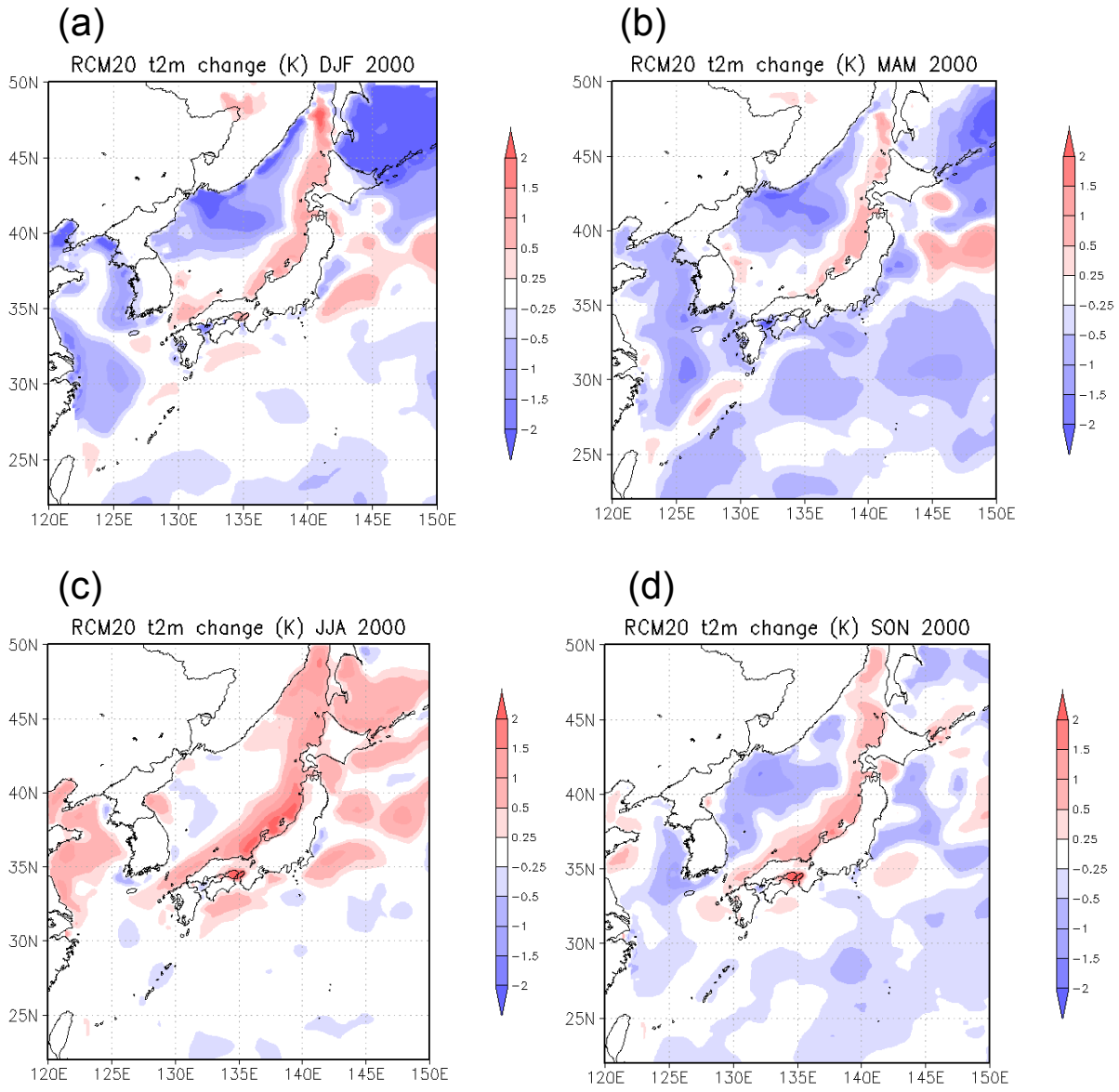

Fig. 3.17 Differences in surface temperature between MGDSST-run and JRA-run in (a) winter, (b) spring, (c) summer and (d) fall. The unit is °C.

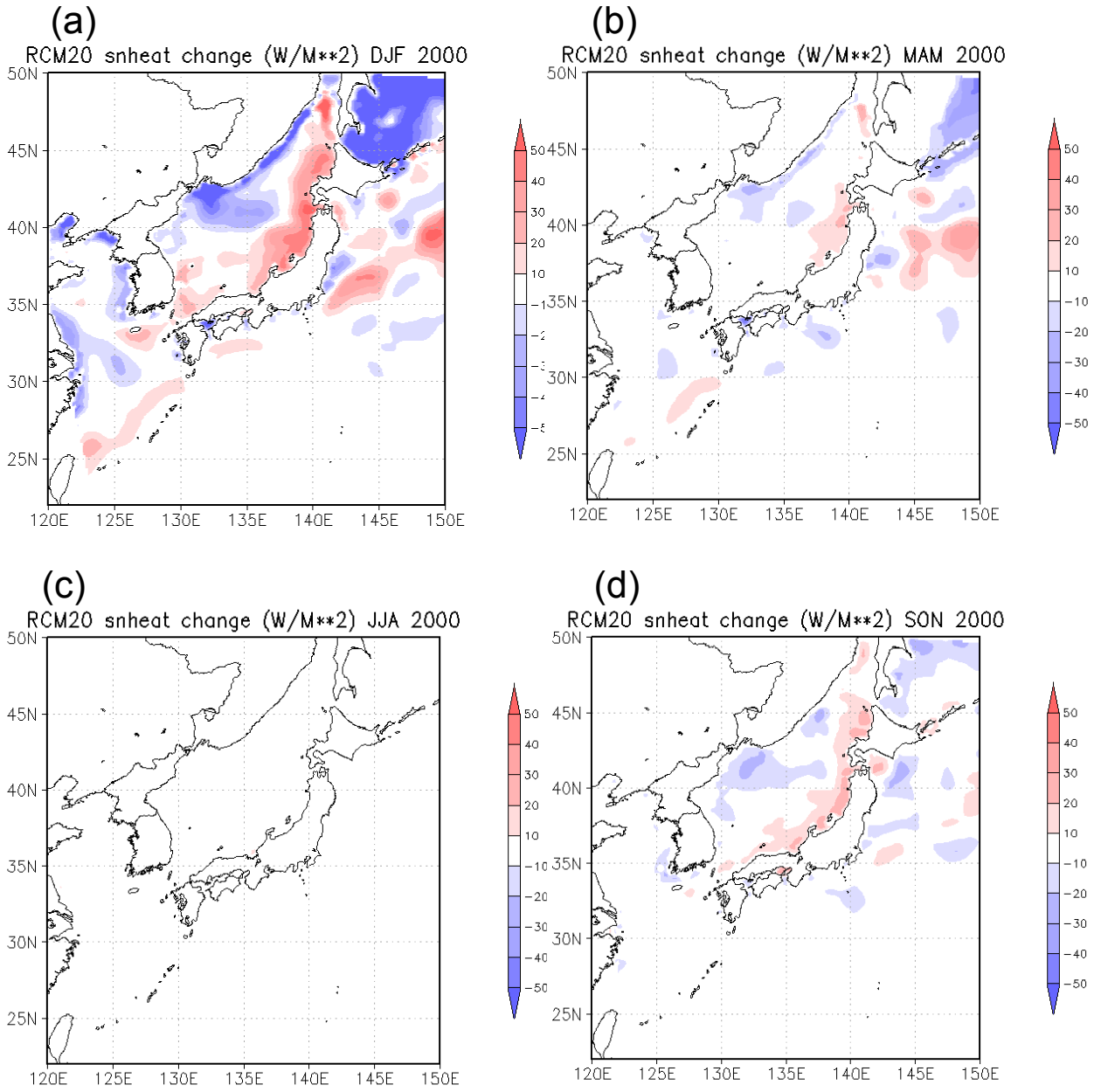

Fig. 3.18 Differences in sensitive heat flux between MGDSST-run and JRA-run in (a) winter, (b) spring, (c) summer and (d) fall. The unit is W m^{-2}.

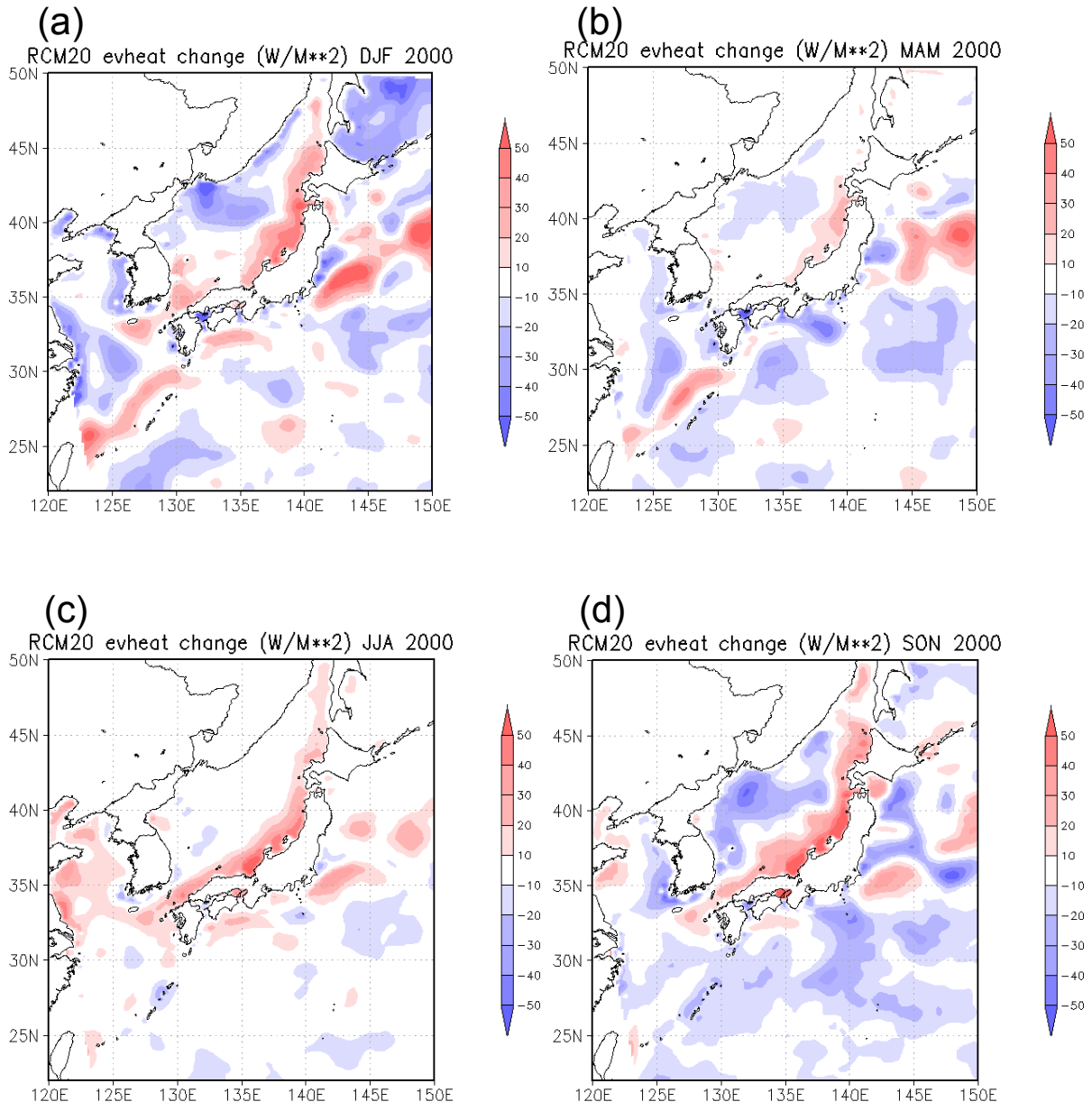

Fig. 3.19 Differences in latent heat flux between MGDSST and JRA-SST in (a) winter, (b) spring, (c) summer and (d) fall. The unit is W m^{-2}.

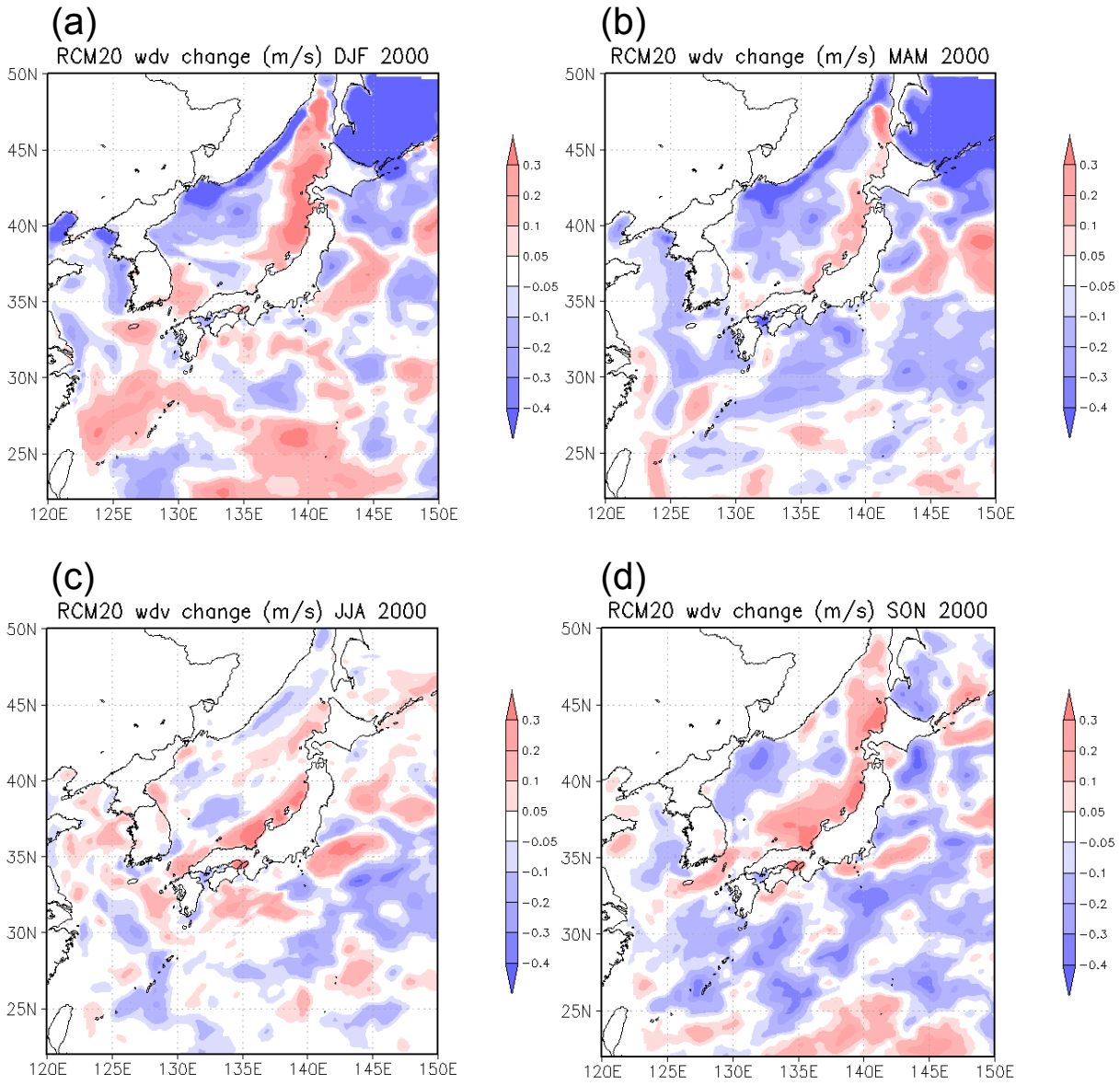

Fig. 3.20 Differences in wind speed between MGDSST and JRA-SST in (a) winter, (b) spring, (c) summer and (d) fall. The unit is m s^{-1}.

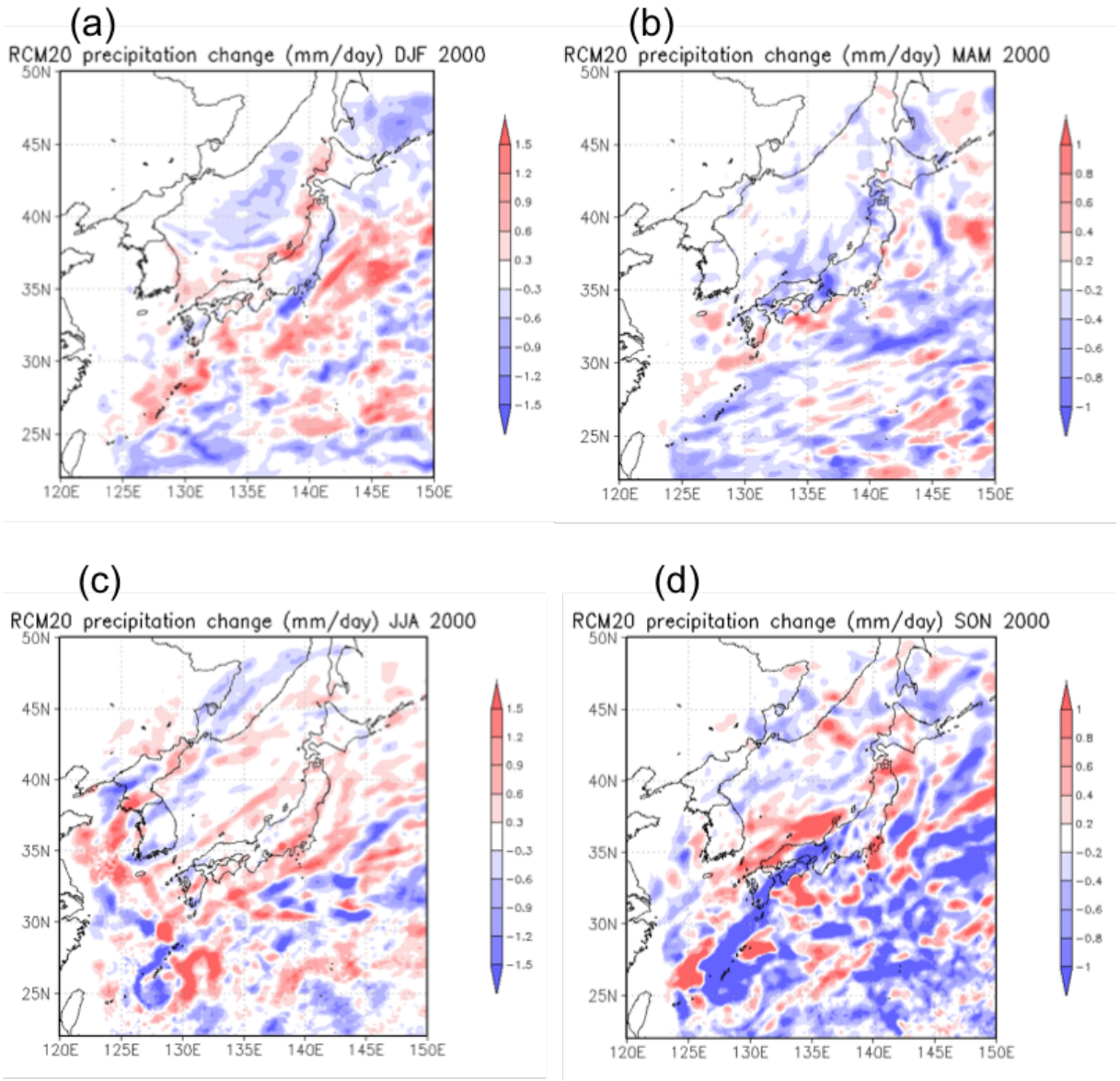

Fig. 3.21 Differences in precipitation between MGDSST-run and JRA-run in (a) winter, (b) spring, (c) summer and (d) fall. The unit is mm day^{-1}.

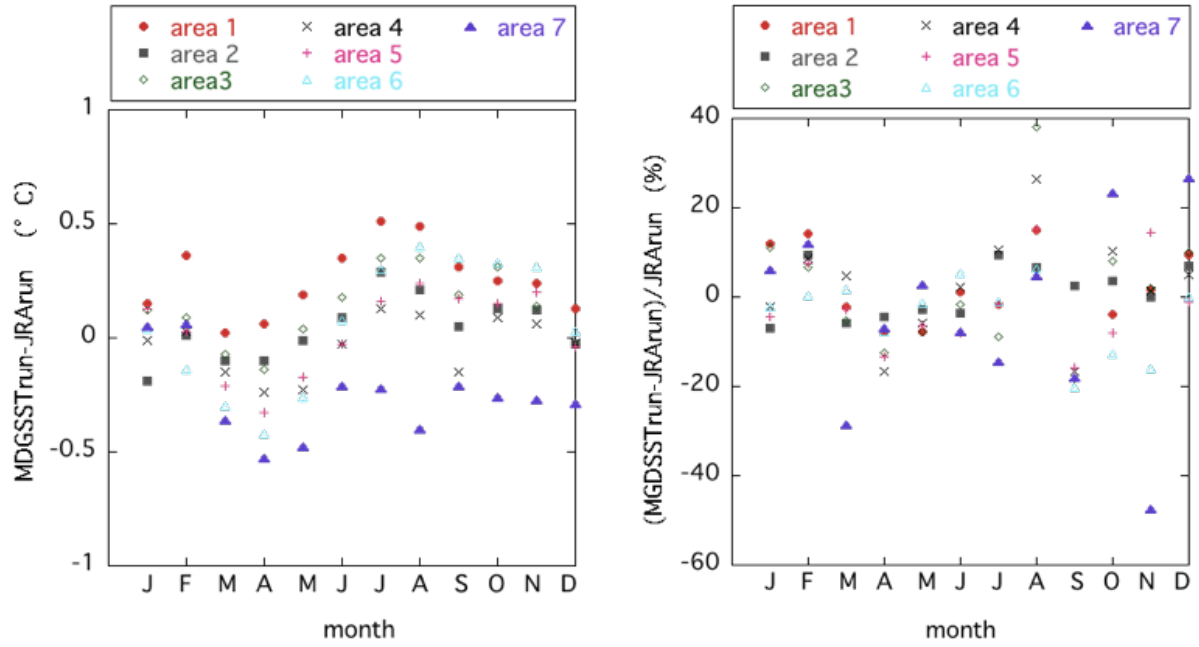

Fig. 3.22 Monthly differences between MGDSST-run and JRA-run averaged over seven climatic areas as shown in Fig. 3.3.

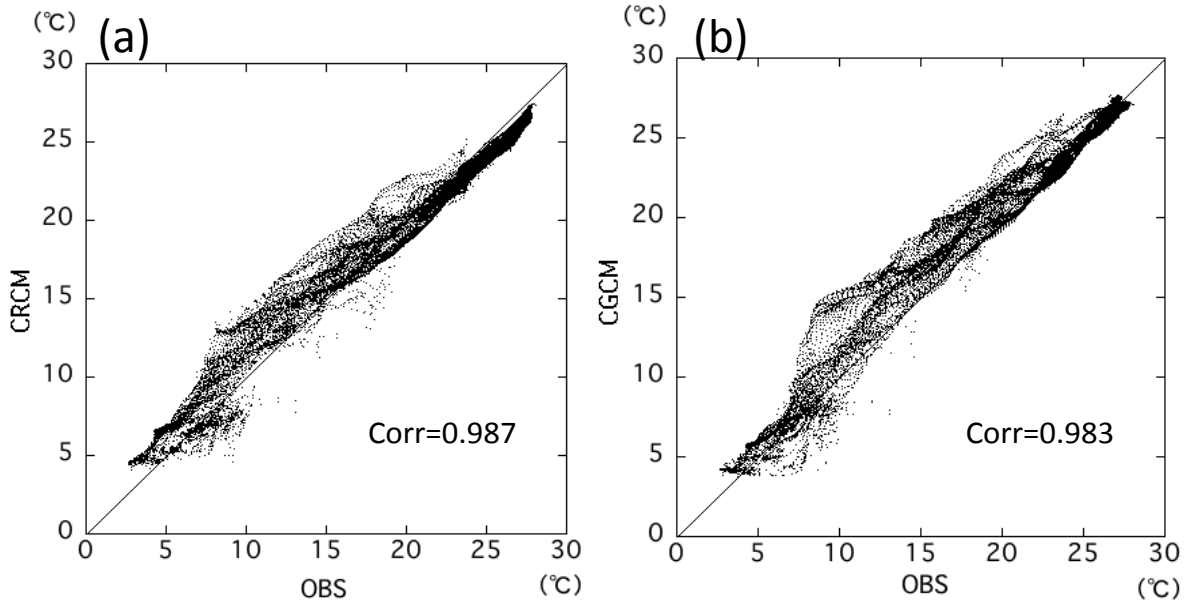

Fig. 3.23 Comparison of simulated and observed 10-year averaged annual mean SST. (a) CRCM-run, (b) CGCM-run.

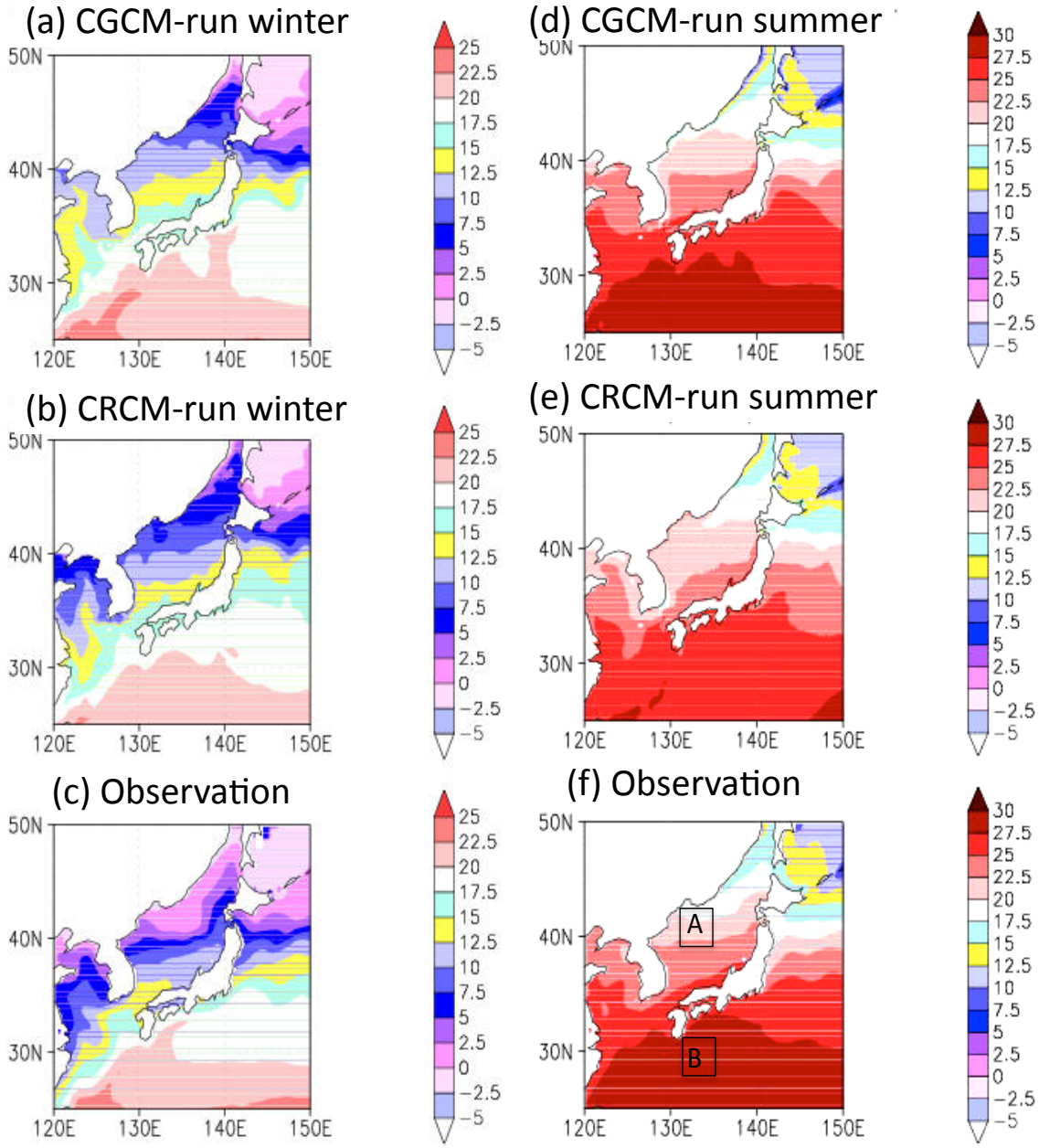

Fig. 3.24 Seasonal mean SST (°C) in winter simulated by (a) CGCM-run, (b) CRCM-run and (c) observation, and in summer simulated by (d) CGCM-run, (e) CRCM-run and (f) observation. Observation used here is MGDSST made by JMA.

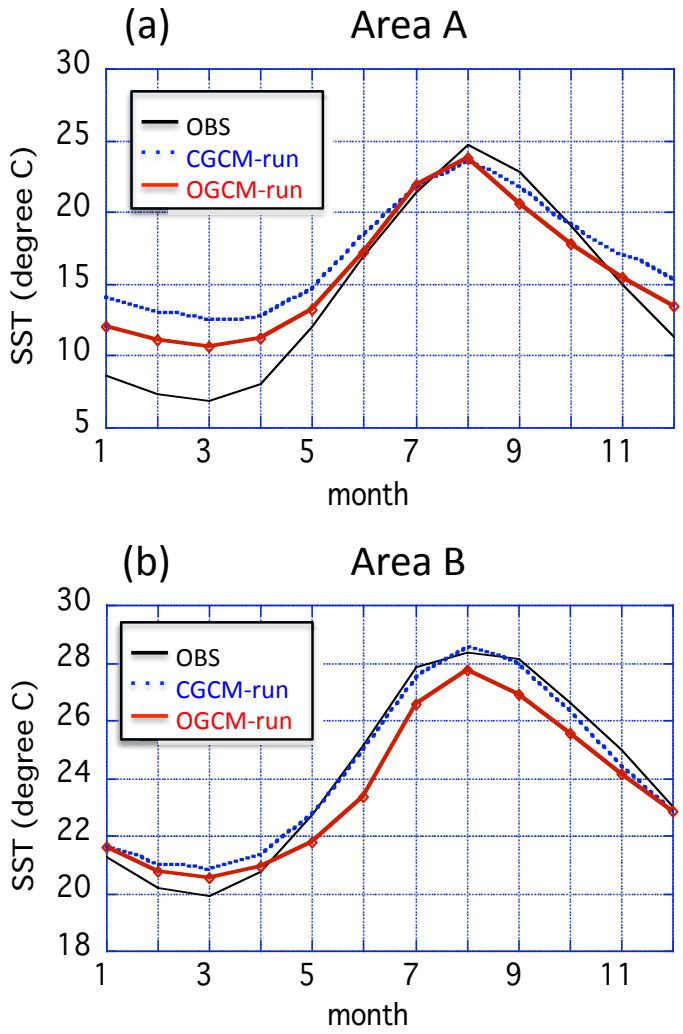

Fig. 3.25 10-year mean monthly SST averaged over (a) area A and (b) area B in Fig. 3.24 f. Black: observation; dotted blue: CGCM run; red: CRCM run.

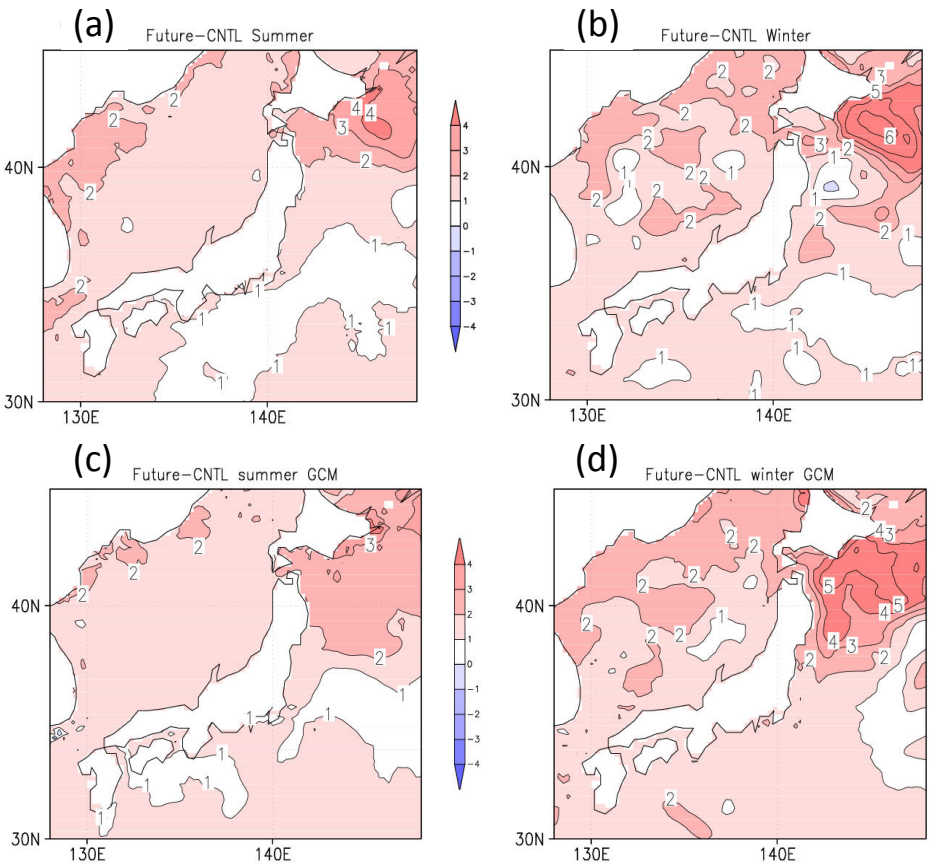

Fig. 3.26 Differences in 10-year averaged seasonal SST (°C) between present climate runs and future projection run (a) the CRCM-run in summer (July, August and September), (b) the CGCM-run in summer, (c) the CRCM in winter (January, February and March) and (d) the CGCM-run in winter.

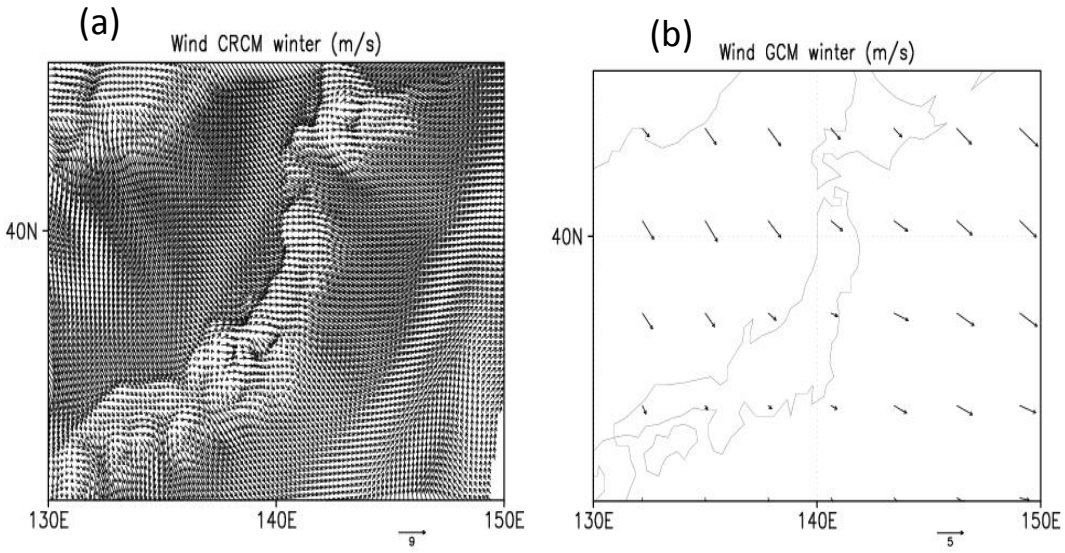

Fig. 3.27 10-year averaged surface wind (m s^{-1}) in winter for the future projection run simulated by (a) the CRCM and (b) the MRI-CGCM2.

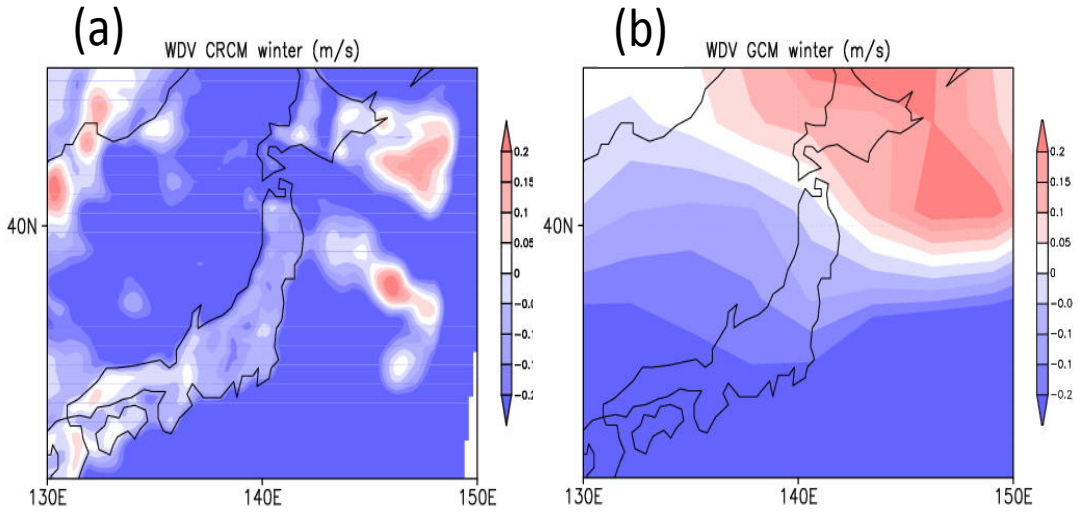

Fig. 3.28 10-year averaged surface wind speed differences (m s^{-1}) between future projection and present climate run.

CHAPTER 4 The influence of Kuroshio Large Meander on climate around Japan based on a regional climate model

In previous chapter, we evaluated precipitation performance of RCM20 and examined atmospheric responses with high-resolution SST data. Moreover, atmospheric influences on SST were examined using MRI-CRCM employing a two-way method. The results showed the atmospheric responses are closely related to the ocean through SST. In Chapters 4 and 5, based on Murazaki et al. (2015), we describe a detailed investigation about the influence of the Kuroshio on the climate around Japan using NPOGCMv.2 and RCM20 to quantitatively estimate the impact of the Kuroshio LM and to clarify the mechanism of how the cold SST pool influences neighboring convection activity.

4.1 Simulation design

NPOGCMv.2 and RCM20 were used in this study. Initially, for the simulation using NPOGCM, 26-year-monthly-averaged datasets of surface wind, surface air temperature (SAT), radiation, precipitation and Sea level pressure (SLP) were created by JRA-25 as a forcing data. The 20-year integration was then performed as a spin-up. Using the spin-up results as an initial condition and the 6-hourly JRA-25 atmospheric data as the forcing data, the NPOGCM simulation was run from 1 January 1979 to 31 December 2004. The last 20 years of the resulting SST and sea ice data were used as lower boundary conditions for RCM20. Initial and lateral boundary conditions were provided by the 6-hourly data from JRA-25. A 20-year simulation using RCM20 was run from 1 January 1985 to 31 December 2004 (hereafter, OGCM-run).

It is difficult to identify atmospheric responses to changes in SST using the OGCM-run results alone because several factors influence the atmosphere such as the monsoon, global warming, and the westerly jet. Therefore, we used the long-term integration results from RCM20 (JRA-run; Murazaki et al. 2010), using the JRA-SST as the lower boundary condition, as a

control run. The only difference between the OGCM-run and JRA-run was the lower boundary conditions. The JRA-run used an observation-based SST with a resolution of 1.125 °, whereas the OGCM-run used the NPOGCM high-resolution simulation result with a resolution of 1/10 ° around Japan. These two runs were compared to detect detailed atmospheric responses to changes in the Kuroshio's path (Fig. 4.1). To characterize atmospheric responses to the Kuroshio LM more clearly, we investigated the seasonally averaged field of surface turbulent heat flux and EPT. We also examined transient events such as the frequency of steep gradients in EPT and high-intensity rainfall events.

The EPT of a volume of air is greater when its temperature is high or the air contains a large amount of water vapor. Heavy rain is closely related to EPT at the 500 m level (Kato 2011). Kato (2011) suggested that the conventional index using EPT at the 850 hPa level at the time of heavy rainfall is not suitable because water vapor from the sea is stored in a lower convective mixed layer up to ~1 km deep over the sea. He compared EPT at the 500 m level, SLP, and wind vectors in heavy rainfall areas, and concluded that inflow from the south of an air mass with high EPT at the 500 m level plays an important role in the generation and development of cumulus clouds. Because RCM20 does not predict conditions at the 500 m level, we used predicted EPT at the 950 hPa level instead as air pressure at 500 m is generally close to 950 hPa (Kato 2009).

We also investigated horizontal and vertical EPT gradients over the ocean around the Kuroshio LM. The vertical EPT gradient serves as an index of atmospheric stability, which is closely related to atmospheric convection. The horizontal EPT gradient increases where two different air masses meet. Weather fronts are expressed more clearly by the horizontal EPT gradient than the temperature gradient, especially in the rainy season. The occurrence of a strong EPT gradient indicates that active front zone exists there (Ninomiya and Akiyama 1992; Zhou et al. 2004).

4.2 Twenty-year averaged results of the long-term integration of NPOGCM

We compared the 20-year averages of SST for winter (December–February) and summer (June–August) from JRA-25 and NPOGCM with MGDSST, and found that JRA-SST does not sufficiently resolve the detailed features of the ocean currents (Figs. 4.2a and 4.2d). MGDSST effectively showed the fine-scale SST distribution associated with the Kuroshio flow along the Pacific coast of Japan (Figs. 4.2b and 4.2e). NPOGCM showed the transport of warm water to the southern coast of Japan by the Kuroshio in detail (rectangle in Figs. 4.2c and 4.2f), however, this model also had some biases. During winter, the 22 °C isotherm predicted by NPOGCM reached the Kii Peninsula (33 °N 136 °E; Fig. 4.2c), whereas those indicated by the MGDSST and JRA-SST data lay south of 33 °N (Figs. 4.2a and 4.2b). In summer, the 28 °C isotherm predicted by NPOGCM (Fig. 4.2f) was north of those indicated by the MGDSST and JRA-SST data (Figs. 4.2d and 4.2e).

To evaluate the annual changes and trends in the area-averaged SST, the sea area surrounding Japan was divided into four zones according to SST analysis conducted by JMA (2006), as shown in Fig. 4.3. The 20-year SST averages for each zone were calculated using the NPOGCM results, JRA–SST and MGDSST, and the anomalies were determined by subtracting the 20-year averages from the monthly averaged SST. Figure 4.4 shows the 12-month moving average of the area-averaged SST anomalies. In the Sea of Japan (zone 1 in Fig. 4.3), a remarkable increase over the last 100 years (approximately 1.7°C) was demonstrated by the analysis of the JMA observations (Takatsuki et al. 2007).

Compared with the other three zones, the Sea of Japan area exhibits a steeper slope, in agreement with the observations. Twelve-month moving averages in zones 3 and 4 show a good agreement between the NPOGCM result and the observations. Zones 1, 3, and 4 have a higher correlation coefficient between MGDSST and NPOGCM (more than 0.9), while that of zone 2 is lower (approximately 0.7). Because the SST of this region is highly influenced by the strength of the Oyashio, a cold current from the north, NPOGCM may be biased in the area influenced by

the Oyashio. In this study, however, we focus on the Kuroshio meandering at lower latitudes where this influence is minimal and leave the phenomenon at high latitudes for future research.

4.3 Comparison of JRA-run and OGCM-run

In this section, we compare the results of the 20-year continuous simulation of RCM20 with both the JRA-run and OGCM-run and describe how the detailed structure of Kuroshio influences the atmospheric climate conditions.

Figure 4.5 shows the 20-year-averaged January mean results of the difference between the SAT and SST, the heat flux (latent heat flux + sensible heat flux), surface water vapor flux and its convergence and divergence, and the precipitation for the JRA-run and OGCM-run. The SAT–SST provides an indication for atmospheric stability; while SAT demonstrates a gradual meridional distribution over the ocean, the SST distribution shows a steep incline at the Kuroshio front. Thus, Kuroshio's flow path can be inferred by looking at the SAT–SST (Tokinaga et al. 2009). They used shipboard and satellite observations from both winter and summer to investigate the SAT–SST in the area that runs across the Kuroshio and assessed the impact of the current on regional cloud and fog conditions. They demonstrated that the SAT–SST falls below −6 °C along the Kuroshio front and becomes highly unstable. The SAT–SST plot of the OGCM-run (Fig. 4.5b) shows minimum values (approximately −7 °C) along the Kuroshio front. On the other hand, the steep incline and narrow band of minimum values are not clearly found on the SAT–SST data of the JRA-run (Fig. 4.5a). Figures 4.5c and 4.5d show the total heat flux of the JRA-run and OGCM-run, respectively. The location of the maximum heat flux of OGCMM-run corresponds to the location of the minimum SAT–SST contours. The maximum heat flux value is approximately 500 W m^{-2}, which agrees with satellite observation winter climatology (approximately 450 W m^{-2}) and shipboard observation values (approximately 520 W m^{-2}) shown in Tokinaga et al. (2009). Figures 4.5e and 4.5f show the surface water vapor flux and its convergence and divergence. In the winter season in Japan (Fig. 4.5e), a strong monsoon from the continent hits the backbone range, producing a strong convergence on the Japan Sea

side followed by a divergence on the Pacific Ocean side, the other side of the backbone range. Subsequently, a weak convergence appears again over the sea, indicated by the ellipsoidal regions in Figs. 4.5e and 4.5f. The magnitude of the convergence on the Kuroshio front is greater in the OGCM-run than that in the JRA-run. This convergence contributes to the increase in precipitation on the Kuroshio front, as shown by the precipitation distribution in Figs. 4.5g and 4.5h.

Figure 4.6 shows the 20-year-averaged July mean results of the SAT–SST, heat flux, water vapor flux and its conversion and divergence, and rainfall. In July, the OGCM-run shows a difference between the SAT and SST of approximately −1°C (Fig. 4.6b) and a heat flux from the ocean to the atmosphere of approximately 120 W m^{-2} (Fig. 4.6d)—less than a quarter of the values in winter. The contrast in temperatures and heat flux is not represented clearly in the JRA-run results (Figs. 4.6a and 4.6c). Tokinaga et al. (2009) reported that their satellite image analysis showed a maximum heat flux of approximately 180 W m^{-2} on the Kuroshio front in summer, which is comparable in magnitude to that in the OGCM-run (Fig. 4.6d).

The average values of the JRA-run and OGCM-run from 1985 to 2004 in the Kuroshio front area (rectangles in Figs. 4.6b) are shown in Table 4.1. The SAT–SST of the OGCM-run is 0.15°C higher than that of the JRA-run, indicating a decrease in the atmospheric stability. As a result, the heat flux from the ocean shows an increase of approximately 10 % with reinforced convergence, which leads to an increase in the average annual precipitation of approximately 8 mm $month^{-1}$ (Figs. 4.6g and 4.6h).

Next, we demonstrate whether the experiment reproduced realistic atmospheric responses (Fig.4.7). The GCM-run, replaced the SST to the result of NPOGCM, shows precipitation reproducibility in the Sea of Japan side (area 3 in Fig. 3.3) is improved in winter. For example, precipitation amount in January increases more than 40 mm $month^{-1}$ in the Sea of Japan side (Fig. 4.7a), which improved from underestimation of JRA-run result as shown in Fig. 3.4e. In June, the rain band over the Kuroshio appears clearly (Fig. 4.7i), and it corresponds well to the observation result of by Sasaki et al. (2012).

Figure 4.8 depicts the differences in monthly SST, and monthly precipitation between the JRA-run and OGCM-run is shown in Fig. 4.9. The maximum difference in precipitation occurred in June, Meiyu-baiu rainy season, extending to 3 mm per day. This result corresponds well to the result of the sensitivity experiment by Sasaki et al. (2012). After the end of the baiu, the precipitation difference between the JRA-run and OGCM-run became small but still exist on the Kuroshio.

To understand the influence on the vertical atmospheric structure due to Kuroshio, we show a cross-section of the difference in vertical wind along A–B in Fig. 4.8. In the winter season, upward motion occurred near 127 °E–128 °E. This position corresponded to the position of the Kuroshio but slightly spread to the east. The deviation of upward motion became gradually more prominent from April to June (Fig. 4.9d–e), which corresponded to the monthly precipitation differences (Fig. 4.8d–e). The upward motion around the 500 hPa level became gradually stronger in the vertical direction from April through June. Xu et al. (2011) showed that precipitation in the spring on the ECS is mainly related to the deep atmospheric heating of cumulus convection. Furthermore, using reanalysis data, Sasaki et al. (2012) showed that the diabatic heating rate and the upward motion on the Kuroshio are at the maximum around the 400–500 hPa level in June. Our result is consistent with their results and indicates that the Kuroshio affects deep convection in the ECS during the baiu season.

4.4 Variation of the Kuroshio path and its influence on climate around Japan

The SST distribution and the corresponding atmospheric field around Japan area were shown in the previous section. A unique path change of Kuroshio occurs in a longer time scale besides seasonal variation in the Kuroshio area. Kuroshio is known for its meandering behavior; that is, Kuroshio sometimes deviates from its SP along the coast of Japan, and instead meanders to the southeast, away from the coast. This flow pattern is known as the Kuroshio LM. This section describes the impact of atmosphere by the path of the Kuroshio variations.

4.4.1 Changes in Kuroshio paths calculated by NPOGCM

In this sub section, the reproducibility of variations in the Kuroshio's paths is demonstrated. Although there are various views regarding the indicator of the Kuroshio LM, in this study, we adopt the southernmost latitude with a water temperature of 15 °C at a 200 m depth, according to the definition given by Kawai (1972). Based on this definition, the large Kuroshio meander occurs when the southernmost latitude of the Kuroshio front is stably located at latitude 32 °N between 136 °E and 139 °E. On the sea surface, weather significantly affects water temperature. We therefore used subsurface temperature at a depth of 200 m, rather than SST, to identify the Kuroshio LM. It is well-known in the oceanographic community that this method gives results similar to those given by other methods such as the report on tidal level differences between two points on both the sides of Shiono Cape at the southern tip of the Kii Peninsula (JMA 2007).

With respect to simulating the timing of the Kuroshio LM, the model results indicate that the current was in a highly stable SP phase from 1987–1996, and subsequently moved to a prevailing LM phase (Fig. 4.10). However, the JMA observational data (JMA 2007) show that the Kuroshio was in the SP state for most of the study period, except for three relatively short LM phases: December 1986 to July 1988, December 1989 to December 1990, and July 2004 to August 2005. Therefore, the model did not successfully predict the timing of LM phases. Tsujino et al. (2013) suggested that the net depth-integrated Kuroshio transport off southern Japan, whose mean quantity and variability are affected by the basin-scale wind stress field, strongly influences the path selection of the Kuroshio. Specifically, a weak (strong) Kuroshio favored LM (SP). In the NPOGCM simulation, the net Kuroshio transport was about 40 Sv in the SP period (1989–1996) whereas it was 20 Sv in the LM period (1997–2004) (not shown). This is consistent with the suggestion of Tsujino et al. (2013), even though some positive feedback effects should be taken into account. On the basis of the observations, Imawaki et al. (2001) estimated the net Kuroshio transport to be 42 Sv as a seven-year average in the period from 1992 to 1999, during which the Kuroshio was largely in the SP state. Thus, the net Kuroshio transport of NPOGCM was consistent with the observational estimate in the SP state. The net Kuroshio transport should

have been larger in the prevailing LM phase in the NPOGCM simulation, although further investigations are required to confirm this conjecture. However, Tsujino et al. (2013) also pointed out that mesoscale eddies are involved in the transition of the Kuroshio path, implying that it would be generally still difficult for the current OGCMs to get the Kuroshio LM timing right. In this study, we will focus on the atmospheric responses to the LM that operate through heat and water vapor exchanges, and will not pursue the mechanism causing the timing of the Kuroshio LM.

The SST distribution patterns characteristic of the two states of Kuroshio are compared in Fig. 4.11. When the system switches from the SP to the LM state, SST decreases in the area where Kuroshio dominates in its SP state, and increases in the area covered by the LM path. The effects of the change between the two states were not obvious in the JRA-SST data (Figs.4.11a, 4.11d, and 4.11g). The MGDSST data, however, showed a striking decrease in SST around 33°N 138°E and an increase around 35°N 142°E (Figs. 4.11b, 4.11e and 4.11h).

The NPOGCM SST predictions also showed the effects of the change in state, but suggested that the Kuroshio extended further south than indicated by the MGDSST data (Figs. 4.11c, 4.11f and 4.11i). As a result, the cold pool caused by the Kuroshio LM was relatively overestimated by NPOGCM (Fig. 4.11i).

The Kuroshio LM state simulated by NPOGCM was overestimated in terms of both area and duration (Figs. 4.10 and 4.11). However, because the main purpose of this study is to quantify the impact of the Kuroshio LM on the climate around Japan, the NPOGCM run does not necessarily need to accurately replicate the Kuroshio LM period. The simulation may be considered successful if it reproduces the two characteristic paths of the Kuroshio. The exaggerated area of the LM is preferable because it will cause RCM20 to predict stronger atmospheric responses to the LM than the MGDSST data would. The stronger atmospheric response can then be taken as an upper bound of possible atmospheric responses to the Kuroshio LM. In fact, the LM did occupy a considerably larger area in the early 1960s and late 1970s (Kawabe 1995). Furthermore, because variations in the MGDSST data may be dampened by the

application of optimum interpolations, these data might be insufficient to resolve the detailed features of intense ocean currents such as the Kuroshio. The SST predicted by NPOGCM, however, is at least based on the physical law of the model. Therefore, we used the SST fields simulated by NPOGCM when running RCM20.

4.4.2 Atmospheric response to Kuroshio using RCM20

Changes in the frequency of steep gradients in equivalent potential temperature and rainfall intensity With respect to the difference in total surface turbulent heat flux (latent plus sensible heat flux, defined positive upward, hereafter, surface heat flux) in winter between the LM and SP states predicted by OGCM, there was a region with negative values (cold pool), reaching minima of approximately −80 W m^{-2} between 33 °N 134 °E and 34 °N 141 °E. This is the northern side of the Kuroshio front during LM phases (Fig. 4.12a). Regions with positive values (warm pools), reaching a maxima of approximately 60 W m^{-2}, were spread out along the upstream KE front region between 34 °N 140° E and 36 °N 146 °E. In the JRA-run, the area of moderate positive values of less than 32 W m^{-2} was spread out widely over the ocean (Fig. 5.10c).

Surface heat flux in summer is relatively weak, and the change in surface heat flux between the LM and SP states was correspondingly weak with minima of approximately −46 W m^{-2} in the cold pool (Fig. 4.12b). This pattern corresponds well with the pattern of change in SST (Fig. 4.12i). In the JRA-run (Figs. 4.12c and 4.12d), differences were even smaller (less than 16 W m^{-2}) and were almost uniformly spread over the ocean. There was no statistically significant difference ($p < 0.1$) in surface heat flux changes in the simulation area from SP to LM states between the OGCM and the JRA-run, with the exception of the areas surrounding the Kuroshio LM (not shown). Therefore, the SST changes caused by the Kuroshio LM in the OGCM-run are likely to be responsible for the differences in surface heat flux.

Changes in surface heat flux from the ocean to the atmosphere affect both temperature and water vapor in the atmospheric boundary layer. In the OGCM-run in winter, EPT in the cold

pool was strongly reduced during the LM state relative to the SP state (Fig. 4.13a), however, the JRA-run showed only a weak negative area north of 32 °N and a weak positive area south of 32 °N (Fig. 4.13c). For the summer months, a weak negative area appeared near 33 °N 140 °E in the OGCM-run (Fig. 4.13b). Given the fact that EPT in this area increases in the JRA-run as a result of natural climate variability (Fig. 4.13d), the change of EPT due to the Kuroshio LM probably shows a similar pattern in both winter and summer when the natural variability is subtracted.

The change in surface heat flux caused by the Kuroshio LM affects the change in both EPT distribution and the horizontal EPT gradient related to atmospheric front activity. The LM causes the winter frequency of horizontal EPT gradients exceeding 0.1 K km^{-1} (hereafter, steep $|\nabla_h \theta_e|$) at the 950 hPa level to decrease over an area stretching from the northern edge of the cold pool to the southern edge of the warm pool (33 °N 134 °E to 34 °N 147 °E; Fig. 4.14a). The frequency of steep $|\nabla_h \theta_e|$ increases in an area that spreads out from the southern edge of the cold pool. These changes are more pronounced in summer than in winter (Fig. 4.14b). The larger changes in summer may be related to the fact that the frequency of steep $|\nabla_h \theta_e|$ in summer is more than double of that in winter. For example, at a location of large change in the surface heat flux (33.6°N 138°E), the seasonal average of steep $|\nabla_h \theta_e|$ frequency based on 3-hourly sampling is about 60 (46) out of 240 data times per month for the SP (LM) state in summer. In winter, these figures are about 23 and 16 per month for the SP and LM state, respectively. In the JRA-run, however, change in the frequency of steep $|\nabla_h \theta_e|$ was relatively small (Figs. 4.14c and 4.14d). These distributions were similar to the results of the OGCM-run (Figs. 4.14a and 4.14b), except for the areas surrounding the Kuroshio LM.

To analyze the influence of the Kuroshio LM on the atmosphere in more details, we examined the rate of change in frequency of steep $|\nabla_h \theta_e|$ predicted by both the OGCM and JRA-run along the line 33.6°N, where change in surface heat flux was the greatest (Fig. 4.12a). The rates of change in the frequency of steep $|\nabla_h \theta_e|$ predicted by the two runs diverged near 134°E and converged near 146°E in winter, whereas they diverged near 136°E and converged

near 145°E in summer (Fig. 4.15). The difference between the two runs was approximately 35% in winter and 30% in summer. Frequency decreased in a relatively large area that extended eastward from the cold pool. The following may constitute a possible explanation.

In general, the meridional EPT distribution makes a substantial contribution to $|\nabla_h \theta_e|$. When the Kuroshio is in the LM state, $|\nabla_h \theta_e|$ over the northern edge of the cold pool, around 33 °N and 134–140 °E, decreases because the lower EPT in the cold pool reduces the differences in EPT between the north and south. Moreover, it decreases in the extended eastward zone around 34 °N and 140–146 °E because the increase in the EPT over the warm pool weakens the contrast between this air and the humid air from the south.

The change in the frequency of high intensity rainfall events, defined as more than 1 mm of precipitation within three hours, is shown in Fig. 4.16. The JRA-run predicted a weak decrease in the cold pool area (Fig. 4.16c). The OGCM-run, however, predicted change corresponding to the changes in surface heat flux during winter months (Fig. 4.13a), i.e., the frequency decreased in the cold pool but increased in the warm pool (Fig. 4.16a). The maximum frequency change was about 8 times per month. In summer, the pattern was similar to winter (Fig. 4.16b), with the addition of a region of strong decline in the frequency of high intensity rainfall events over the much-weakened cold pool. As shown in Figs. 4.12 and 4.14, there were few differences between the OGCM-run and the JRA-run outside the area surrounding the Kuroshio LM.

Figure 4.17 shows the rate of change in the frequency of high intensity rainfall events, as predicted by the OGCM-run and the JRA-run, along the line A–B shown in Fig. 4.12a. The rates of change predicted by the two simulations began to diverge near 135.5 °E and again converged near 143 °E, which corresponds almost exactly with the cold pool area. The difference between the two runs was approximately 30-35 % for summer and 20-25 % for winter.

4.4.3 The seasonal averaged atmospheric variations between LM and SP by removing the natural fluctuation

We now examine the results of RCM20 regarding the response of the atmosphere around

Japan to the different Kuroshio flow paths. To find the variation between the atmospheric response to the Kuroshio LM period and the direct flow period, we define the anomalies $\Delta X_{ogcm}(x, t)$ and $\Delta X_{jra}(x,t)$ of the monthly mean climate parameter as a function of time and location as follows.

$$\Delta X_{OGCM}(\mathrm{x},\mathrm{t}) = X_{OGCM}\ (\mathrm{x},\mathrm{t}) - \overline{X_{OGCM}(x)} \qquad (4-1)$$

$$\Delta X_{JRA}(\mathrm{x},\mathrm{t}) = X_{JRA}\ (\mathrm{x},\mathrm{t}) - \overline{X_{JRA}(x)} \qquad (4-2)$$

In equation (4-2), $X(x,t)$ represents a physical quantity as a function of a location, x and time t. The subscripts *OGCM* and *JRA* indicate the OGCM-run and JRA-run, respectively, and the over bar $\bar{}$ and *t* represent the monthly 20-year-averaged value and a period of one month, respectively. Thus, the anomalies $\Delta X_{ogcm}(x, t)$ and $\Delta X_{jra}(x, t)$ represent the deviation from the monthly climate data. When we compare the JRA-run and OGCM-run results, it is difficult to determine whether the differences arise from the different average field or 20-year trend or the changes in the Kuroshio path. Therefore, we define the impact quantity (anomaly variation) as follows:

$$\Delta f\ (\mathrm{x},\mathrm{t}) = \Delta X_{OGCM}\ (\mathrm{x},\mathrm{t}) - \Delta X_{JRA}\ (\mathrm{x},\mathrm{t}) \qquad (4-3)$$

By the equation (4-3), the impact on the atmosphere due to detailed structures of the SST can be revealed by removing the differences in the average field between the JRA-run and OGCM-run. To quantitatively clarify the variation in the impact on the atmosphere of the two Kuroshio paths, we examined $\Delta h(x)$, the variations in atmospheric characteristics between the Kuroshio SP and LM periods,

$$\Delta h(x) = \overline{\Delta f(x,t)_{LM}} - \overline{\Delta f(x,t)_{SP}} \qquad (4-4)$$

To test whether there was a significant atmospheric difference between these periods, a t-test was performed at the 90 % significance level.

Using the above definition, the degree of change in total heat (latent heat and sensible heat) flux was calculated (positive upward). Analysis of the change in total heat flux in winter

(December–February) between LM and SP phases showed a region with negative values (cold pool), reaching minima of approximately –120 W m^{-2}, between 33 °N 134 °E and 34 °N 141 °E, which is the north side of the Kuroshio front during LM phases (Fig. 4.18a). Regions with positive values (warm pools), up to approximately 80 W m^{-2}, were spread out along the LM front region between 34 °N 140 °E and 36 °N 146 °E. In spring (March–May) the cold pool moved slightly closer to the Japanese islands (Fig. 4.18b). The total heat flux in summer (June–August) is relatively weak, and the pattern of change in heat flux was correspondingly weak (Fig. 4.18c). In autumn (September–November) the pattern began to strengthen once again, but the warm pool to the south of the cold SST pool had almost disappeared (Fig. 4.18d). This pattern of change in total heat flux corresponds well with the pattern of change in SST (Fig. 4.11i).

Changes in the frequency of high intensity rainfall events, defined as 3-hour rainfall totals exceeding 1 mm, corresponded to changes in heat flux, and in winter decreased in the cold pool but increased in the warm pool (Fig. 4.19a). The maximum frequency change was about eight occurrences per month. The pattern was similar for spring (Fig. 4.19b), but in summer a region of strong decline in the frequency of high intensity rainfall events developed (Fig. 4.19c) over the much-weakened cold pool (Fig. 4.18c). In autumn the spread of the area of decrease in frequency of high intensity rainfall events was about the same as the case of summer (Fig. 4.19d), although its pattern was not corresponding well to the cold pool unlike summer case (Fig.4.18d).

The area of negative change in the winter frequency of steep $|\nabla\theta_e|$ at the 950 hPa level spread from the northern edge of the cold pool to the southern edge of the warm pool (33 °N 134 °E to 34 °N 146.5 °E; Fig. 4.20a). The zone of increase in the frequency of steep $|\nabla\theta_e|$ spread out from the southern edge of the cold pool. In spring the region of decrease spread northward, while the region of increase to the south of the Kuroshio LM region took on a dipole structure (Fig. 4.20b). The region of decrease became more pronounced in summer than it was in winter (Fig. 4.20c). In autumn the region of decrease lay between 33 °N 134 °E and 34 °N 146.5 °E, similarly to other seasons, and the dipole structure evident in spring had almost completely disappeared (Fig. 4.20d).

A comparison of vertical wind strength differences between the LM and SP phases along the line 30 °N–35 °N, 140 °E (line A–B in Fig. 4.18a) showed that the greatest changes were observed in winter (Fig. 4.21a). These changes, which were greater than 2.4 hPa h^{-1}, were observed at the 900–850 hPa level, at 32 °N and 33.2 °N. During the SP phase, upward winds were dominant at 32 °N–34 °N, but were weaker than during the LM phase. During spring and summer, the two winter peaks merged and shifted northward, towards the land (Figs. 4.21b and 4.21c). In autumn, the peak moved southward again (Fig. 4.21d). In summer, the strengthening of downward winds occurred at higher elevations, up to and above the 400 hPa level.

4.4.4 The influence of the Kuroshio LM on the Japanese climate

As discussed above, differences between the predictions of the OGCM-run and the JRA-run were most striking around the cold pool area and the Pacific Ocean side of central Japan, but were hardly apparent in other regions of Japan (Figs. 4.18, 4.19 and 4.20). To obtain a quantitative estimate of the influence of changes in the Kuroshio's path on Japan's climate, we focused on three land areas along the Pacific side of Japan (Fig. 4.22) and compared the averages of four climate parameters with those from the cold pool area. We examined the deviation of the predictions of the OGCM-run from those of the JRA-run. For this analysis, area A was defined as the region where the Kuroshio turns southward during LM phases, area B as the region where the Kuroshio's path is the furthest from land, and area C as the region near the open ocean where the Kuroshio turns north-eastward in both the LM and SP phases. Model run duration was divided into 4 seasons and results were compared between seasons.

With respect to monthly variation in area-averaged SAT, according to the definition (4-4), area A showed a statistically significant ($p < 0.1$, all seasons) reduction in SAT of approximately 0.1 °C–0.2 °C (Fig. 4.23a), which is 20 %–30 % of the reduction over the oceanic cold pool area. There was also a small but significant ($p < 0.1$) reduction of approximately 0.1 °C in February, May, and July in area B and in March in area C. The result indicates that for SAT, area A located nearest the cold pool is more influenced by the cold SST pool than the other areas.

For seasonal weather forecasting of temperature, the definition of the range of a normal year varies slightly according to the area and seasons but is approximately ± 0.2 °C of the average climate. Therefore, in the land region near the cold SST pool, Kuroshio LM may become an important factor for seasonal weather forecasting.

Figures 4.23b and 4.23c indicate the change ratio of precipitation and of precipitation frequency, respectively. In the ocean area, the precipitation change rate shows a 10 %–40 % decrease in most months. In particular, the change ratios in July and August are remarkable while in area C, precipitation tends to decrease except in November. The precipitation change ratio in June (−12 %) is larger than that of the ocean area (−5 %) and is comparable in March and May (Fig. 4.23b). For seasonal weather forecasting of precipitation, the definition of the range of the normal year ratio is around 75 %–125 % of the normal year. Therefore, our result indicates that the precipitation change due to the Kuroshio LM cannot be ignored for weather forecasting.

The result also shows that a large positive precipitation change ratio appeared in November (Fig. 4.23b), while the precipitation frequency change ratio was not statistically significant (Fig. 4.23c). As to the large negative precipitation change ratio in December, we found some cases with large discrepancies between the OGCM-run and JRA-run (not shown here). It may be due to the slight shift in the path of the disturbances, and we confirmed that the result of the OGCM-run was closer to the observation (AMeDAS). Furthermore, simple calculation without using the definition of equation (4-4) showed that the OGCM precipitation difference ratio, (LM-SP)/SP, was approximately −5 %, which was close to that in the other winter months. Further investigation may be required in the future.

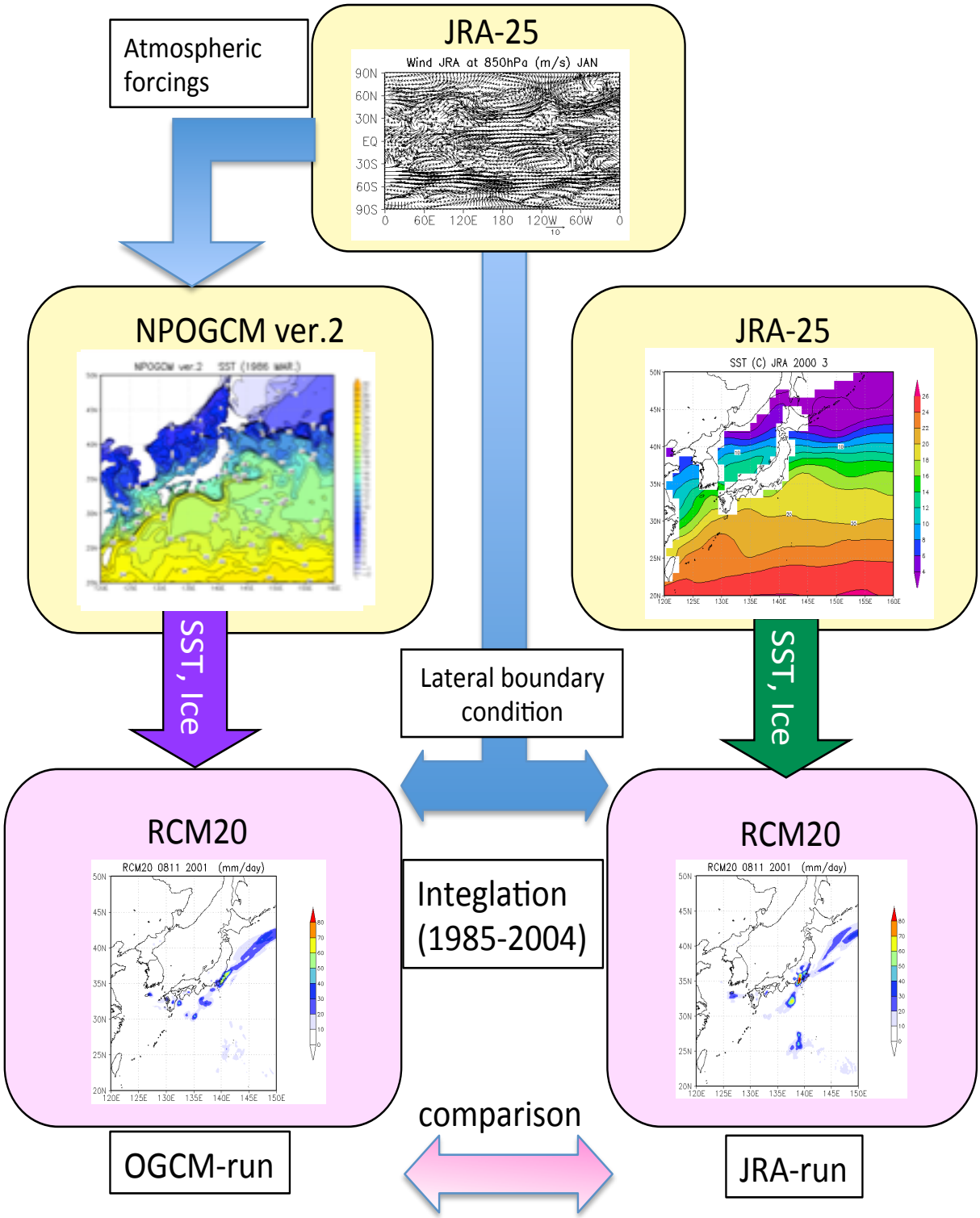

Fig. 4.1 Experimental design.

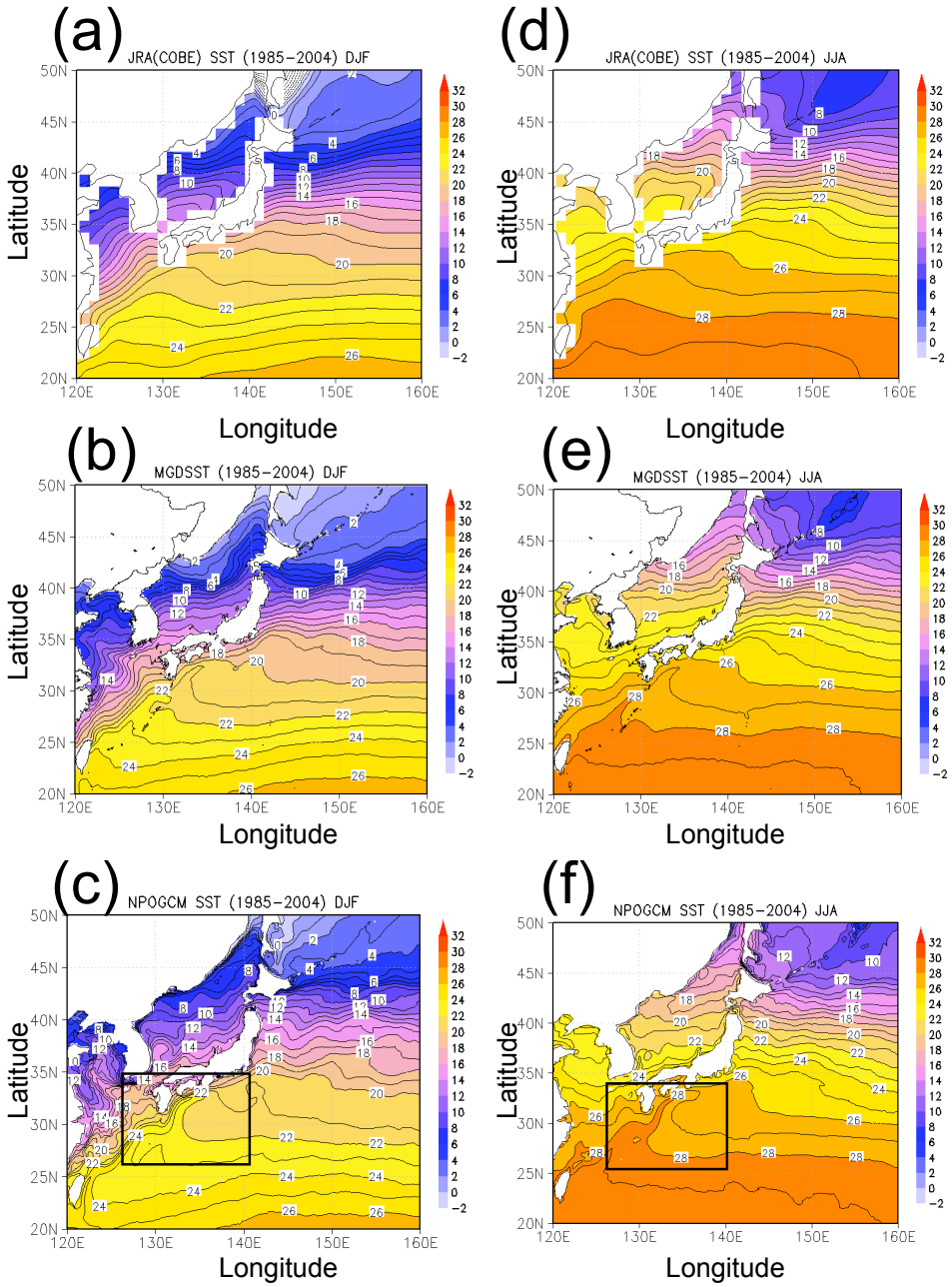

Fig. 4.2 Horizontal distributions of 20-year-averaged SST from the JRA-25 (a, d), from the MGDSST (b, e), and simulated by NPOGCM (c, f). Distributions are for winter (December–February; a, b, c) and summer (June–August; d, e, f). The isotherm interval is 1 °C. Rectangles in (c) and (f) indicate the area where warm northward SST flows occur, which are associated with the Kuroshio.

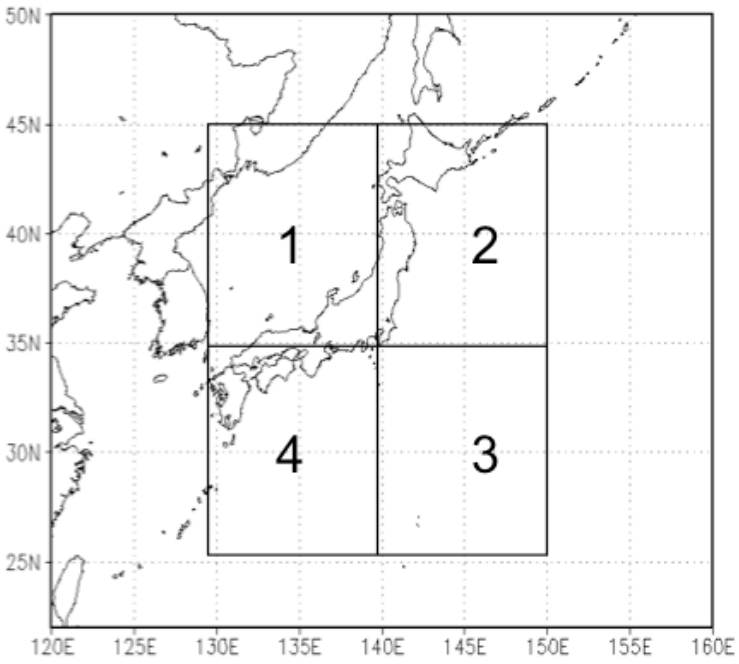

Fig. 4.3 Division of zones for the evaluation of 20-year SST averages used in Fig. 4.4 (zone 1: 35 °N–45 °N, 130 °E–140 °E; zone 2: 35 °N–45 °N, 140 °E–150 °E; zone 3: 25 °N–35 °N, 140 °E–150 °E; zone 4: 25 °N–35 °N, 130 °E–140 °E).

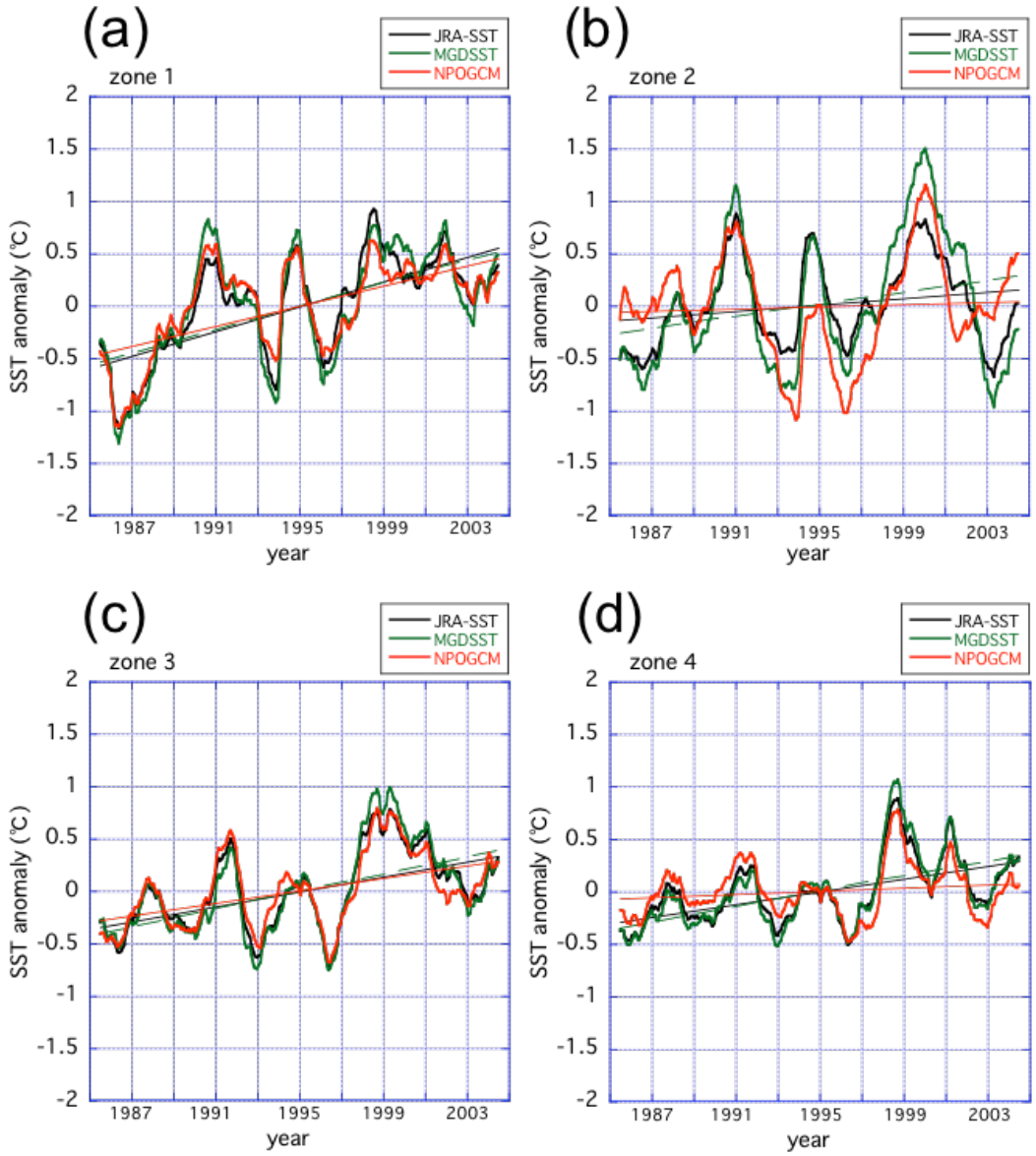

Fig. 4.4 Time series averages over each of the four zones with a trend line for the 12-month running mean SST anomaly in (a) zone 1, (b) zone 2, (c) zone 3, and (d) zone 4. Red lines: NPOGCM results. Green lines: MGDSST. Black lines: SST of JRA-25.

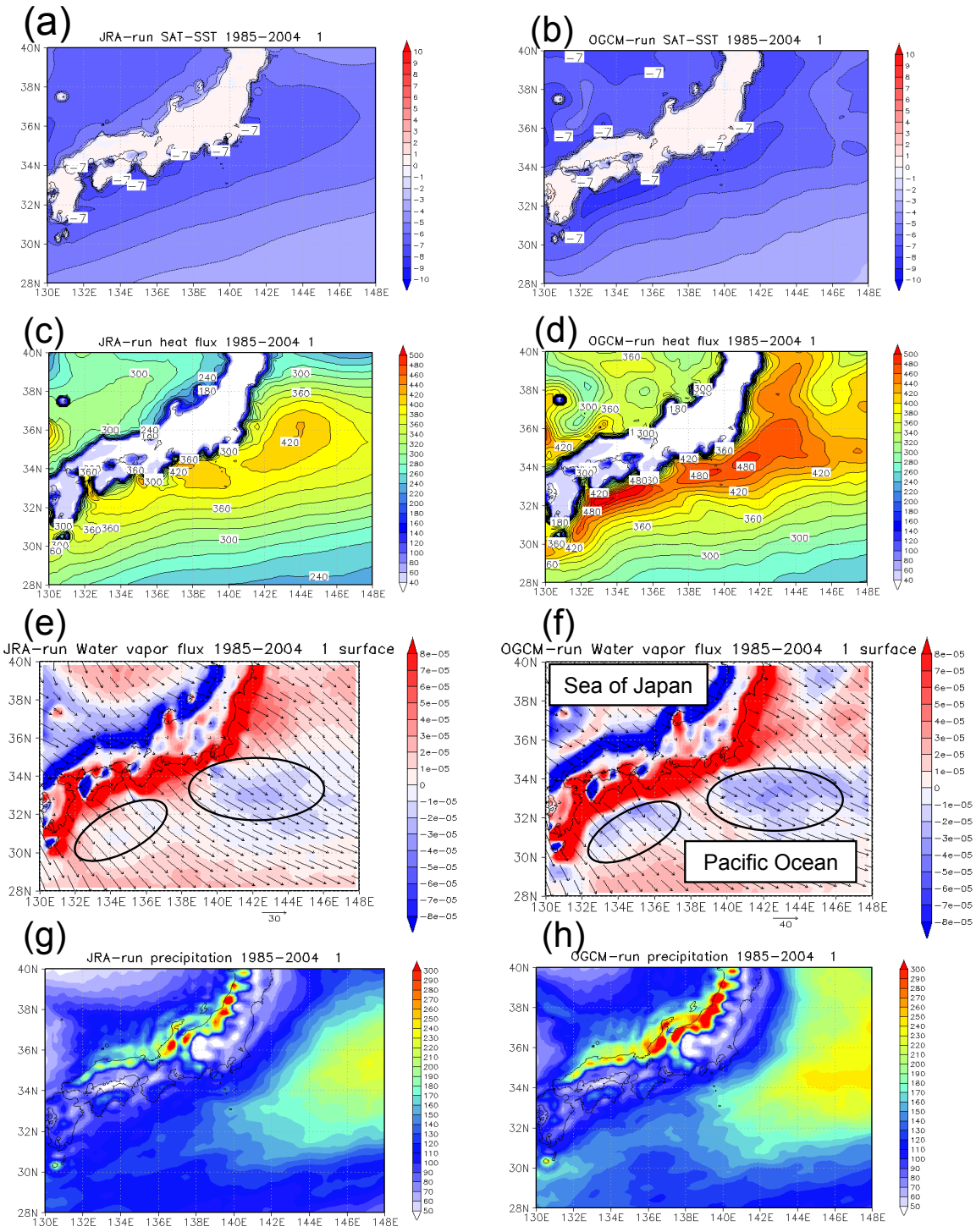

Fig. 4.5 Twenty-year-averaged data for January. SAT–SST [°C] of (a) JRA-run and (b) OGCM-run. Heat flux [W m^{-2}] of (c) JRA-run and (d) OGCM-run. Water vapor flux and its divergence [s^{-1}] of (e) JRA-run and (f) OGCM-run. Precipitation [mm $month^{-1}$] of (g) the JRA-run and (h) OGCM-run.

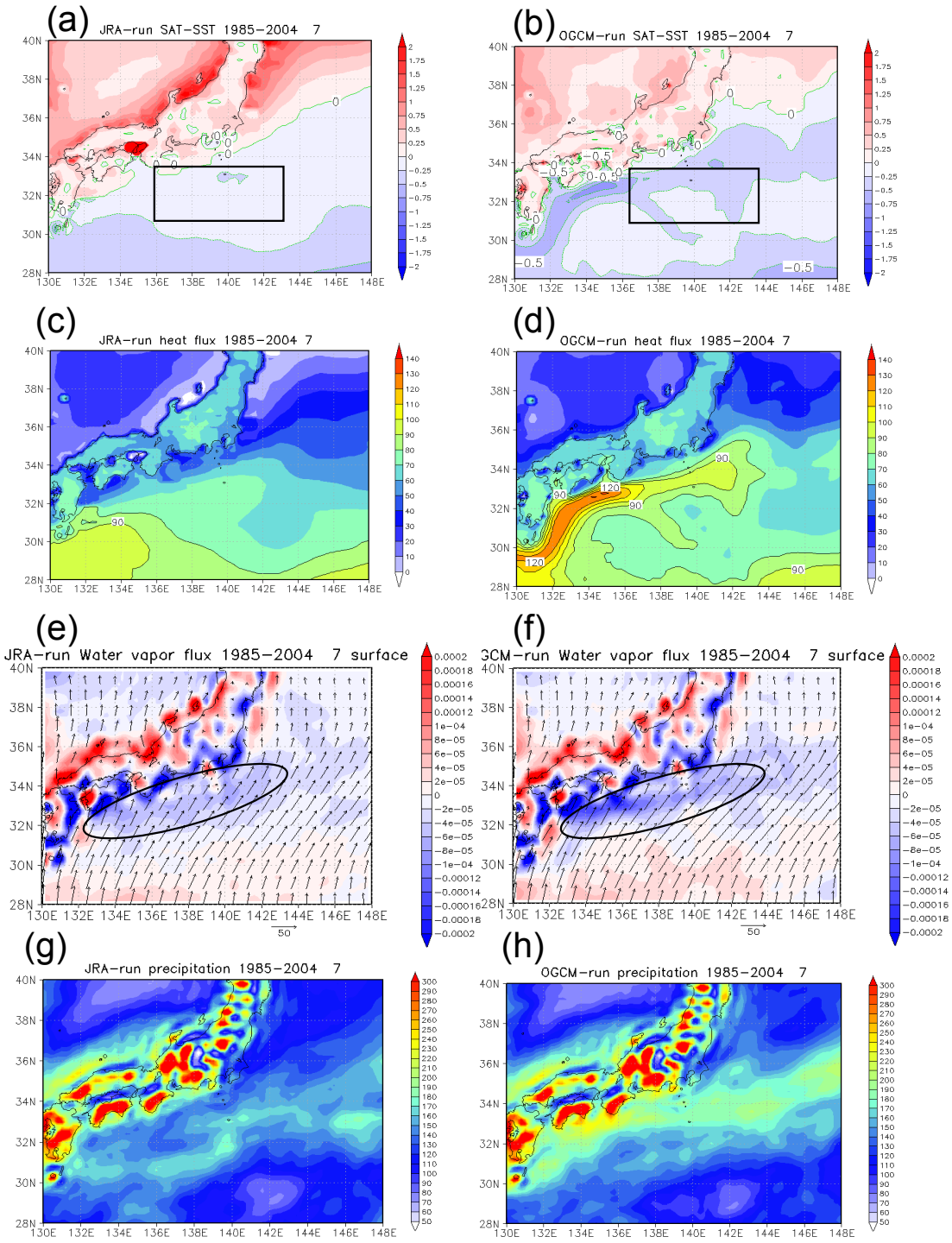

Fig. 4.6 Twenty-year-averaged data for July. SAT–SST [°C] of (a) JRA-run and (b) OGCM-run. Heat flux [W m^{-2}] of (c) JRA-run and (d) OGCM-run. Water vapor flux and its divergence [s^{-1}] of (e) JRA-run and (f) OGCM-run. Precipitation [mm $month^{-1}$] of (g) the JRA-run and (h) OGCM-run. The rectangles in Figs. 4.6a,b show the area used for the data in Table. 4.1.

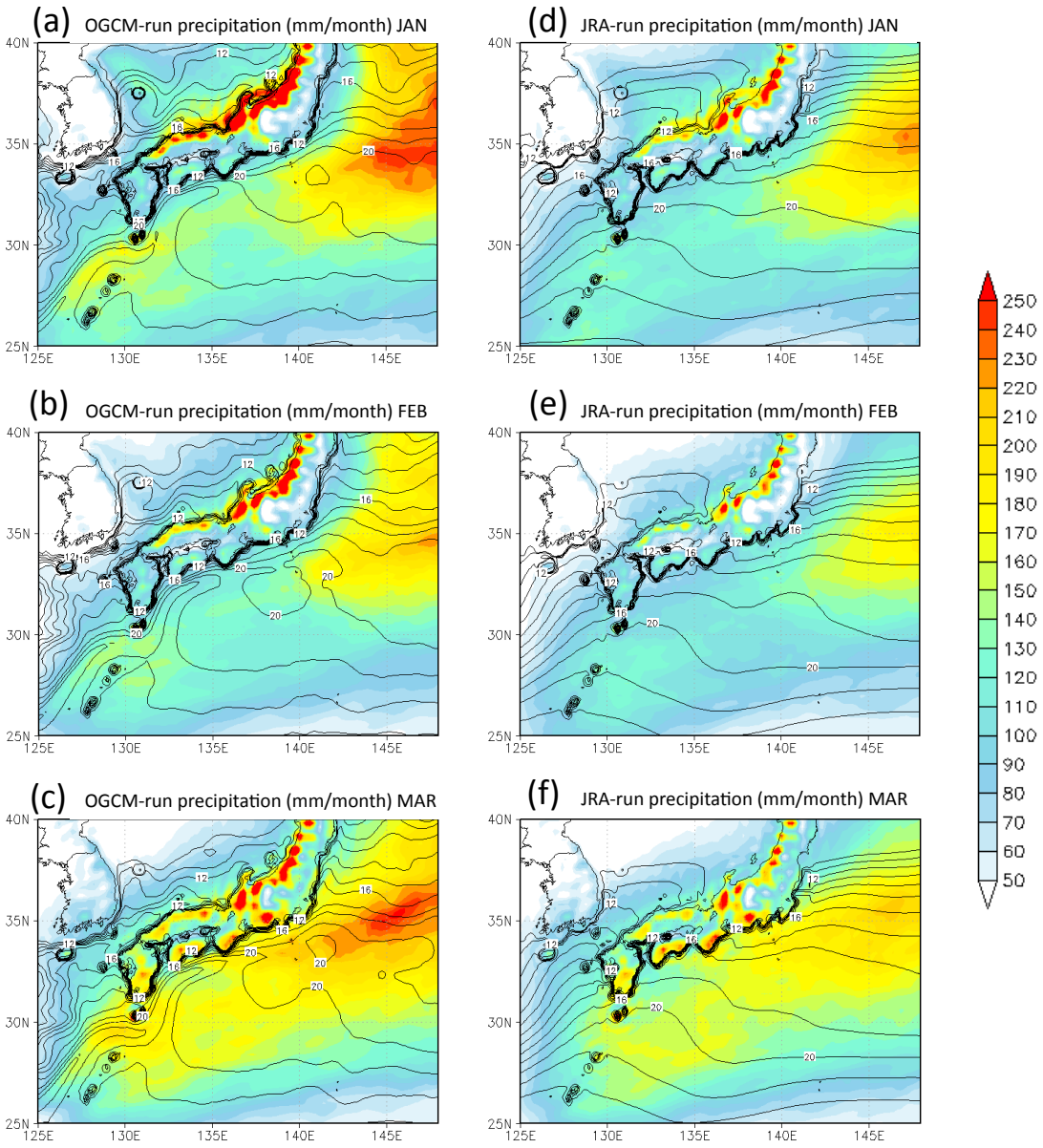

Fig.4.7 Twenty-year-averaged monthly precipitation (mm month^{-1}) of the GCM-run (left side) and the JRA-run (right side). Distributions are for January (a, d), February (b, e) and March (c, f). The contour denotes SST and the 1st layer of ground temperature in the land. The isotherm interval is 1 °C, and the range is from 12 °C to 29 °C.

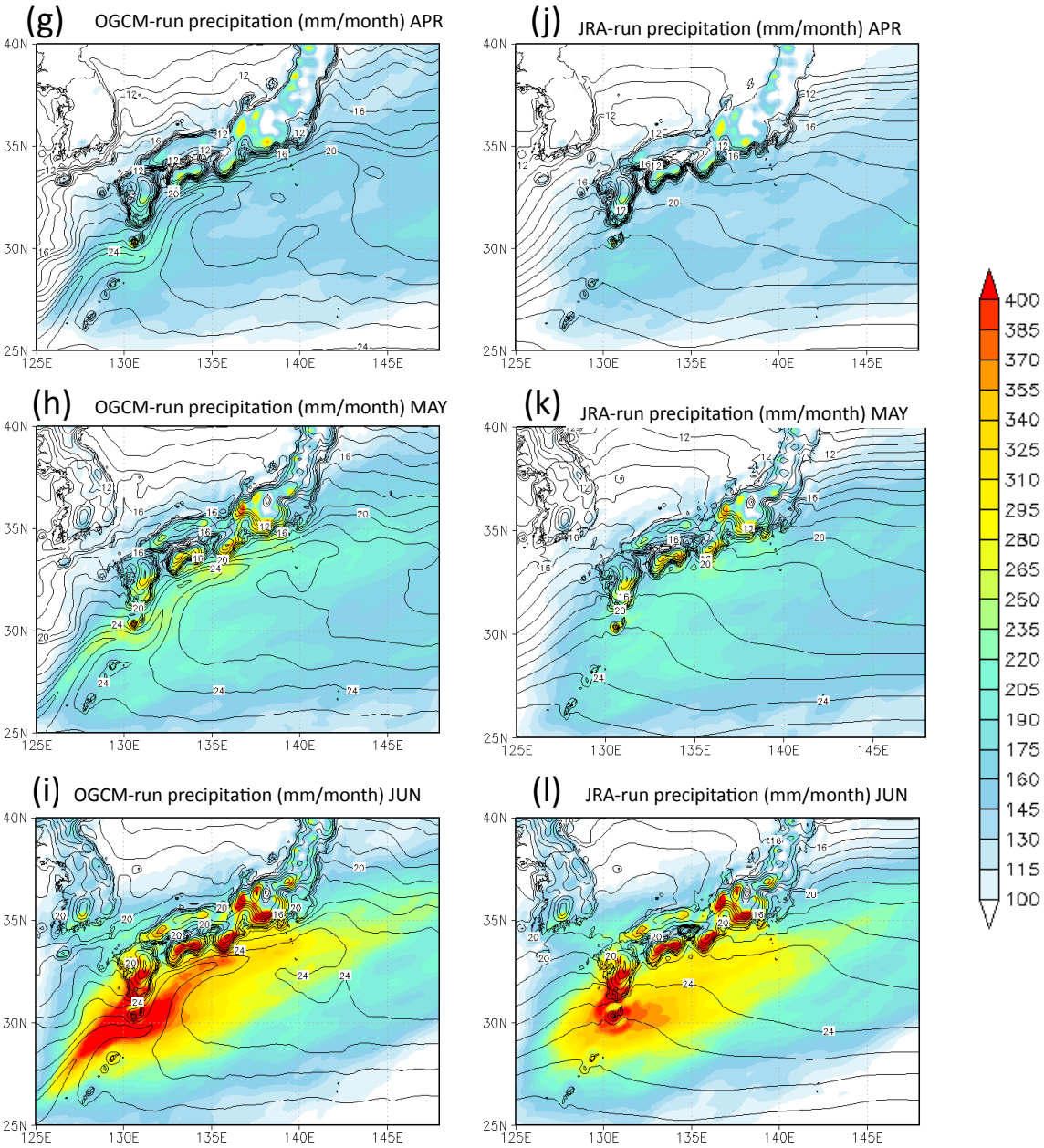

Fig.4.7 Continued. Twenty-year-averaged monthly precipitation (mm month^{-1}) of the GCM-run (left side) and the JRA-run (right side). Distributions are for April (g, j), May (h, k) and June (i, l). The contour denotes SST and the 1st layer of ground temperature in the land. The isotherm interval is 1 °C, and the range is from 12 °C to 29 °C.

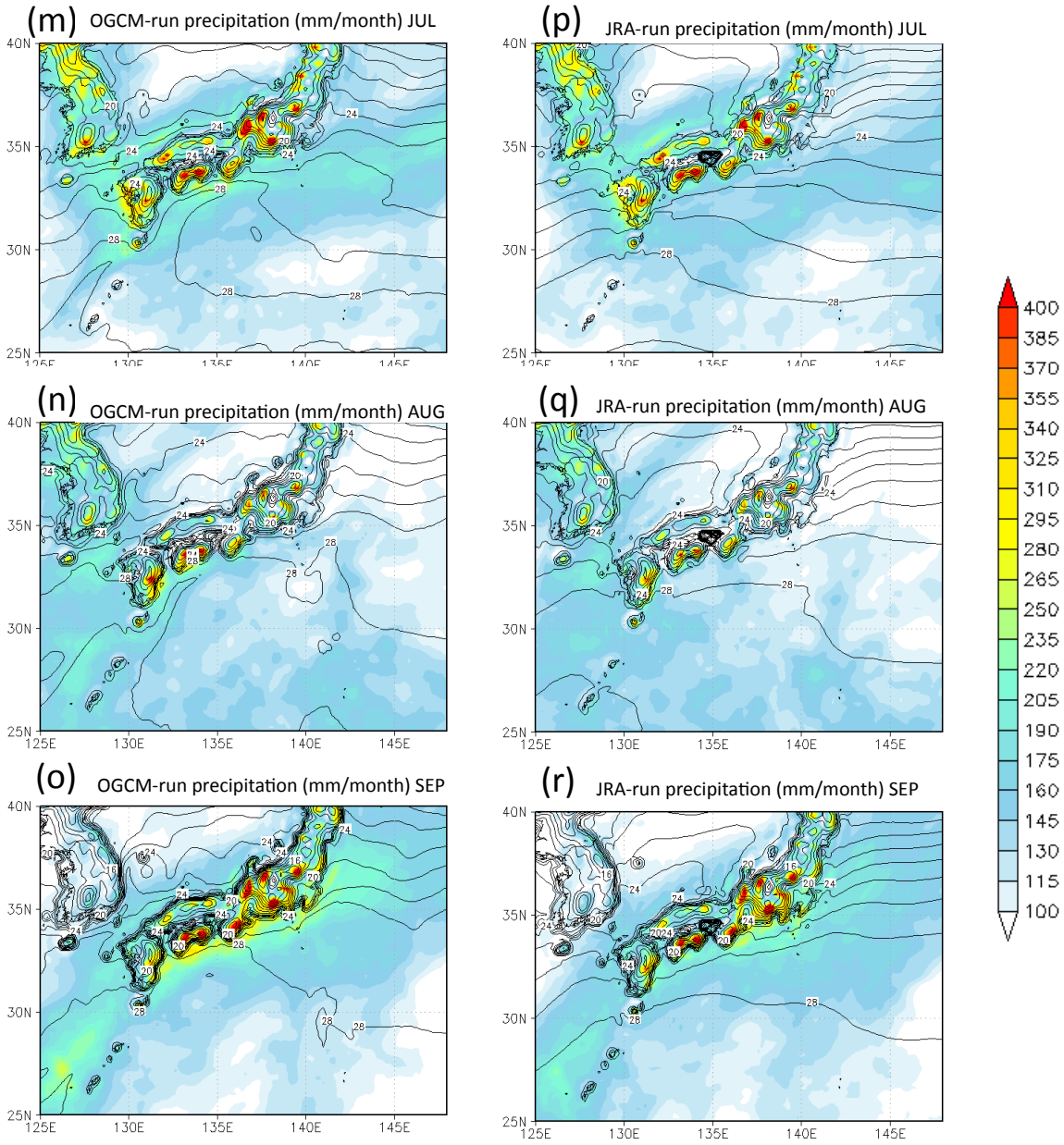

Fig.4.7 Continued. Twenty-year-averaged monthly precipitation (mm month^{-1}) of the GCM-run (left side) and the JRA-run (right side). Distributions are for July (m, p), August (n, q) and September (o, r). The contour denotes SST and the 1st layer of ground temperature in the land. The isotherm interval is 1 °C, and the range is from 12 °C to 29 °C.

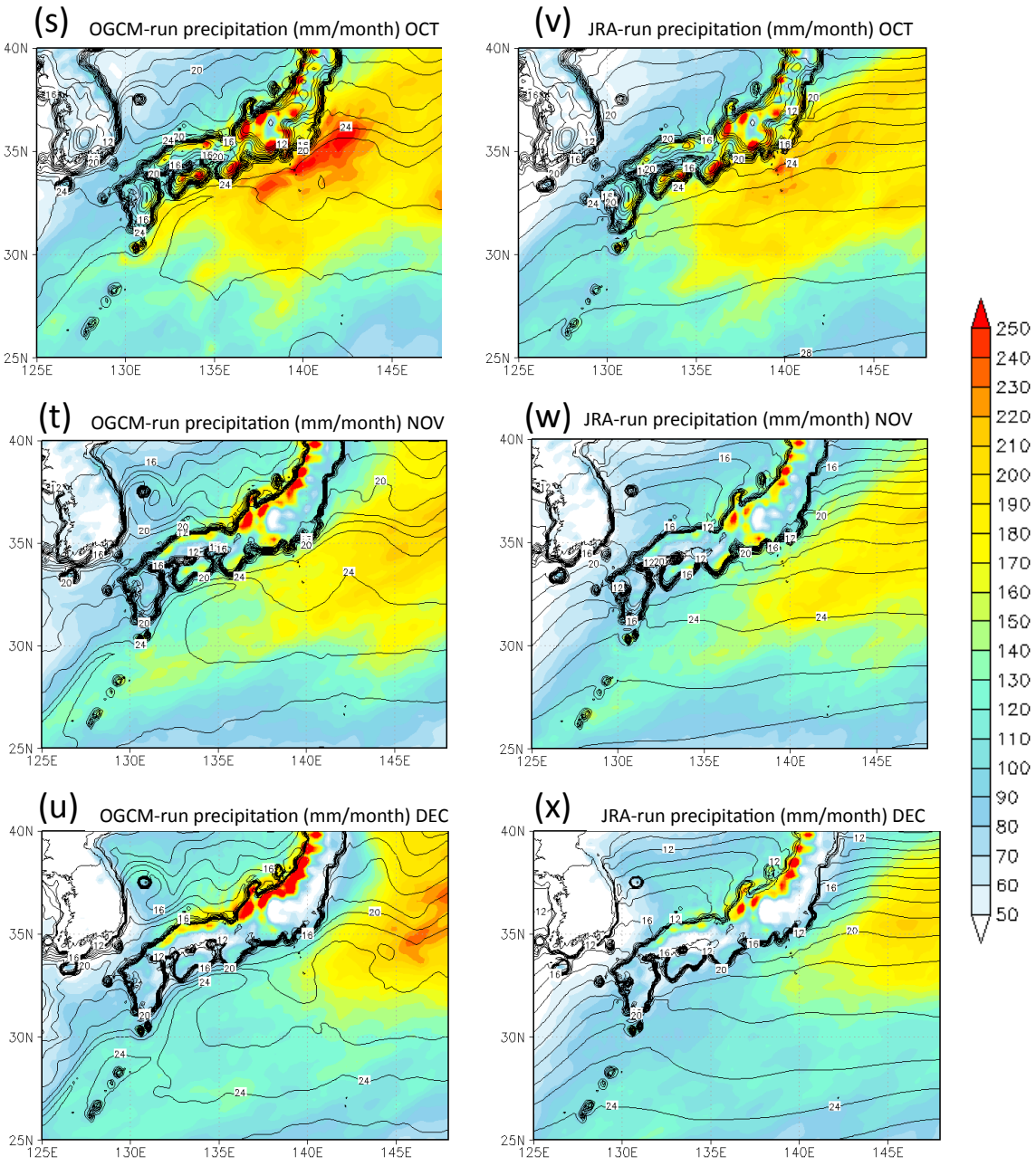

Fig.4.7 Continued. Twenty-year-averaged monthly precipitation (mm month^{-1}) of the GCM-run (left side) and the JRA-run (right side). Distributions are for October (s, v), November (t, w) and December (u, x). The contour denotes SST and the 1st layer of ground temperature in the land. The isotherm interval is 1 °C, and the range is from 12 °C to 29 °C.

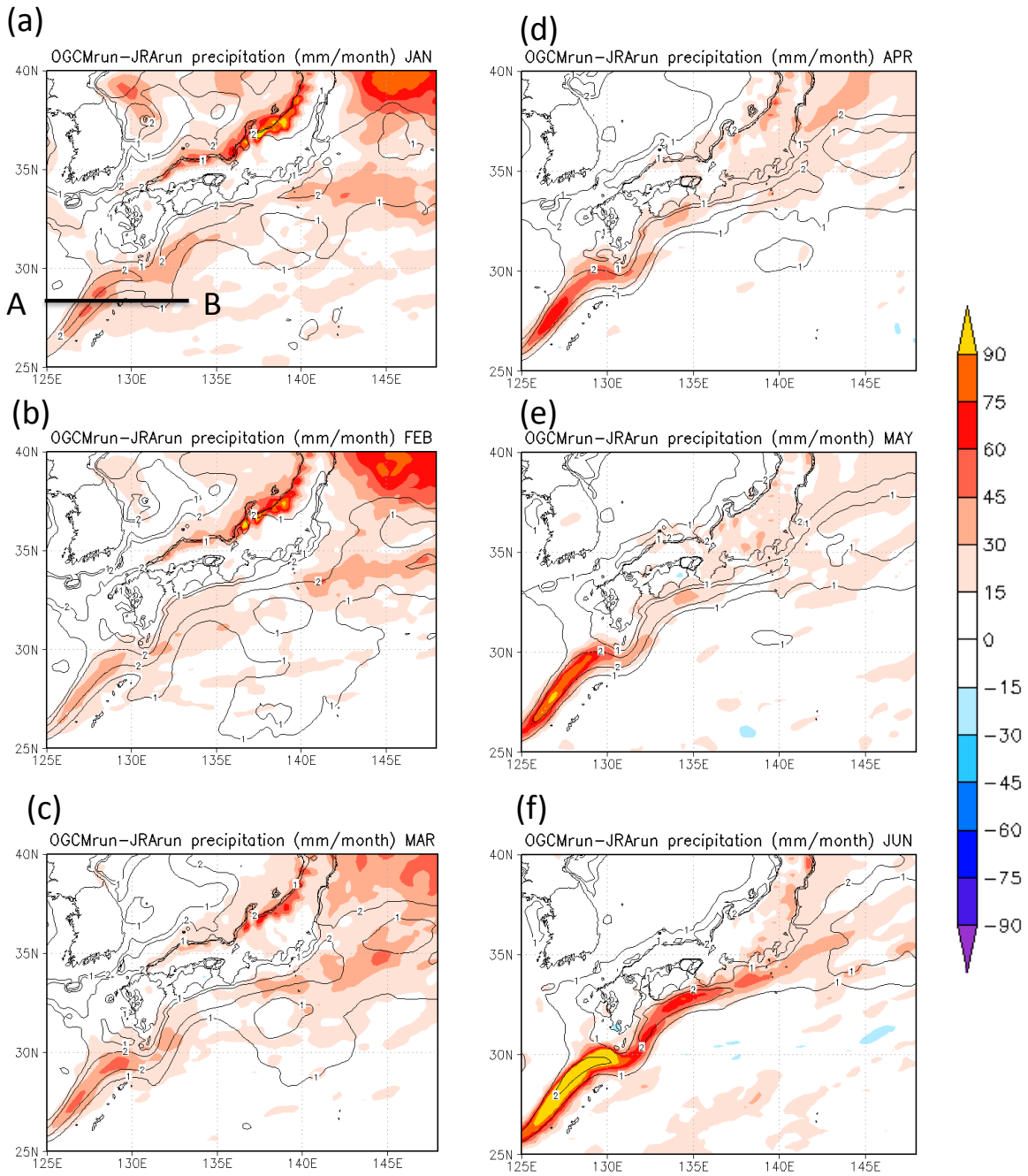

Fig. 4.8 Monthly precipitation differences between OGCM-run and JRA-run in (a) January, (b) February, (c) March, (d) April, (e) May and (f) June. The unit is mm day^{-1}. The contour denotes SST difference is 2 °C. The line from A to B in Fig. 4.8 (a) indicates the cross section illustrated in Fig. 4.9.

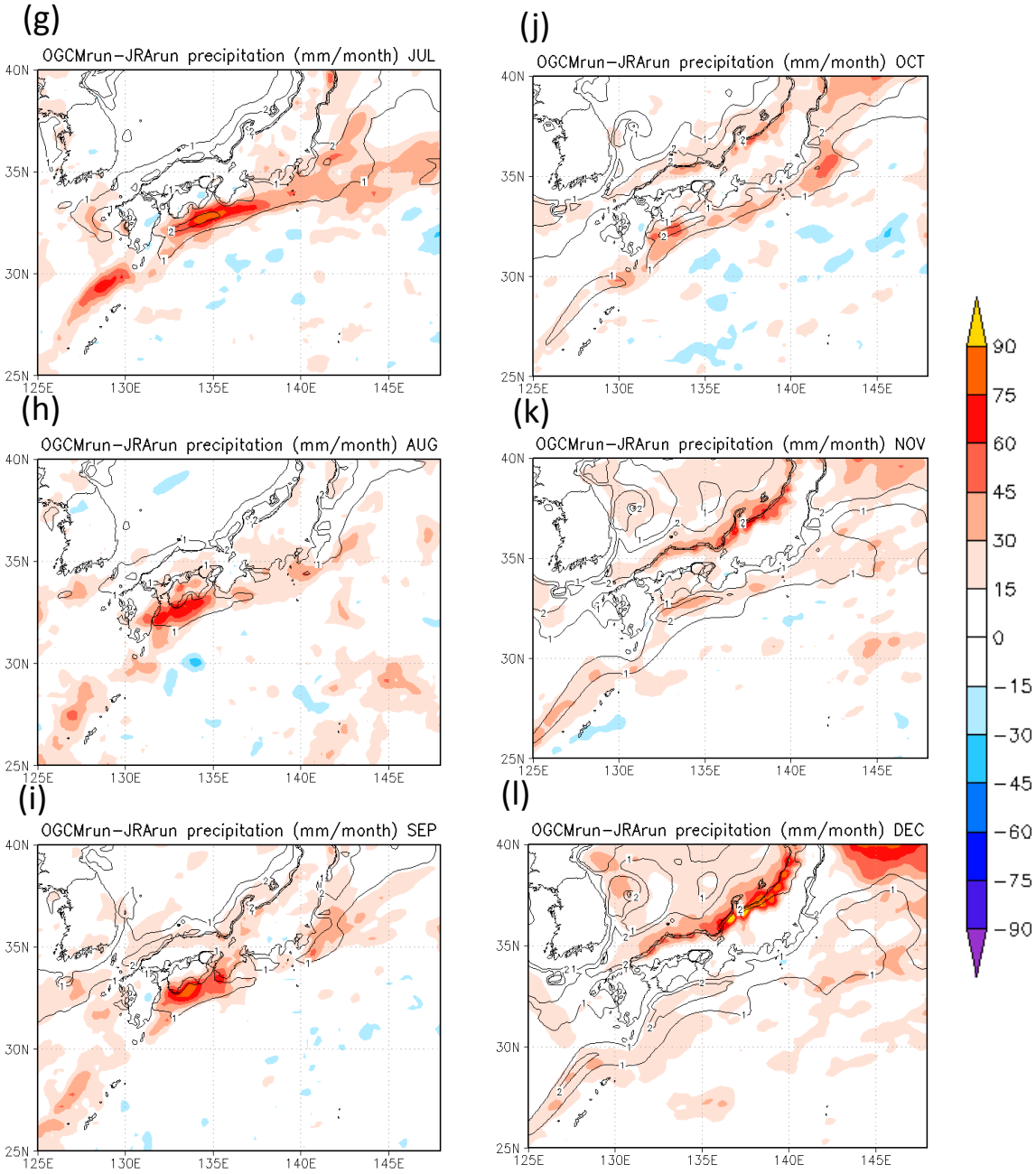

Fig. 4.8 Continued. (g) July, (h) August, (i) September, (j) October, (k) November and (l) December. The unit is mm day^{-1}.

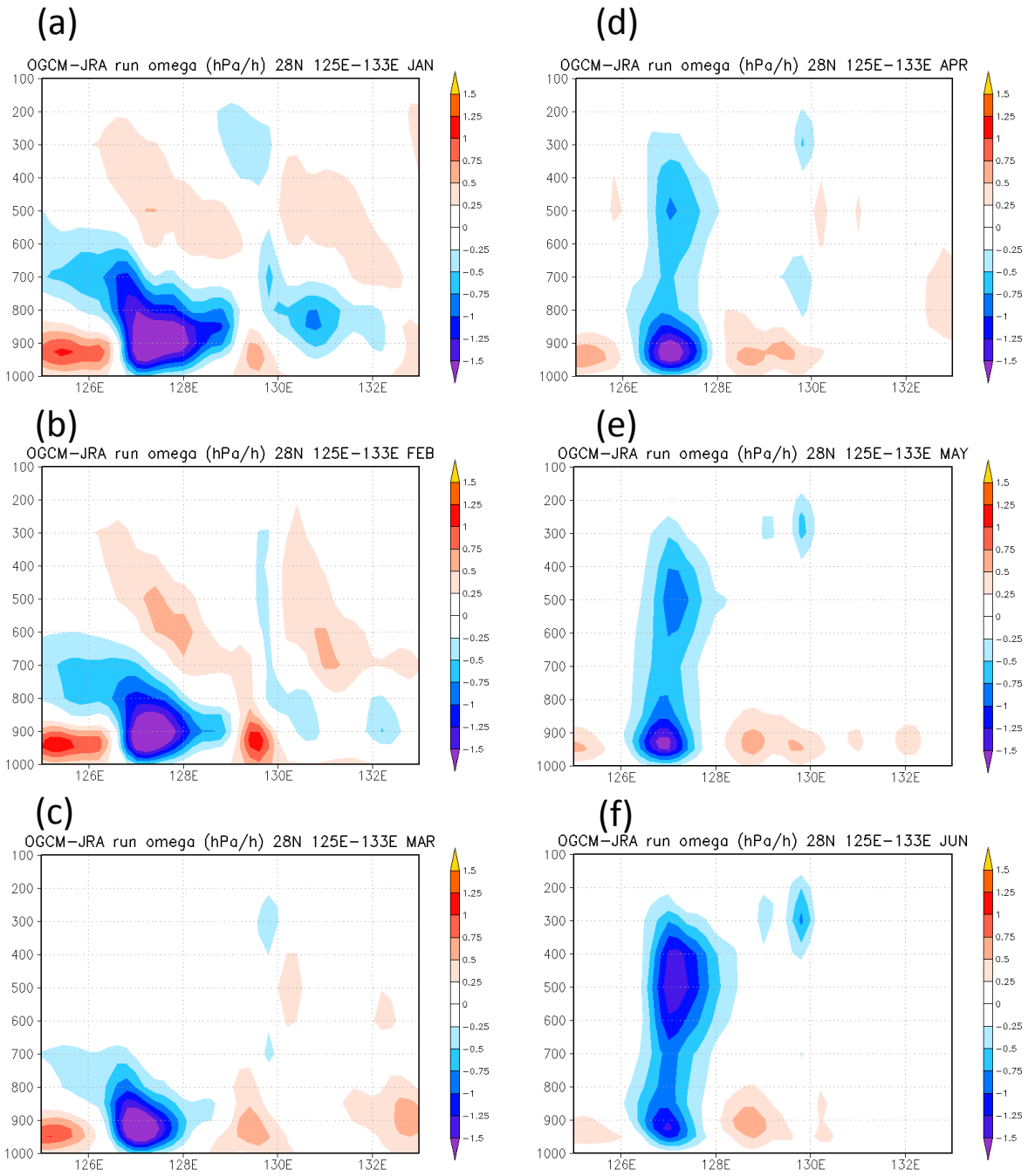

Fig. 4.9 Vertical cross section of vertical wind difference between OGCM-run and JRA-run in (a) January, (b) February, (c) March, (d) April, (e) May and (f) June, along the line A-B in Fig. 4.8 (a). Negative value indicates upward direction. The unit is hPa hour^{-1}

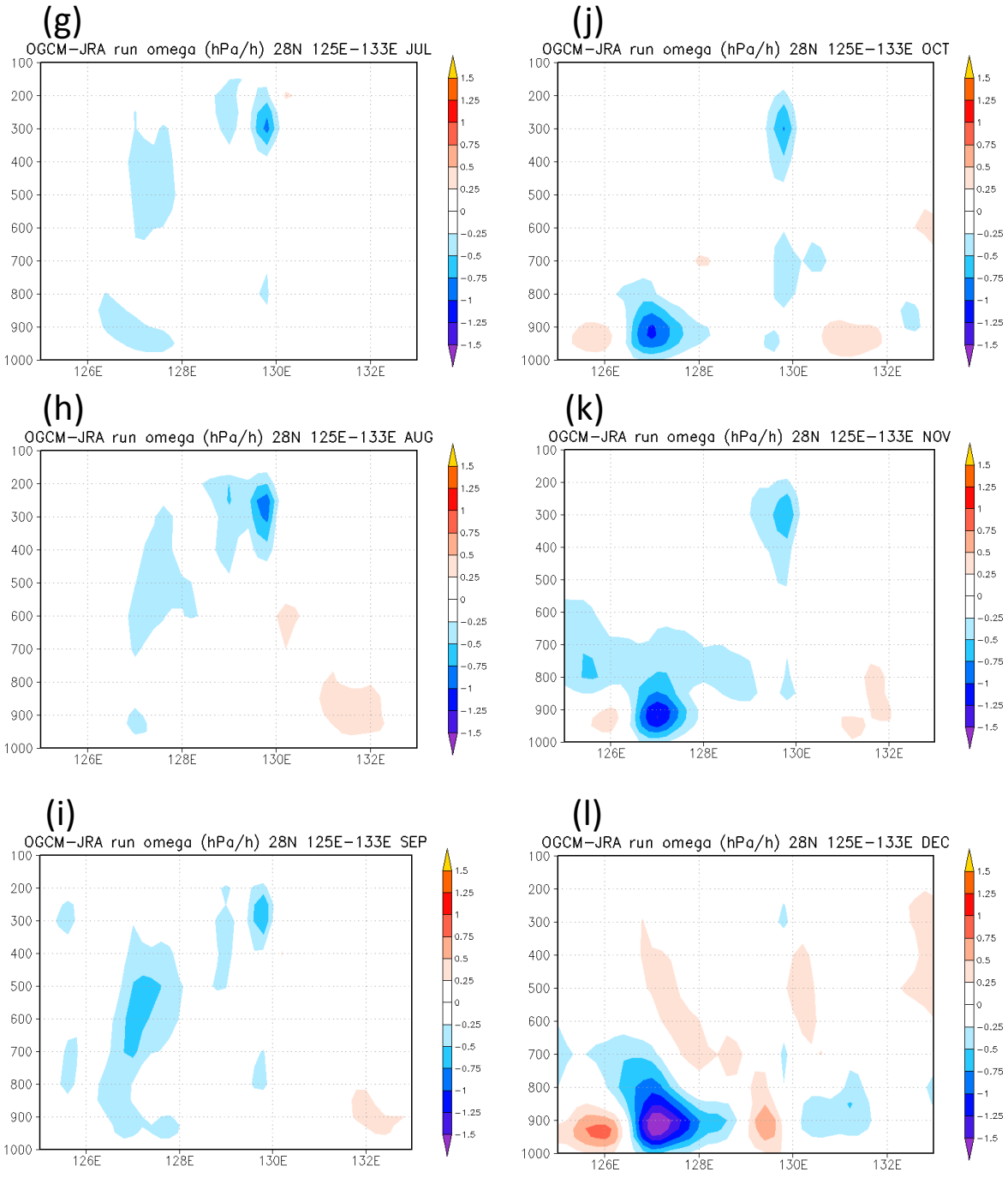

Fig. 4.9 Continued. (g) July, (h) August, (i) September, (j) October, (k) November and (l) December.

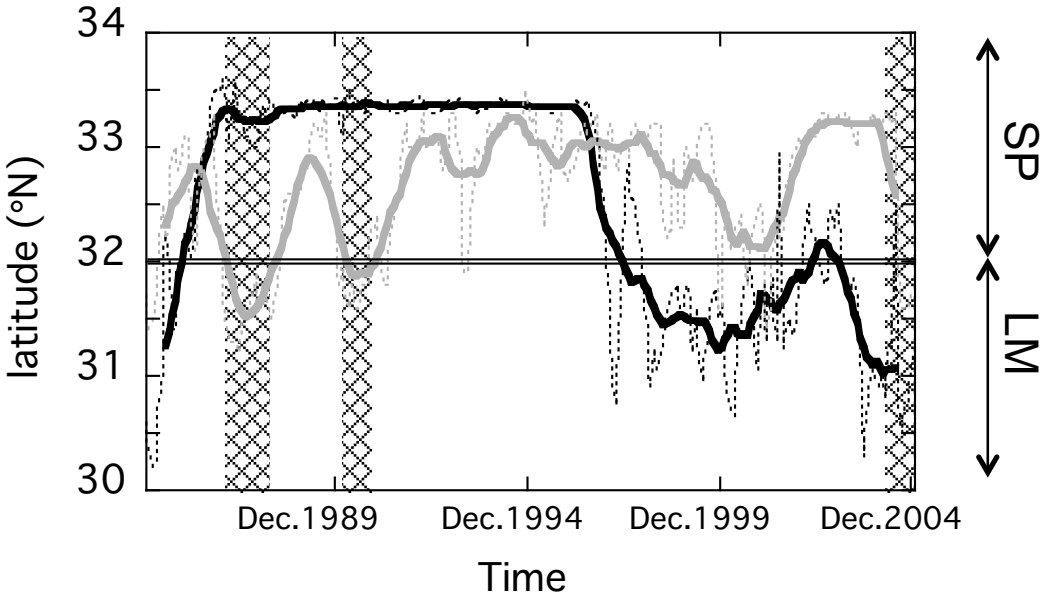

Fig. 4.10 Time series of the southernmost latitude with a water temperature of 15 °C at a depth of 200 m within the latitude range 136–139 °E. The dotted line indicates monthly values, and the solid line indicates the 13-month running mean. The gray line denotes the value observed by the Japan Meteorological Agency, and the black line denotes the simulation produced by NPOGCM. SP denotes the straight path state and LM denotes the large meander state. Cross-hatched sections indicate when the Kuroshio was actually in the LM state.

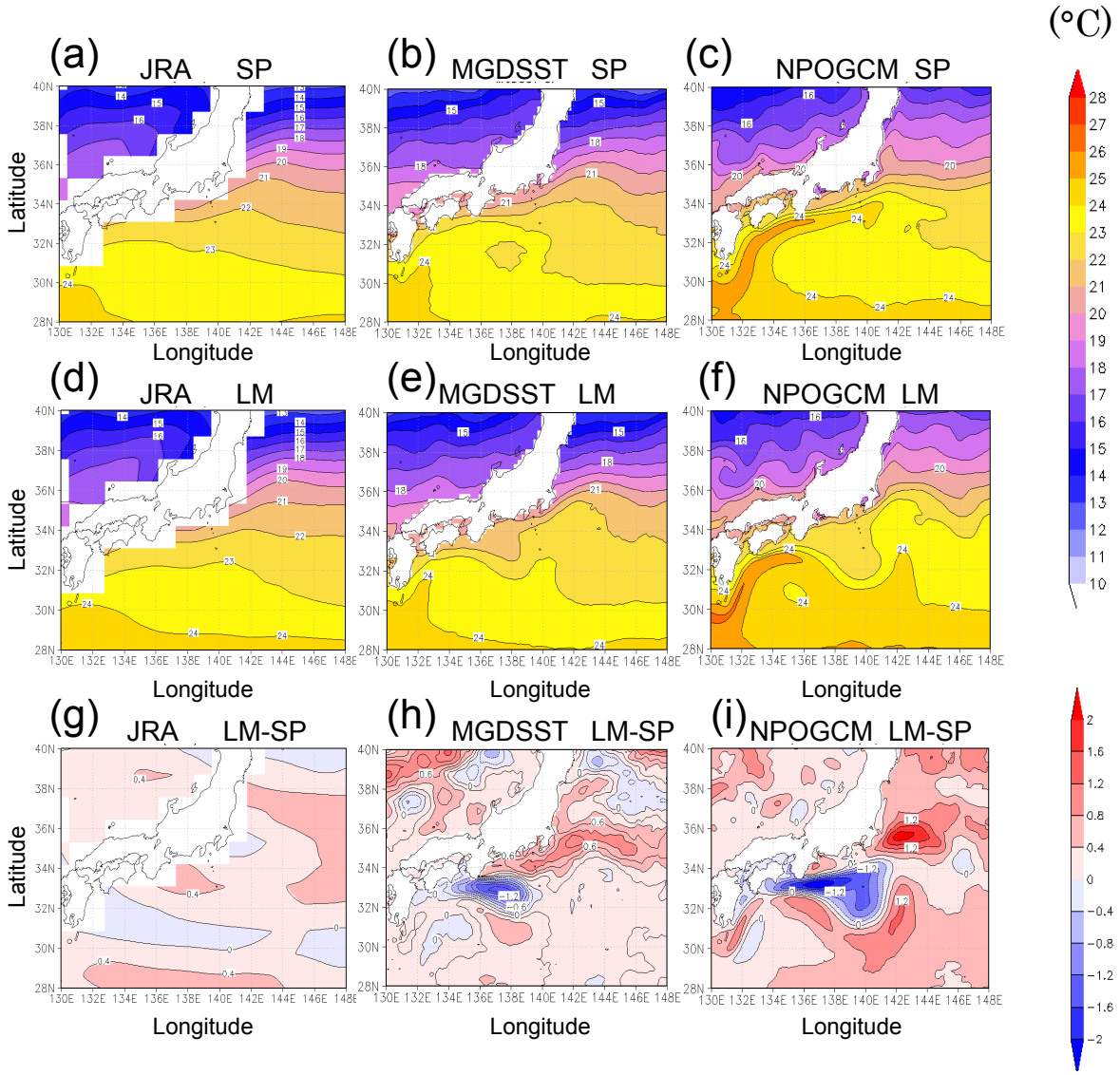

Fig. 4.11 Averaged SST from the JRA-25 (a, d), from the MGDSST (b, e) and predicted by NPOGCM (c, f). Values are averaged for the periods when the Kuroshio was in the SP state (a, b, c) and in the LM state (d, e, f). The contour interval is 1 °C. The figures in the bottom row show differences in SST between the SP state and the LM state, based on JRA-25 data (g), MGDSST data (h) and NPOGCM predictions (i). The contour interval is 0.4 °C. The periods used for the Kuroshio LM state for the JRA-SST and MGDSST data are January 1987 to June 1988, January–December 1990 and July–December 2004. The period used for the SP state is January 1995 to December 1997. For the NPOGCM predictions, the SP period used is January 1988 to December 1996, and the LM period is January 1997 to December 2004.

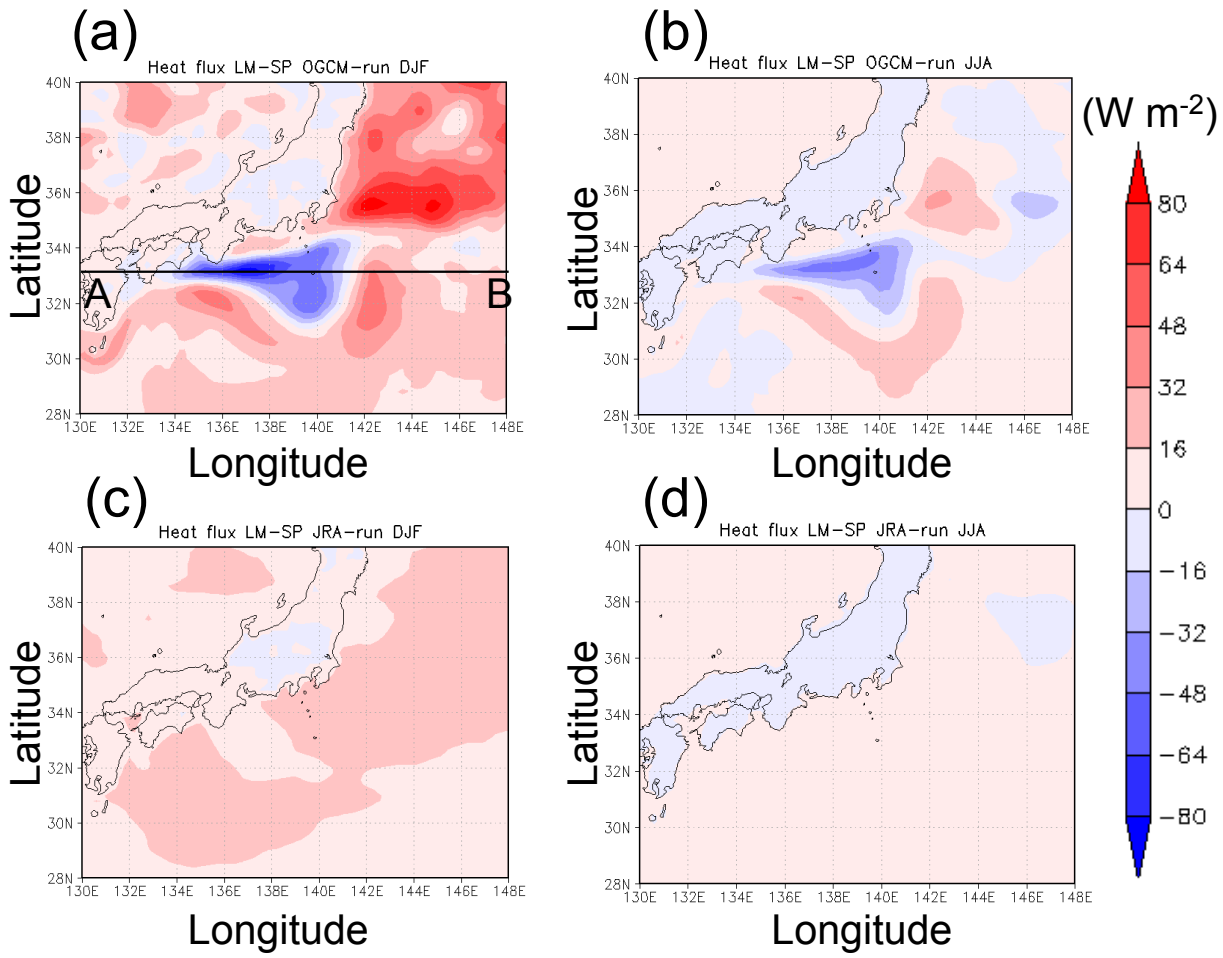

Fig. 4.12 Differences in seasonal averaged total surface turbulent heat flux (W m^{-2}) between the Kuroshio LM and SP states (LM minus SP), as simulated by the OGCM-run in (a) winter (December–February) and (b) summer (June–August), and by the JRA-run in (c) winter and (d) summer. The line from A to B in Fig. 4.12a indicates the cross-section illustrated in Figs. 4.15 and 17.

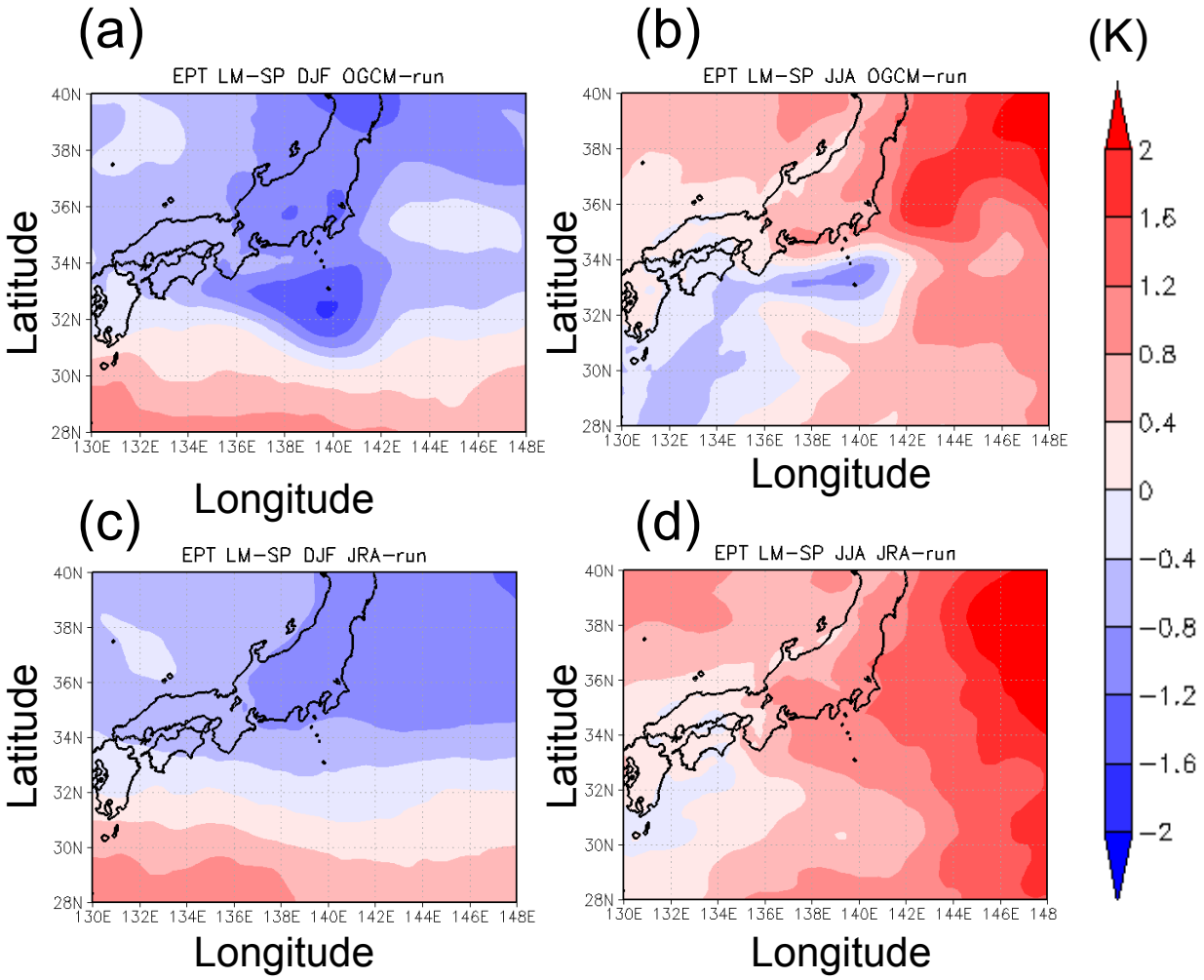

Fig. 4.13 Differences in seasonal averaged EPT (K) between the Kuroshio LM and SP states (LM minus SP), as simulated by the OGCM-run in (a) winter (December–February) and (b) summer (June–August), and by the JRA-run in (c) winter and (d) summer.

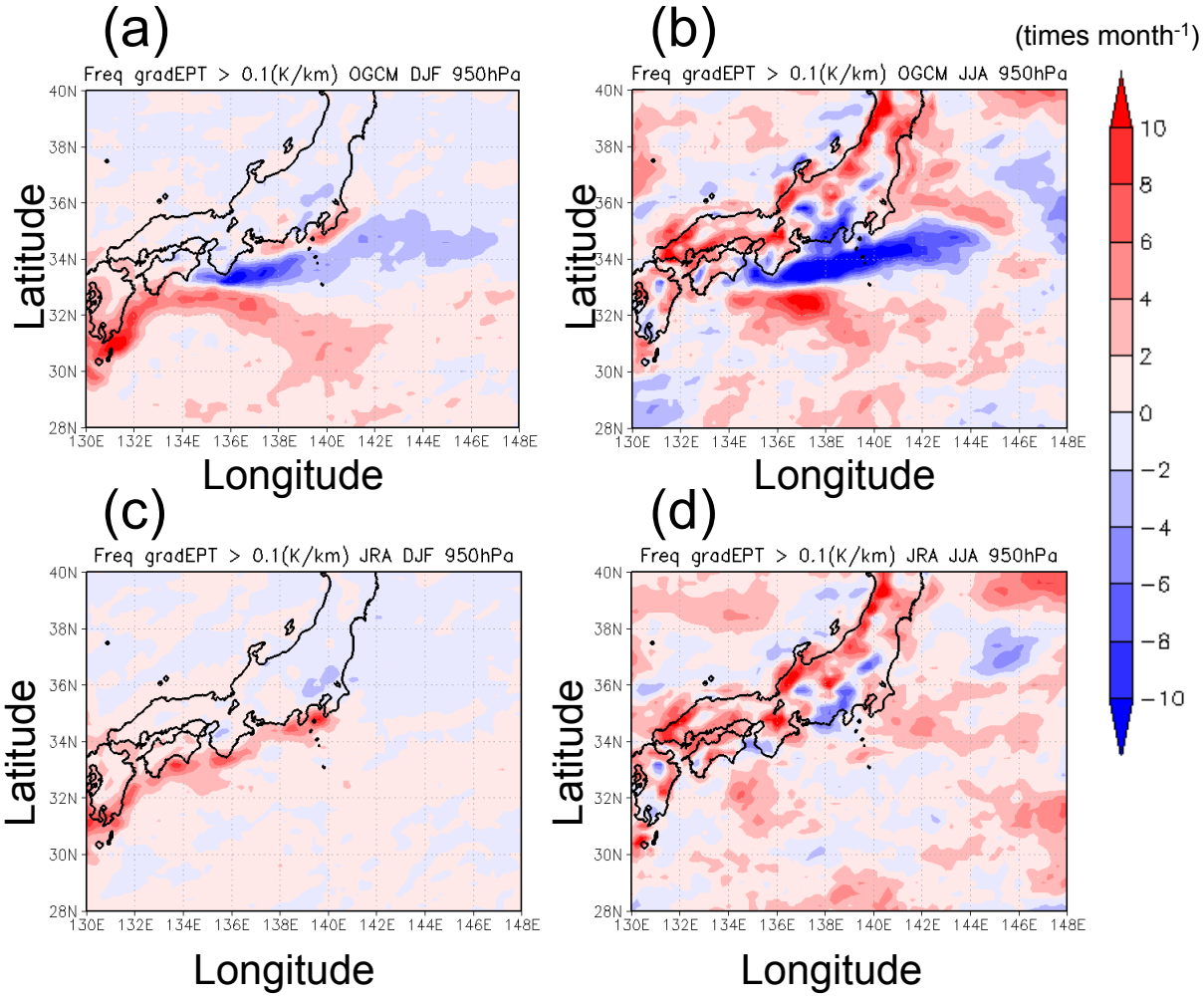

Fig. 4.14 Differences in seasonal averaged frequency of horizontal EPT gradients ($|\nabla_h \theta_e|$) that exceed 0.1 K km^{-1} (times month^{-1}) between the Kuroshio LM and SP states (LM minus SP), as simulated by the OGCM-run in (a) winter (December–February) and (b) summer (June–August), and by the JRA-run in (c) winter and (d) summer.

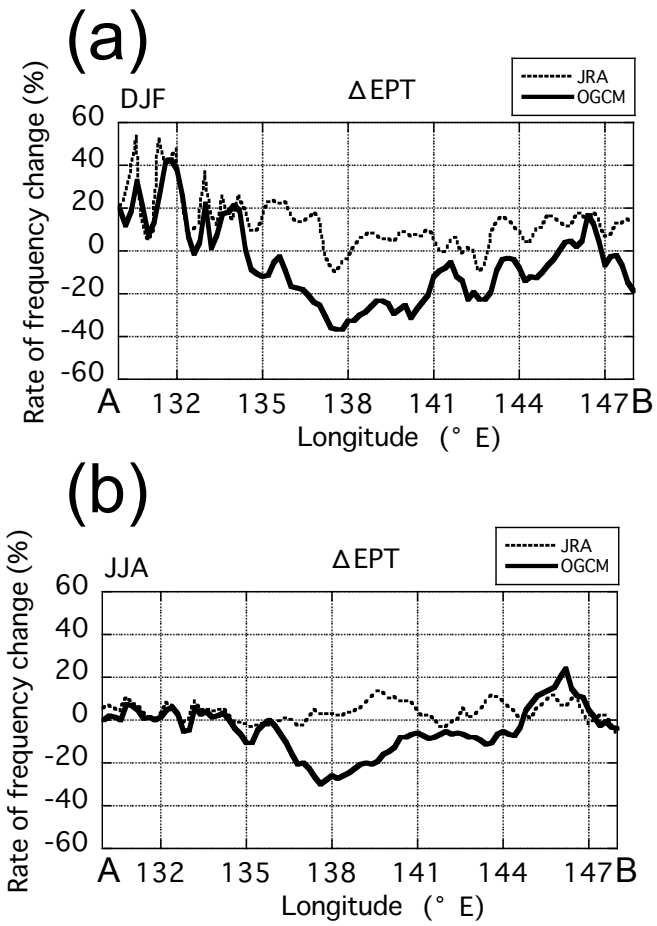

Fig. 4.15 Rate of change, calculated as (LM–SP)/SP and expressed as a percentage, in the frequency of horizontal EPT gradients ($|\nabla_h \theta_e|$) that exceed 0.1 K km^{-1} in (a) winter and (b) summer, as simulated by the JRA-run (dashed line) and the OGCM run (bold solid line), along 33.6°N (line A–B in Fig. 4.12a).

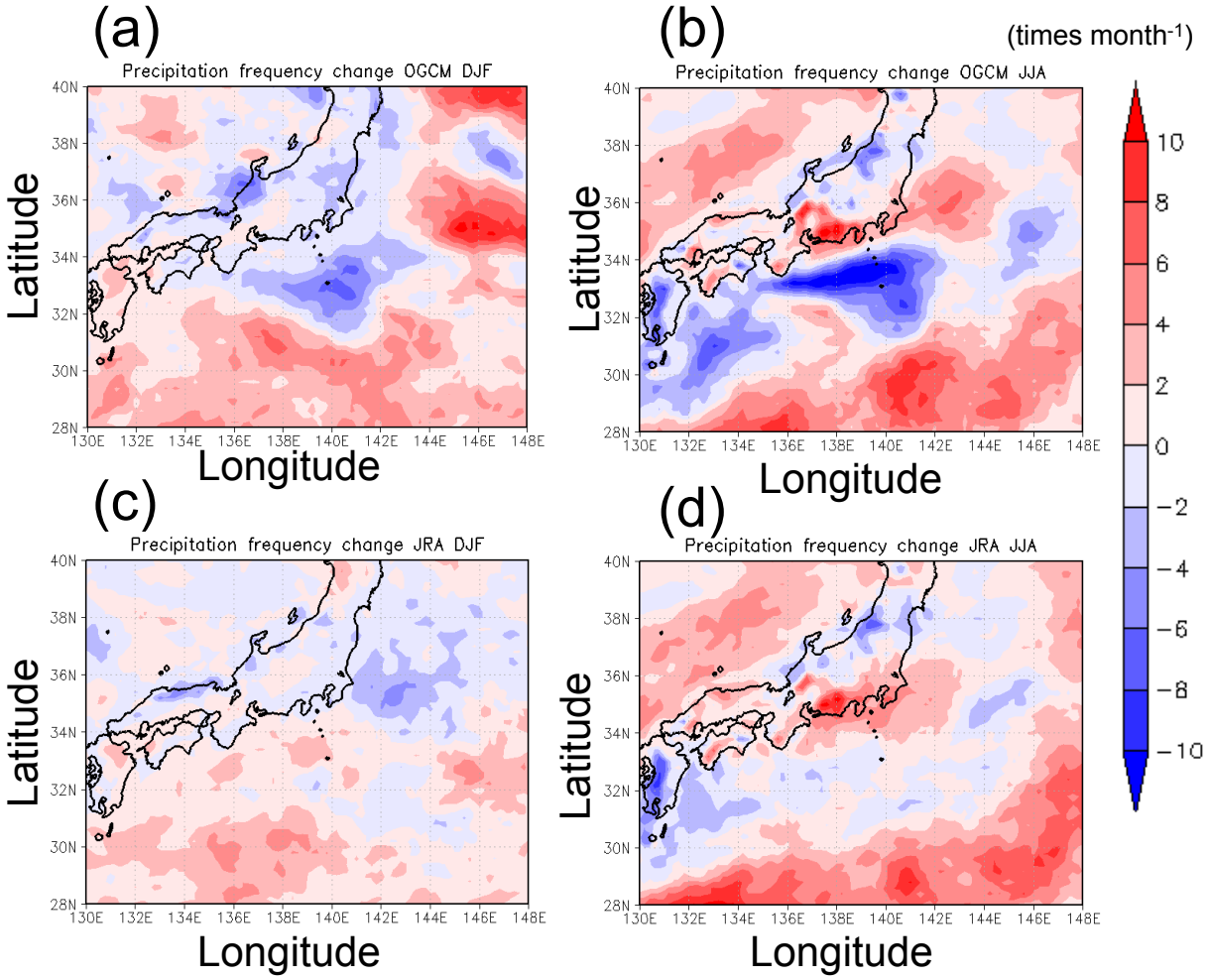

Fig. 4.16 Changes in seasonal averaged frequencies of high intensity rainfall events (times month^{-1}) between the Kuroshio LM and SP phases (LM minus SP), as predicted by the OGCM-run for (a) winter (December–February) and (b) summer (June–August), and by the JRA-run for (c) winter and (d) summer.

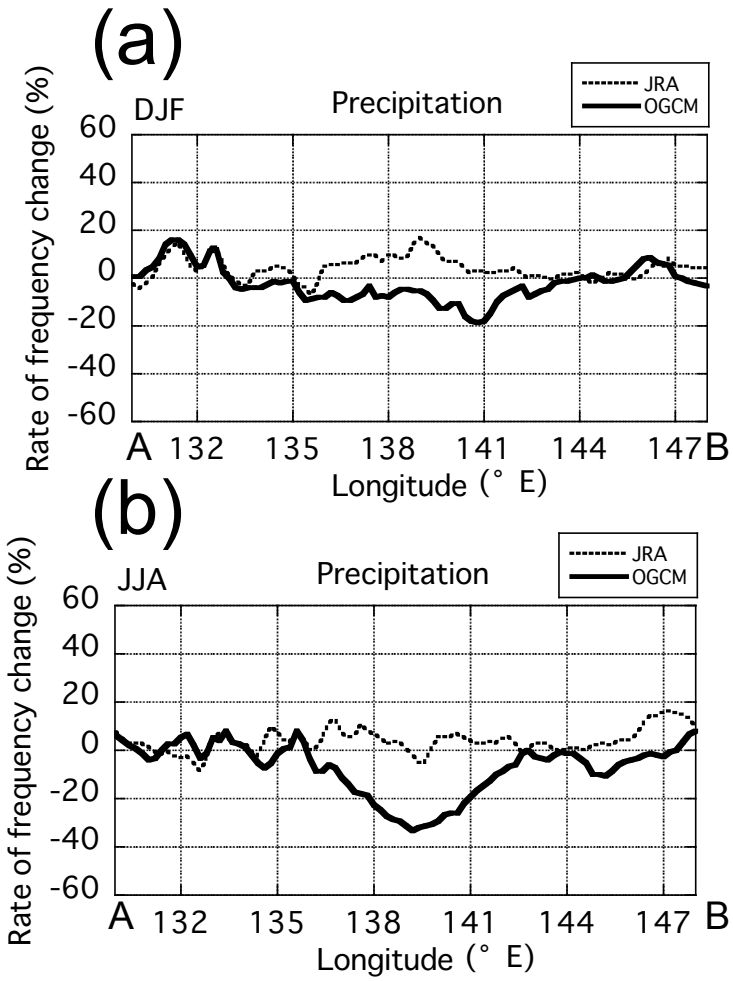

Fig. 4.17 Rate of change, calculated as (LM–SP)/SP and expressed as a percentage, in frequency of high intensity rainfall events in (a) winter and (b) summer, as predicted by the JRA-run (dashed line) and the OGCM-run (bold solid line), along 33.6 °N (line A–B in Fig. 4.12a).

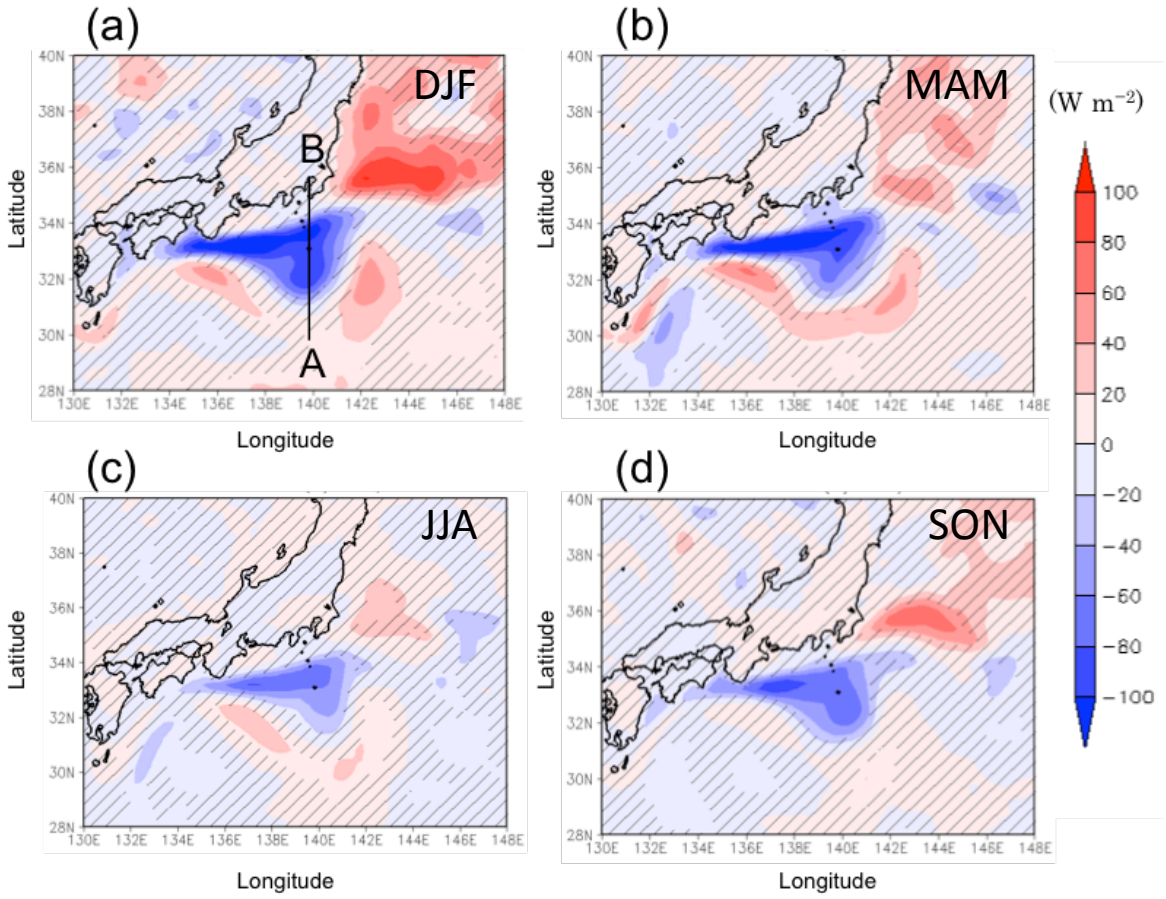

Fig. 4.18 Seasonal averaged total heat flux (W m^{-2}) variations between the Kuroshio LM and SP phases in (a) winter (December–February), (b) spring (March–May), (c) summer (June–August), and (d) autumn (September–November). Hatched areas indicate no significant difference at 90 % level. The line from A to B shows the cross section of Fig.4.21.

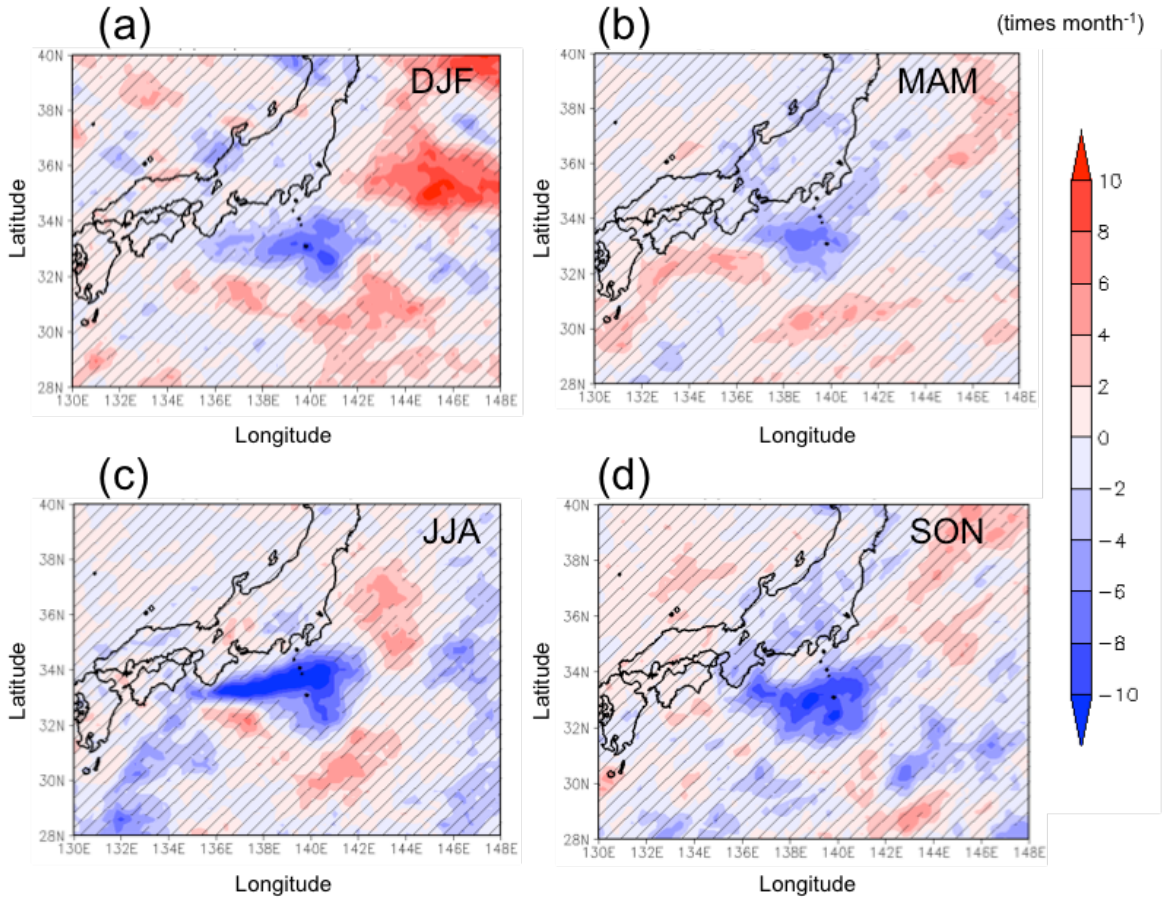

Fig. 4.19 Seasonal averaged frequency of high intensity rainfall events (times $month^{-1}$) between the Kuroshio LM and SP phases in (a) winter (December–February), (b) spring (March–May), (c) summer (June–August), and (d) autumn (September–November). Hatched areas indicate no significant difference at 90 % level.

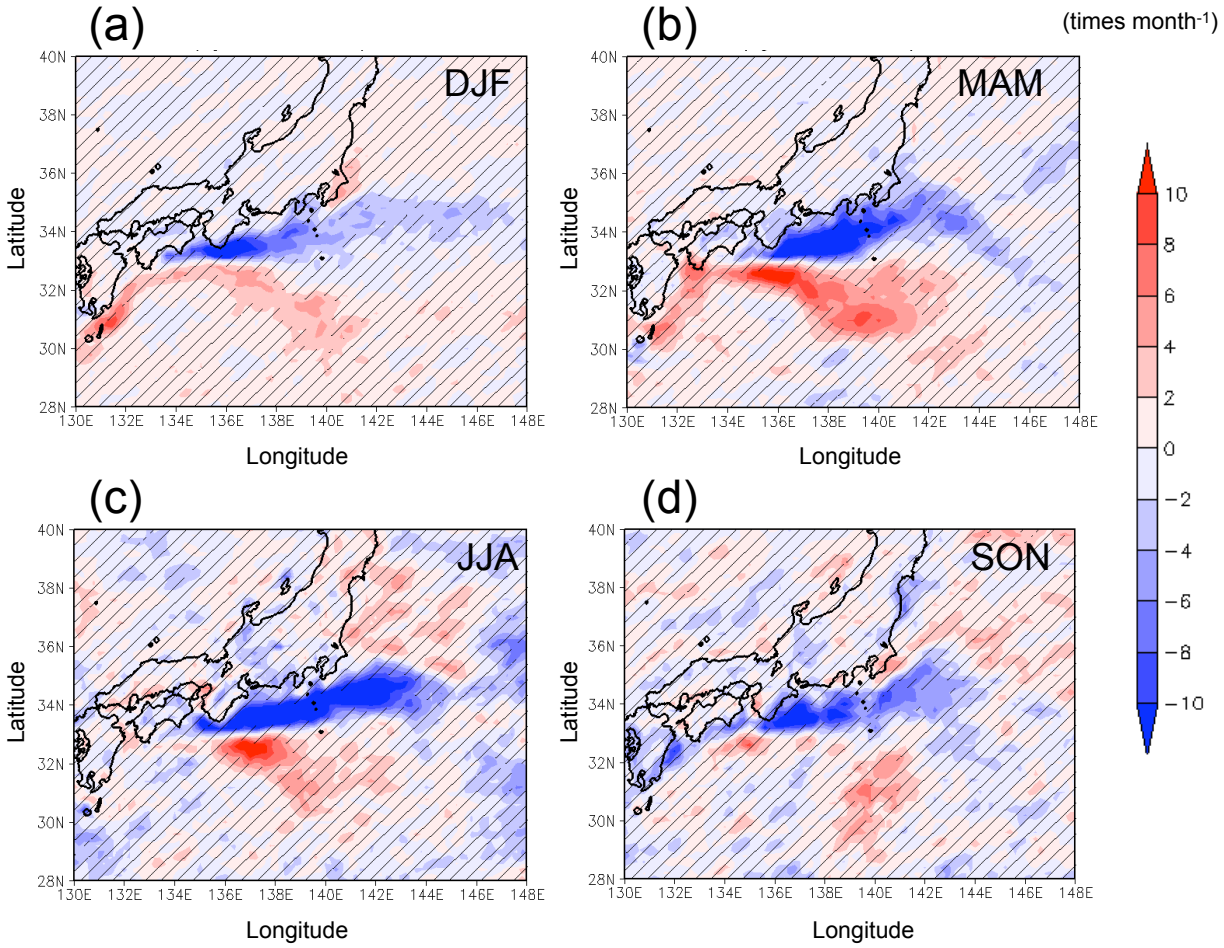

Fig. 4.20 Seasonal averaged frequency of $|\nabla_h \theta_e|$ that exceeds 0.1 K km^{-1} (times month^{-1}) between the Kuroshio LM and SP phases in (a) winter (December–February), (b) spring (March–May), (c) summer (June–August), and (d) autumn (September–November). Hatched areas indicate no significant difference at 90 % level.

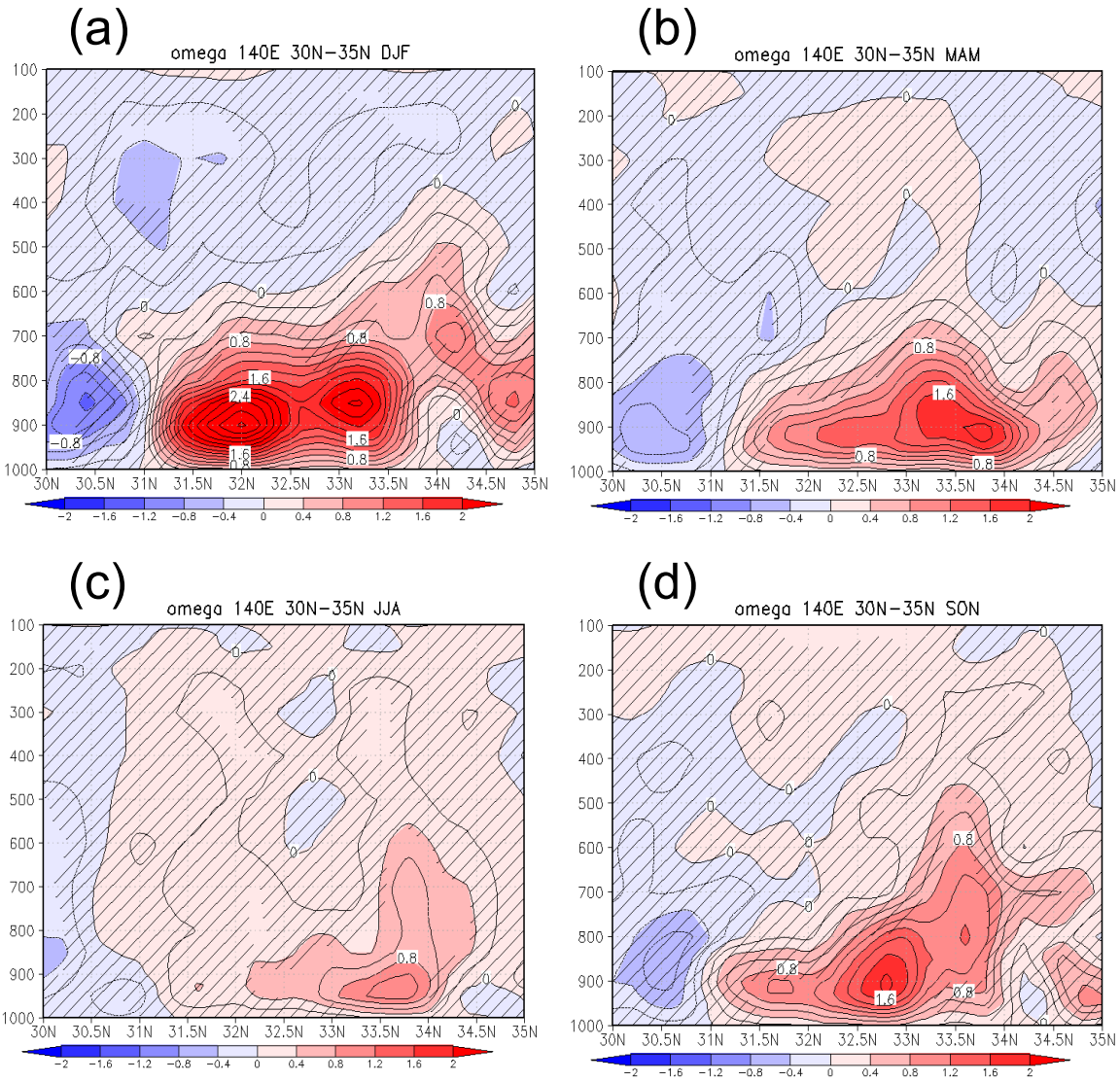

Fig. 4.21 Cross-section view of vertical wind in (a) winter, (b) spring, (c) summer, (d) autumn, along the line A–B (30 °N-35 °N, 140 °E) in Fig. 4.18(a). The unit is hPa hour^{-1} and contour intervals are 0.2 hPa hour^{-1}. The hatches indicates confidence interval less than 90 %.

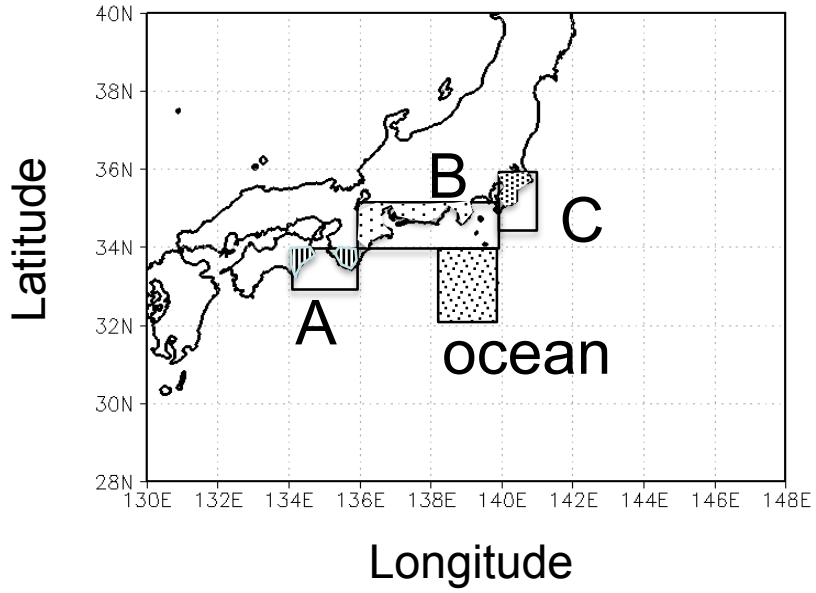

Fig. 4.22 Definition of three land areas and the cold SST pool area used in the analysis of the effects of the Kuroshio LM on Japan's weather. Area A: From 33 °N to 34 °N and from 134 °E to 136 °E; area B: From 34 °N to 35 °N and from 136 °E to 140 °E; area C: From 34 °N to 36 °N and from 140 °E to 141 °E; ocean: From 32 °N to 34 °N and from 138 °E to 140 °E.

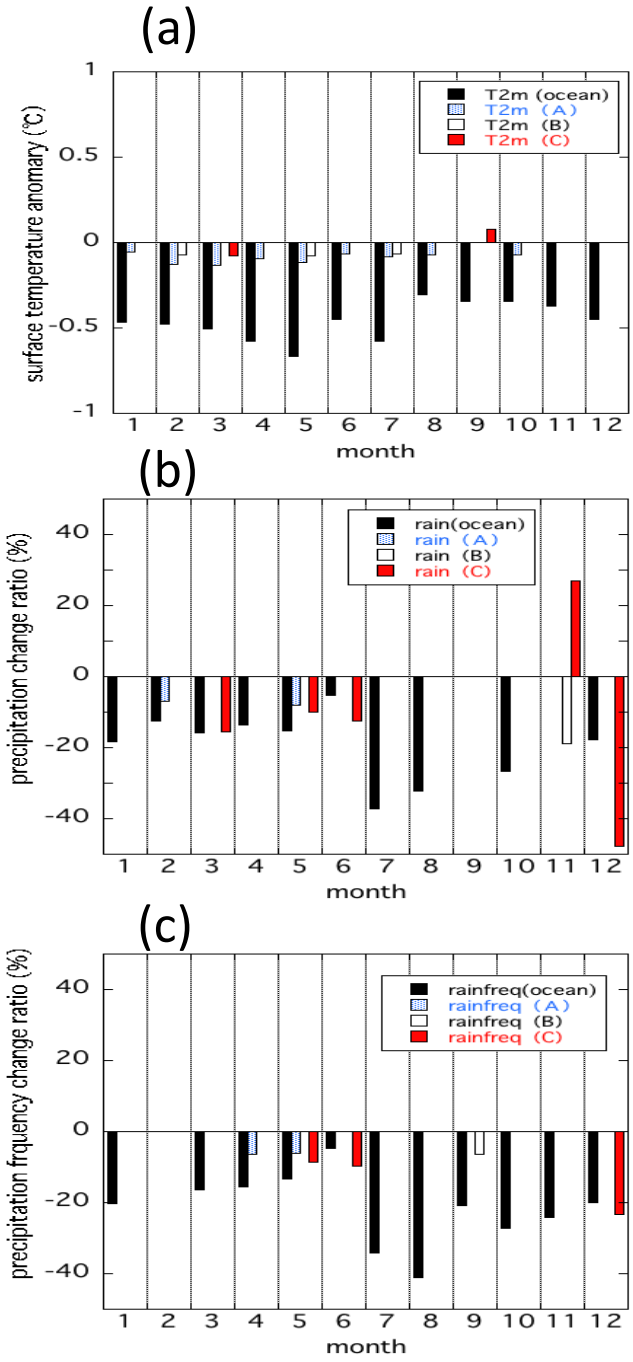

Fig. 4.23 Area-averaged seasonal changes between the Kuroshio LM and SP phases in terrestrial (a) SAT (°C), (b) precipitation change ratio (%) and (c) change ratio of the frequency of high intensity rainfall events (%). The horizontal axis represents the month. Only the significant differences at the 90 % level are presented.

	SAT−SST	heat flux	water vapor flux	precipitation
JRA−run	−2.4	196.11	−1.35E−05	157.11
OGCM−run	−2.55	213.7	−1.41E−05	164.99

Table 4.1 Twenty-year-averaged area, mean SAT–SST, total heat flux [W m^{-2}], water vapor flux convergence [s^{-1}], and precipitation [mm $month^{-1}$]. Upper row: JRA-run result. Lower row: OGCM-run. Area (30 °N–33 °N, 134 °E–142 °E) is shown in Fig. 4.7 a and b.

CHAPTER 5 Discussion

5.1 The mechanism causing the change in intense rainfall frequency in summer

As previous chapter mentioned, surface heat flux change is greater in winter than in summer (Fig. 4.18); however, the change in rainfall frequency was greater in summer than in winter. Here, we investigate the cause from the perspective of the vertical profiles of EPT. In this chapter, note the definition of differences between LM and SP is based on the equation (4-4).

Figure 5.1 depicts the vertical profiles of the difference in temperature and EPT between the LM and the SP states averaged over a rectangular area from 32 °N to 34 °N and from 138 °E to 140 °E. In comparison with the JRA run, which serves as a reference for natural variation, the OGCM run predicted that temperature near the surface would be relatively colder in the Kuroshio LM than in the SP state. The decrease in the surface temperature of the LM state in the OGCM run was larger by approximately 0.6 K in winter (Fig. 5.1a) and approximately 0.4 K in summer (Fig. 5.1b) than that in the JRA run. The change in EPT was more pronounced than that in temperature in both summer (approximately 1.2 K) and winter (approximately 1.0 K; Figs. 5.1c and 5.1d).

We examined the vertical EPT gradient by considering the difference between the 950 hPa and 700 hPa levels in the cold pool area. If the vertical EPT gradient is positive ($\frac{\partial EPT}{\partial p} > 0$), the lower atmospheric layer is unstable, and if it is negative ($\frac{\partial EPT}{\partial p} < 0$), the lower atmospheric layer is stable.

We took the difference in the frequency of occurrence of a range of vertical EPT gradient values (divided into categories 0.02 K hPa^{-1} apart), which were calculated at 3-hourly intervals, between the two states (LM minus SP), for both the OGCM- and JRA- runs (Fig. 5.2). To elucidate the effect of the LM on vertical EPT gradients, we compared the frequency change

predicted by the OGCM-run, in which the LM is relatively exaggerated, with that predicted by the JRA run. In winter, the frequency change in the OGCM-run was more negative than that in the JRA-run when the vertical EPT gradient was above −0.01 K hPa^{-1} (Fig. 5.2a). However, when the vertical gradient was below −0.01 K hPa^{-1}, the frequency change in the OGCM-run was more positive. This suggests that atmospheric stability increases when the Kuroshio is in the LM state.

Summer results are separated by month (Figs. 5.2b, 5.2c and 5.2d) because intra-seasonal variation is substantial in summer as a result of the baiu front and the Pacific subtropical high. In June, the change in the frequency of vertical EPT gradients in the OGCM-run in comparison with those in the JRA-run tended to be more negative for vertical EPT gradients of more than 0.01 K hPa^{-1} and more positive for gradients of less than 0.01 K hPa^{-1} (Fig. 5.2b). Frequency change signals were very weak in July (Fig. 5.2c), but in August frequency change in the strongly unstable range (0.06 K hPa^{-1} or more) was strongly negative in the OGCM-run (Fig. 5.2d). Therefore, although the frequency of vertical EPT gradients decreased for positive (unstable) gradients in both summer and winter in the cold SST pool of the Kuroshio LM, frequency in the strongly unstable range decreased substantially in summer. This implies that the depression of near-surface EPT was responsible for the reduced frequency of high-intensity rainfall events in summer.

5.2 The mechanism of affecting wind by the Kuroshio LM

In the OGCM-run, the LM state caused a marked change in wind at the 950 hPa level over the cold pool in comparison with the SP state (Figs. 5.3a and 5.3b). This change was weak to absent in the JRA run (Figs. 5.3c and 5.3d).

Two mechanisms have been proposed to explain the effects of SST anomalies on wind: vertical mixing (Wallace et al. 1989; Nonaka and Xie 2003) and pressure adjustment (Lindzen and Nigam 1987; Minobe et al. 2008). These mechanisms have been mainly studied over the

oceanic western boundary currents such as the Gulf Stream and the Kuroshio. The vertical mixing mechanism states that increased static stability around a cold SST pool induces reduced vertical mixing, thereby inhibiting momentum transport from above into the lower boundary layer. This results in a decrease in wind speed near the surface. The pressure adjustment mechanism states that increased SLP around the cold SST anomaly causes a pressure gradient between the areas of higher and lower SLP, inducing a change in surface wind.

Xu et al. (2010) investigated these two mechanisms by examining the differences between atmospheric states in the LM state (from November 2004 to March 2005) and the artificially smoothed SP state. We investigated how these mechanisms may have contributed to changes in winds over the cold SST pool.

Following the horizontal atmospheric momentum equations of Xu et al. (2010),

$$\frac{Du}{Dt} = -\frac{1}{\rho}\frac{\partial p}{\partial x} + fv - \frac{\partial \overline{u'w'}}{\partial z} + D_u \qquad (5\text{-}1)$$

$$\frac{Dv}{Dt} = -\frac{1}{\rho}\frac{\partial p}{\partial y} - fu - \frac{\partial \overline{v'w'}}{\partial z} + D_v, \qquad (5\text{-}2)$$

where u and v indicate horizontal wind; w indicates vertical wind; u', v', and w' represent the turbulent fractions of u, v and w, respectively; and ρ and f indicate air density and the Coriolis parameter, respectively. D_u and D_v indicate horizontal mixing.

We focus on the first and third terms on the right hand side of equations (1) and (2), which are related to pressure adjustments and vertical mixing. For analyzing the equations, we used the 950 hPa level as the typical height of a boundary layer, although this height may slightly vary between the LM and the SP states.

In winter, the pressure gradient term revealed a clear divergence field above the cold pool (Fig. 5.4a), which corresponds with the results of Xu et al. (2010). This suggests that increased

SLP caused by the cold pool can create a divergent flow. In summer, a similar but less pronounced distribution appeared (Fig. 5.4b). Although the pressure adjustment mechanism does cause a change in the wind over the cold SST pool, this effect is strengthened when the seasonal wind flows in the same direction, and is weakened when it flows in the opposite direction. For example, the winter seasonal wind around Japan is north-westerly, so the wind blows more powerfully on the lee (or south) side of the cold SST pool. This result is consistent with the findings of Xu et al. (2010), who suggested that the influence of the change in wind direction caused by the high SLP anomaly is strengthened on the lee side of the periodic wind in the winter season.

The vertical mixing term was quite small in comparison with the pressure gradient term (Fig. 5.5), although the vertical mixing term may have been underestimated at 950 hPa owing to the effect of surface friction. The analyses presented here are consistent with the recent findings by Liu et al. (2013), who showed that the pressure adjustment mechanism tends to dominate on monthly to seasonal time scales whereas the vertical mixing mechanism dominates on shorter (2 to 6 days) time scales (Booth et al. 2010).

5.3 Moisture balance variations between LM and SP state

In the previous chapter, decrease in precipitation frequency occurs in the vicinity of the cold SST pool (Fig. 4.19). In the Kuroshio LM period, the cold SST pool causes a considerable drop in potential temperature through turbulence heat flux, and convection activity weakens as a result of the strength of the stability of the boundary layer. However, precipitation frequency does not necessarily decrease in the cold SST area only. To investigate the cause of a decrease in precipitation in greater detail, we investigated the moisture budget in January, which period is dominated by northwesterly winds, and in June, which is the rainy season dominated by the baiu front.

$$\frac{\partial W}{\partial t} = -\int_{Ptop}^{Psfc} \nabla \cdot < q\boldsymbol{V} > \frac{dp}{g} + E - P \qquad (\mathbf{5-3})$$

Where W is precipitable water, $q\boldsymbol{V}$ is moisture flux, P is precipitation, E is evaporation, g is gravitational acceleration, and *Psfc* and *Ptop* are the pressure levels of the model bottom and top layer, respectively. As the amount of water vapor in the altitude above 250 hPa is extremely low, *Ptop* was set to 250 hPa.

Each term of the right side of the equation (5-3) was analyzed separately. Fig. 5.6 shows variations in SST, precipitation, evaporation, water vapor flux and vertical integrated moisture flux convergence (here after, Qconv, following the expression of Kuwano-Yoshida et al. 2013) and moisture flux at 950 hPa level in January. The negative signal in evaporation was shown to correspond to the cold SST pool (Fig. 5.6c). In contrast, precipitation was not entirely correlated with that area (Fig. 5.6b). The change in Qconv was similar to that in precipitation (Fig. 5.6d), and change in moisture flux corresponded well with the pressure gradient term in Fig. 5.4a.

In June, evaporation change was similar to SST change (Fig. 5.7a and 5.7c), while precipitation change was not (Fig. 5.7b). In contrast to January, the moisture flux change extended to the Pacific Ocean side of Japan. The distribution of Qconv showed good agreement with the area of precipitation decrease, especially in the Kanto district and in near-shore sea areas (Fig. 5.7d). This could not be explained by evaporation change only. The results indicate that evaporation and atmospheric stability change over the cold SST pool is one of the factors involved in changing precipitation, but also that change of moisture flux due to the pressure gradient plays an important role in change precipitation outside of the cold SST pool. As previously shown in section 5.2, because Japan is on the windward side of the cold SST pool in January, the effect of the wind change is counterbalanced by northwesterly winds (Fig. 5.3). In addition, moisture in June is significant large compare to the winter season. As a result, moisture flux change due to the Kuroshio LM is relatively strong in June when southwesterly winds

dominate.

To clarify further the moisture term changes due to the Kuroshio LM, we investigated monthly changes in Qconv, evaporation, and precipitation along the lines A–B and C–D in Fig. 5.7a. The latitude of negative evaporation does not change very much each month (Fig. 5.8). The latitude where evaporation decreases corresponded to that of the cold SST pool, as previously shown in Figs 5.6a,c and 5.7a,c. However, the negative change of precipitation reaches inland in summer and moves to the south in winter, which cannot be explained by evaporation change.

Conversely, as shown in Fig. 5.9, the change of Qconv corresponds well with precipitation change. This result indicates that the precipitation change due to the Kuroshio LM may occur outside the cold SST pool through the moisture flux. Table 5.1 shows the time correlation coefficients for 12 months between area-averaged precipitation and Qconv and those between area-averaged precipitation and evaporation. The three land regions and the ocean region are defined as in Fig. 4.22. The correlation between precipitation and Qconv was higher than that of evaporation.

In summer, as shown in Fig. 5.9b, Qconv and precipitation decrease in the north of the inland along line C-D (longitude of l40 °E), while along line A-B in Fig. 5.7, the negative Qconv area does not spread to the north side of 34.5 °N (Fig. 5.9a). The main difference between lines A-B and C-D is the relative direction from the cold SST pool and the land topography. Therefore, one of the possible reasons for the difference in the change of Qconv between line A-B and line C-D is the effect of shielding by the mountains which exist on line A-B. Conversely, on line C-D, there is nothing to interrupt the change of moisture flux of the strong southwestern direction on the Kanto plain, and it easily influences the north inland. The result suggests the influence of the Kuroshio LM varies according to the place, even if on the same Pacific side of Japan. This is consistent with Fig. 4.23, which shows the influence of precipitation frequency in the Japanese area.

Finally, we consider the Kuroshio LM influence on atmospheric circulation vertically and

horizontally. Figure 5.10 indicates the vertical latitude cross-section of the change in vertical wind in January and June along line A-B in Fig. 5.7a. When we investigate the difference in the vertical wind between LM and SP, a downward motion appears on the cold SST pool around 33 ˚N both in January and June, just as between the Kuroshio LM and SP. The change extends to the 850–700 hPa level, and an upward motion exists next to the cold SST pool. Figure 5.11 shows the horizontal wind change and its divergence at the 800 hPa level. Wind converges at the 800 hPa level but diverges at the 950 hPa level. This implies the possibility that the SST anomaly due to the Kuroshio LM affects the atmospheric circulation in the lower layer.

As for the atmospheric response to heat sources, the Matsuno-Gill pattern in the tropics is commonly known (Matsuno 1966; Gill 1980). The heat source in the middle troposphere in the tropics produces a pair of cyclonic (anticyclonic) flows at the lower (upper) troposphere. Furthermore, large-scale zonal circulation in the tropics is referred to as the Walker circulation. The easterly wind from the Central Pacific Ocean and westerly monsoon flows from the Indian Ocean to converge at the cyclonic point where the convective is active. The upward flow diverges in the upper troposphere and descends over the East Pacific Ocean and the Indian Ocean (Ueda 2014). These circulations are phenomena in the tropics or subtropics where convection is active. The vertical scale extends up to the upper troposphere and the horizontal scale extends to the basin scale. For the Kuroshio LM, the horizontal scale is several hundred kilometers and the vertical scale is up to the middle of the troposphere (800-850 hPa level). Therefore, the effect is limited in small scale compared to the tropical responses. Nevertheless, it would be worthwhile considering because the Kuroshio LM may affect the convection activity through the change of moisture flux for the regional scale climate in Japan.

5.4 Influence of the Kuroshio path change on social activity in Japan

In recent years, rainfall variation between years with heavy rainfall and those with less

rainfall has become large (MLIT: Ministry of Land, Infrastructure, Transport and Tourism, 2014). This means that serious water shortages can readily occur in small-rainfall years. Figure 5.13 depicts the status of drought occurrence over 30 years from 1983 to 2012 (MLIT, 2014). The frequency of drought is greater in the Pacific Ocean side of Japan. In terms of Japanese use of water resources and future planning, an increase in drought years would be a very important problem. Various factors affect the occurrence of drought, such as rainfall change, but global warming is likely to be the main factor having a long-term effect (JMA, 2013). The Kuroshio LM would not be a main factor in the occurrence of drought in Japan, however, it might have potential to suppress the atmospheric convection, which would cause a drought to worsen more. An increase in drought years would have a seriously influence on agricultural production. For example, Japanese tea, which is a famous agricultural product of the Tokai district, requires precipitation of more than 1300–1400 mm a year. When the Kuroshio LM occurs in a small-rainfall year, its influence may be significant. Nakamura et al. (2012) and Hayasaki et al. (2013) suggested that during the Kuroshio LM period, in winter, the development of cyclones that go through off the south coast of Japan weakens, and the cyclones tend to move south from the Japanese Islands. This research suggests the importance of taking into account the impact of Kuroshio path change in warmer seasons on the utilization plan of water resources.

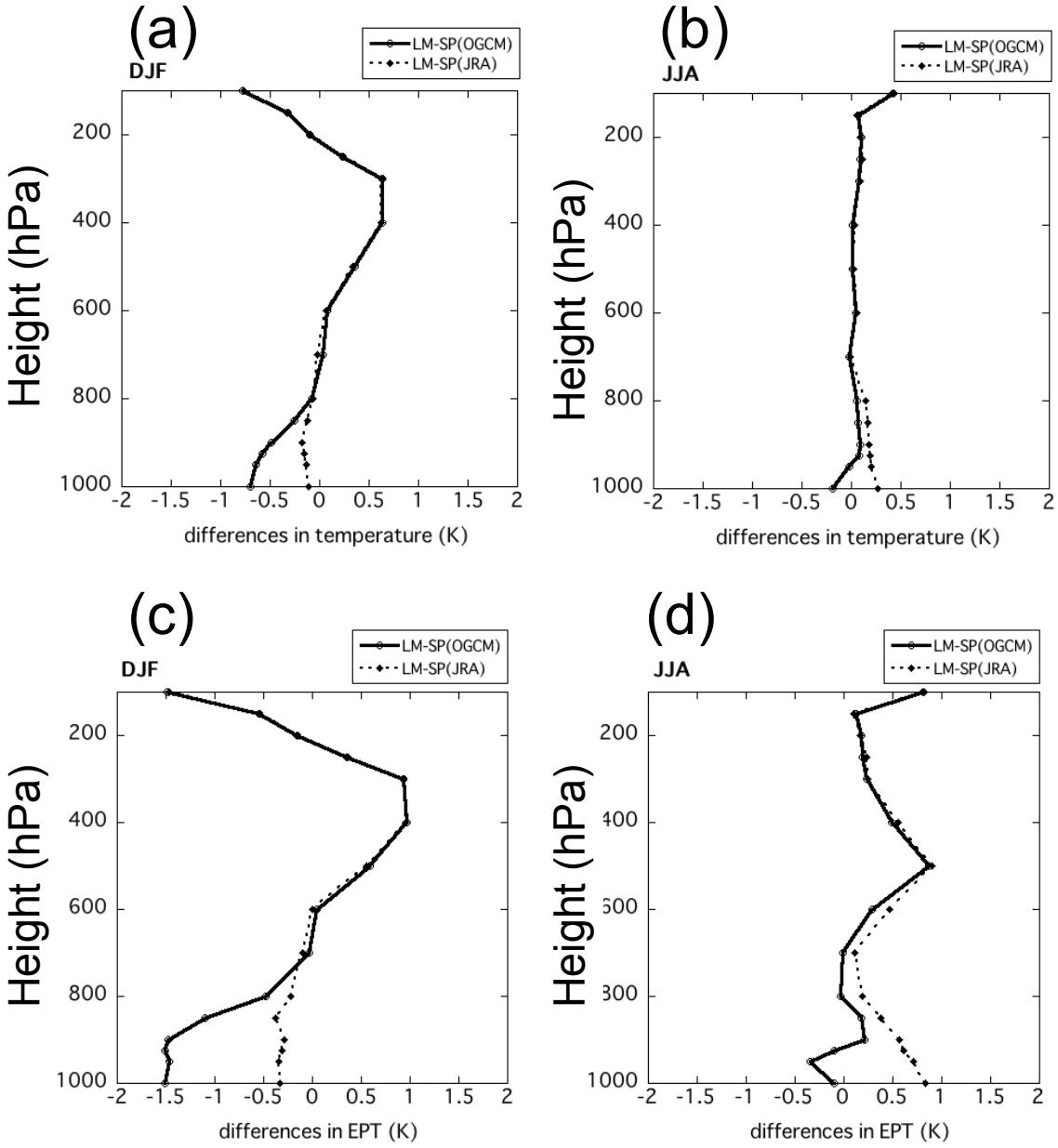

Fig. 5.1 The difference of vertical profiles of area-averaged temperature (K) between the SP and the LM states (LM minus SP) for the OGCM-run (solid line) and the JRA-run (dotted line) in (a) winter and (b) summer, (c, d) same as (a, b) but for EPT. Area averaged from 138°E to 140 °E and from 32 °N to 34 °N, respectively (see also Fig. 4.22).

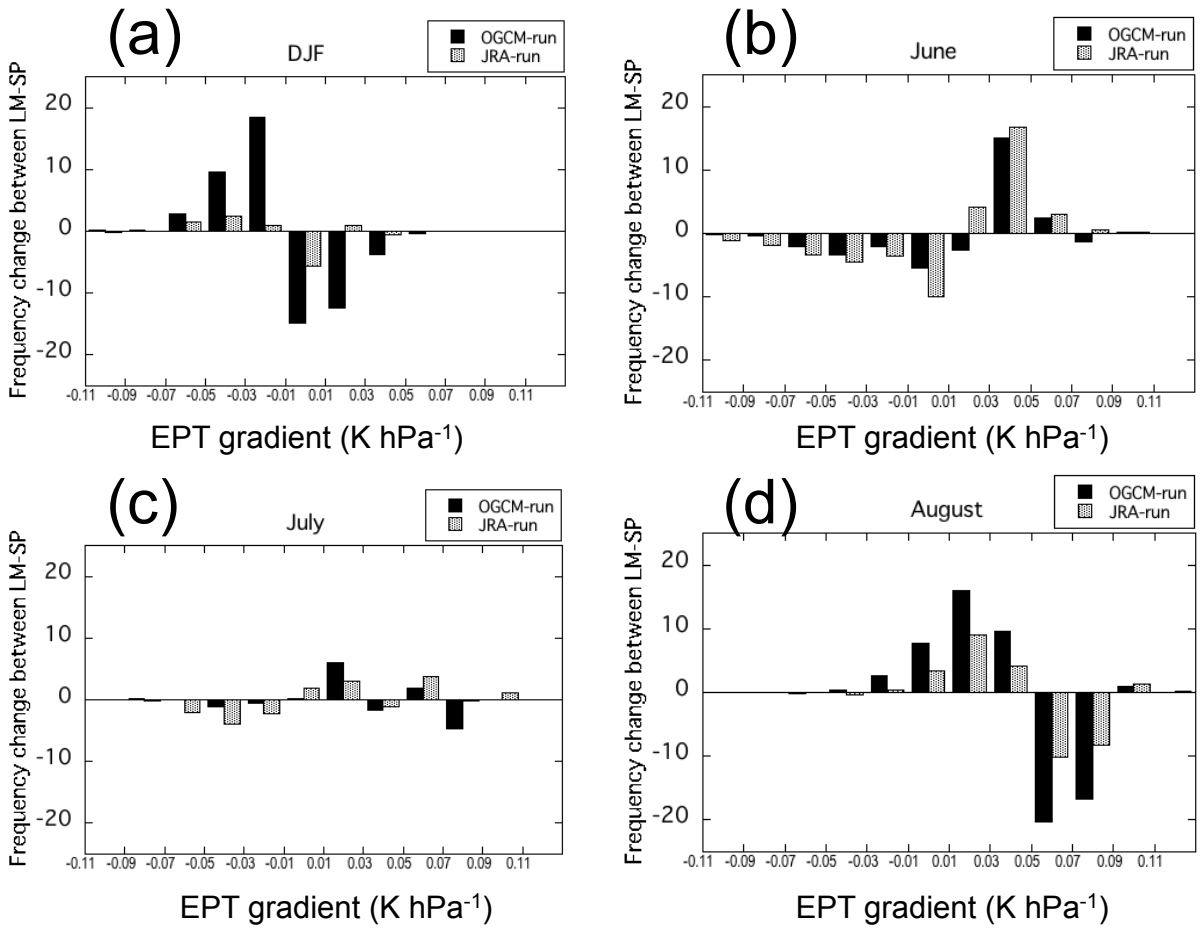

Fig. 5.2 Change in frequency of occurrence of a range of vertical EPT gradients between the 950 hPa and 700 hPa levels, from the SP to the LM states (LM minus SP), in (a) winter, (b) June, (c) July and (d) August. Values are averaged across the area 32 °N 138 °E to 34 °N 140 °E. The horizontal axis gives the EPT gradient $\partial(EPT_{950}\text{-}EPT_{700})/\partial P$ in K hPa^{-1}. Solid bars represent the OGCM run and patterned bars represent the JRA run.

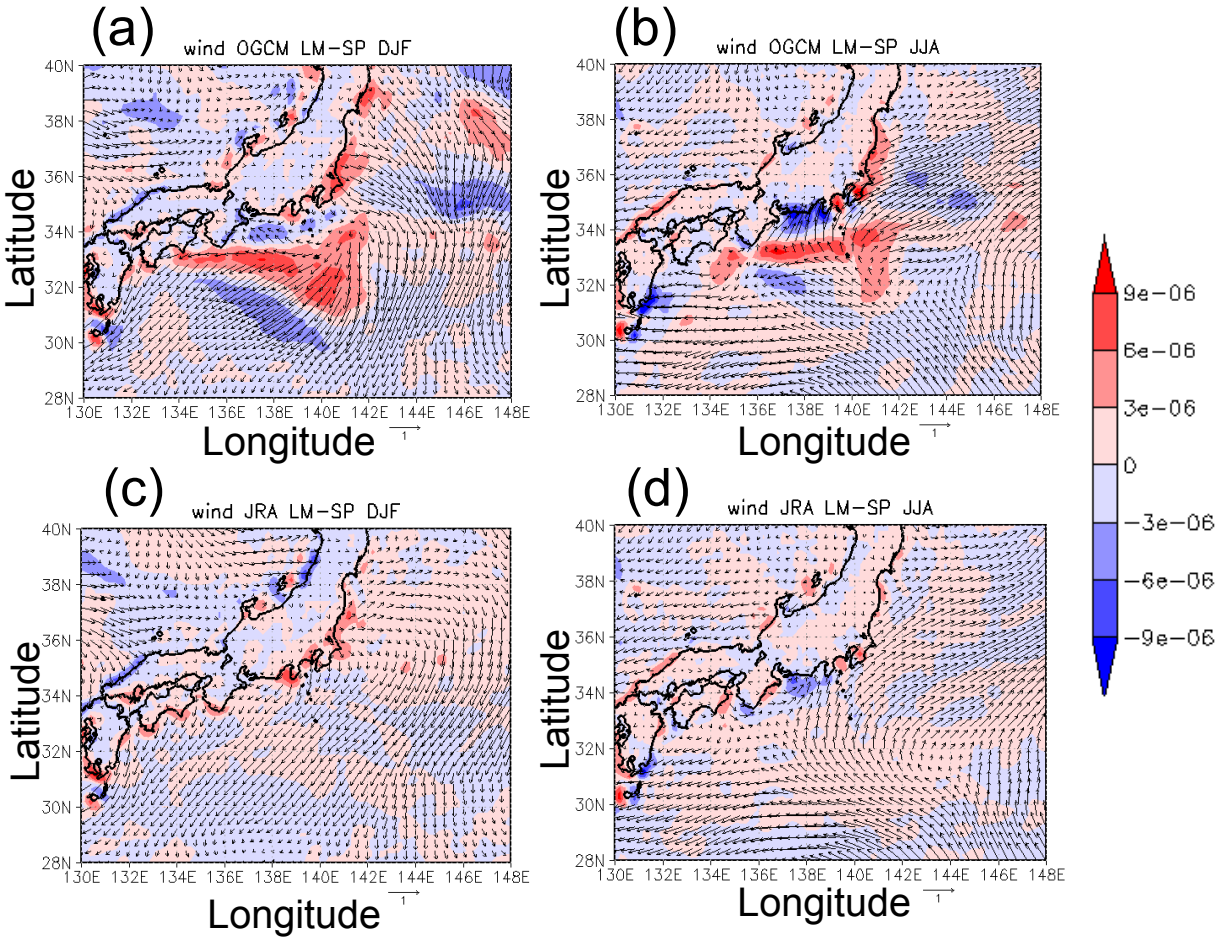

Fig. 5.3 Seasonal averaged differences in wind vectors (m s^{-1}) at the 950 hPa level between the Kuroshio LM and SP phases (LM minus SP), in the OGCM run in (a) winter (December–February) and (b) summer (June–August), and in the JRA run in (c) winter and (d) summer. Red and blue denote divergence (positive) and convergence (negative) of wind vectors (s^{-1}), respectively.

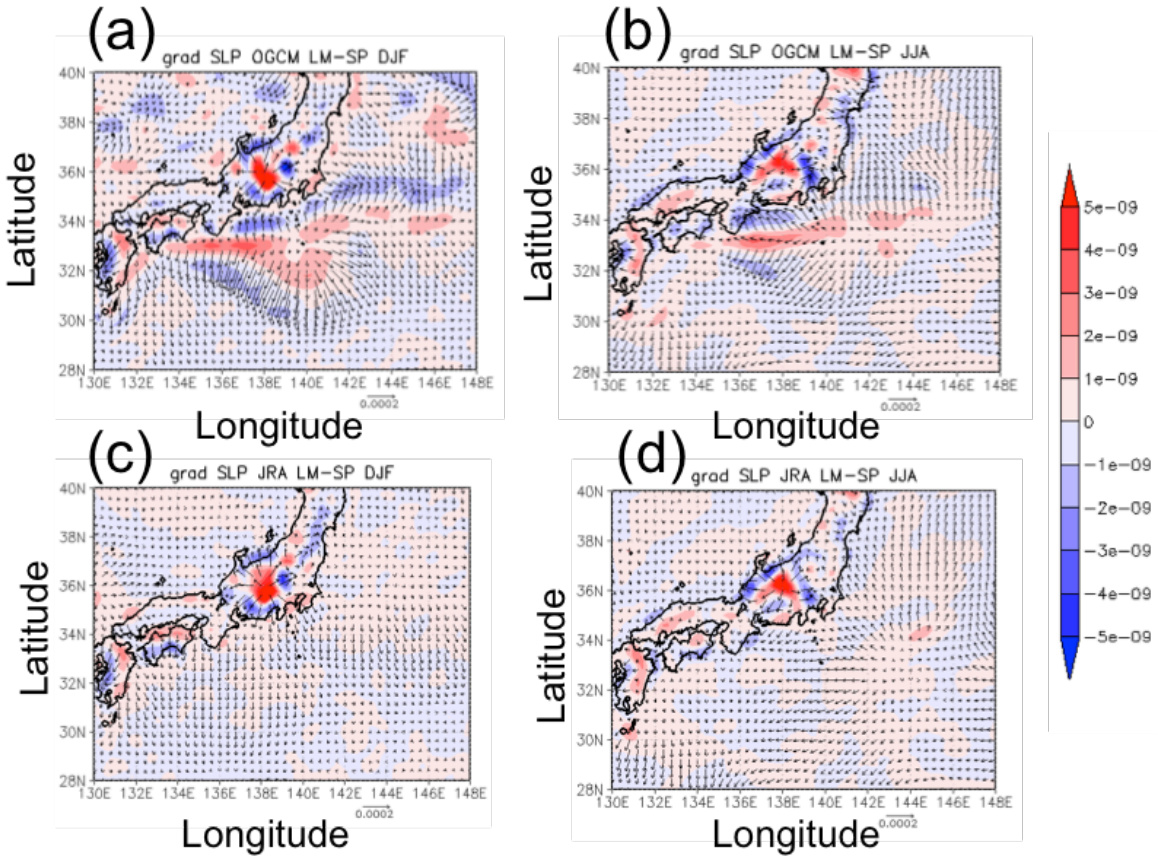

Fig. 5.4 Seasonal averaged differences in pressure gradient terms (m s^{-2}) at the 950 hPa level, between the LM and SP states (LM minus SP), as predicted by the OGCM run in (a) winter and (b) summer, and by the JRA run in (c) winter and (d) summer. Red and blue denote divergence and convergence of the pressure gradient terms (s^{-2}), respectively.

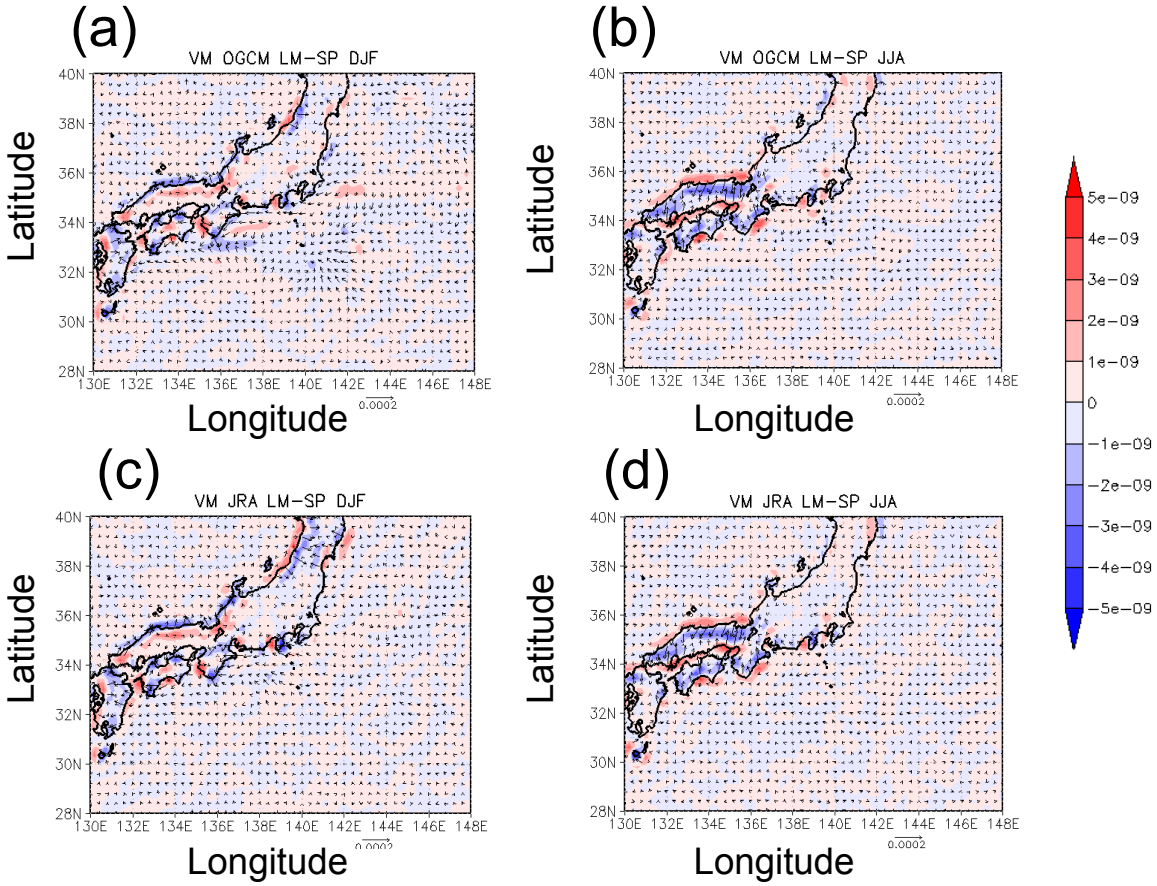

Fig. 5.5 Seasonal averaged differences in vertical mixing terms (m s^{-2}) at the 950 hPa level, between the LM and SP states (LM minus SP), as predicted by the OGCM run in (a) winter and (b) summer, and by the JRA run in (c) winter and (d) summer. Red and blue denote divergence and convergence of the pressure gradient terms (s^{-2}), respectively.

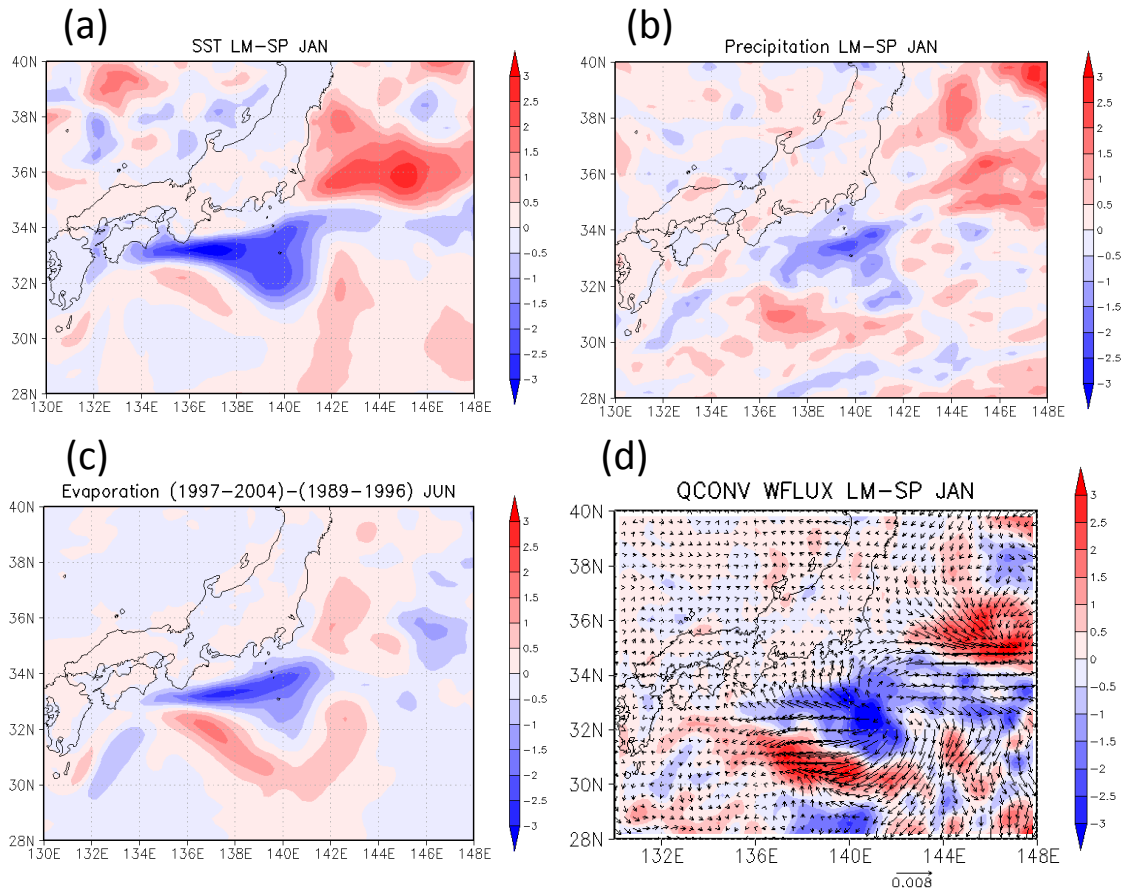

Fig. 5.6 Monthly differences between LM and SP in (a) SST (℃), (b) precipitation (mm day^{-1}), (c) evaporation (mm day^{-1}), (d) water vapor flux (kg kg^{-1} m s^{-1}) and vertical integrated moisture convergence (mm day^{-1}) in January.

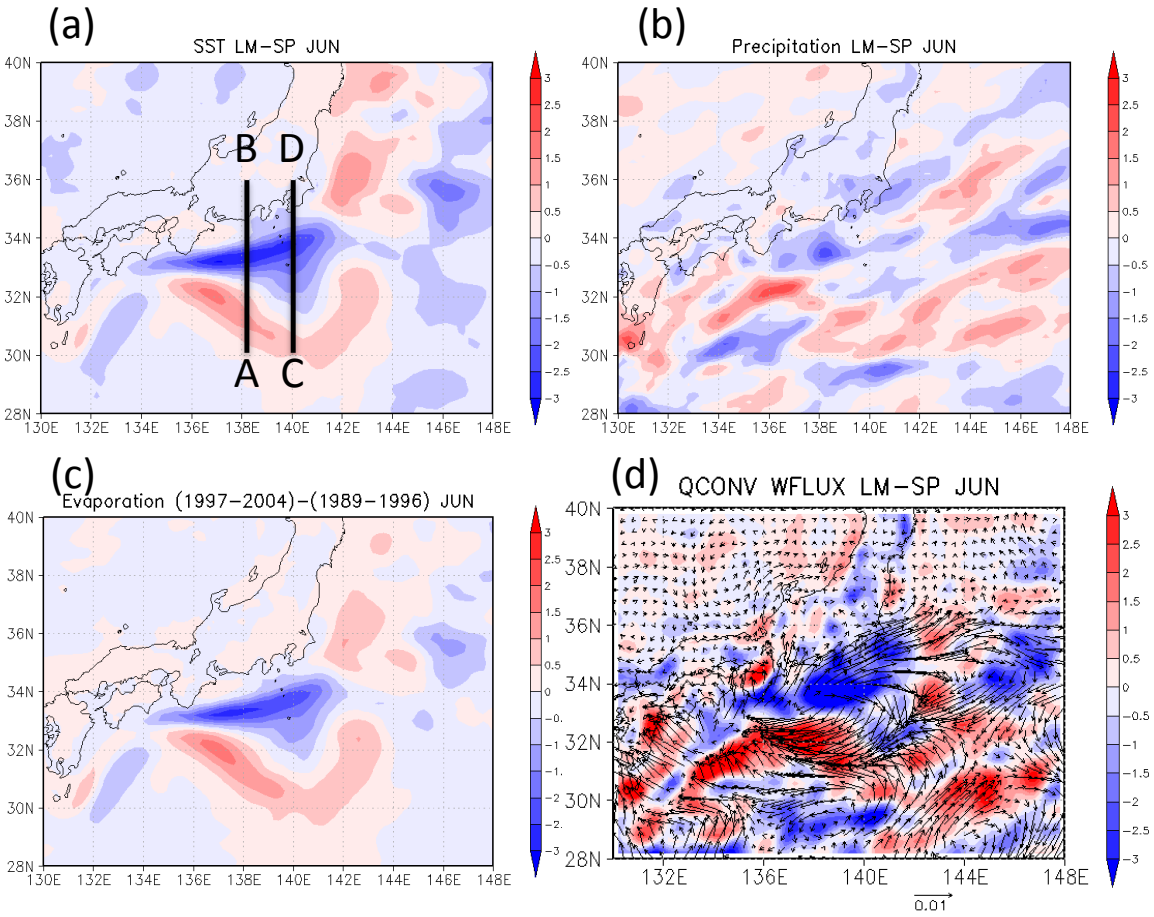

Fig. 5.7 Monthly differences between LM and SP in (a) SST (°C), (b) precipitation (mm day^{-1}), (c) evaporation (mm day^{-1}), (d) water vapor flux (kg kg^{-1} m s^{-1}) and Qconv (mm day^{-1}) in June.

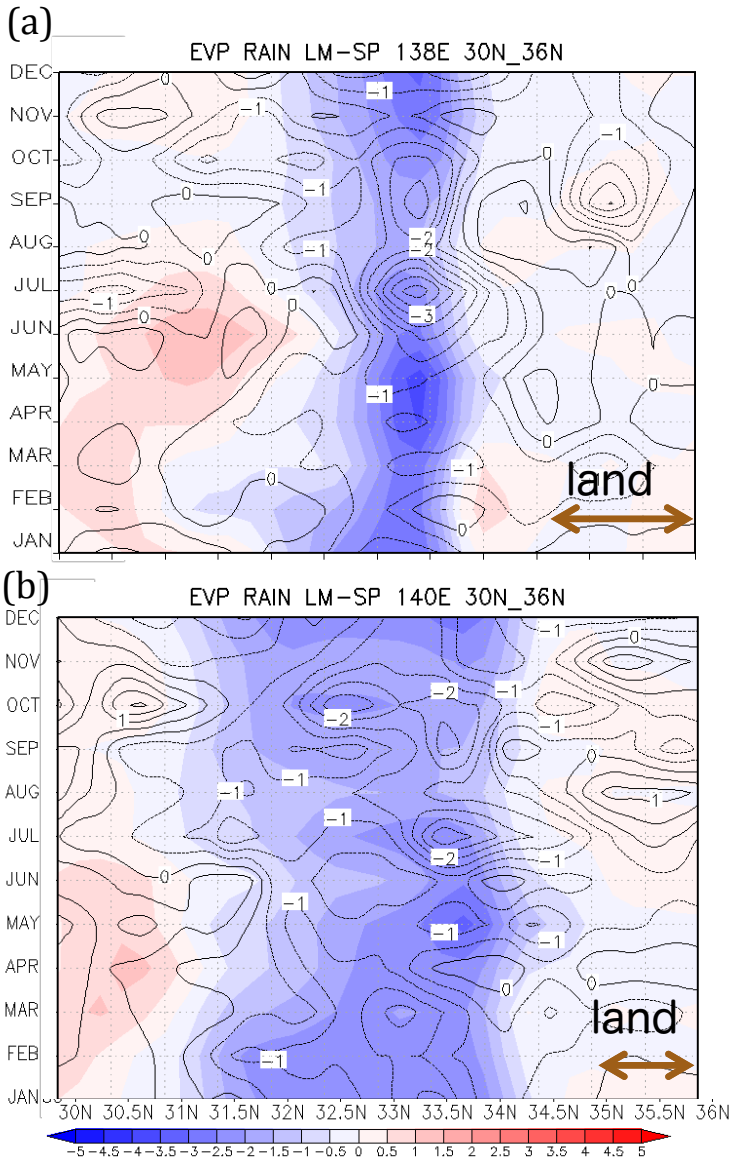

Fig. 5.8 Time-latitude cross section of evaporation differences between the Kuroshio LM and SP phases along (a) the line A-B and (b) the line C-D in Fig. 5.7. The unit is mm day^{-1}. The contour of the both figures denotes SST change. The contour interval is 0.5 °C.

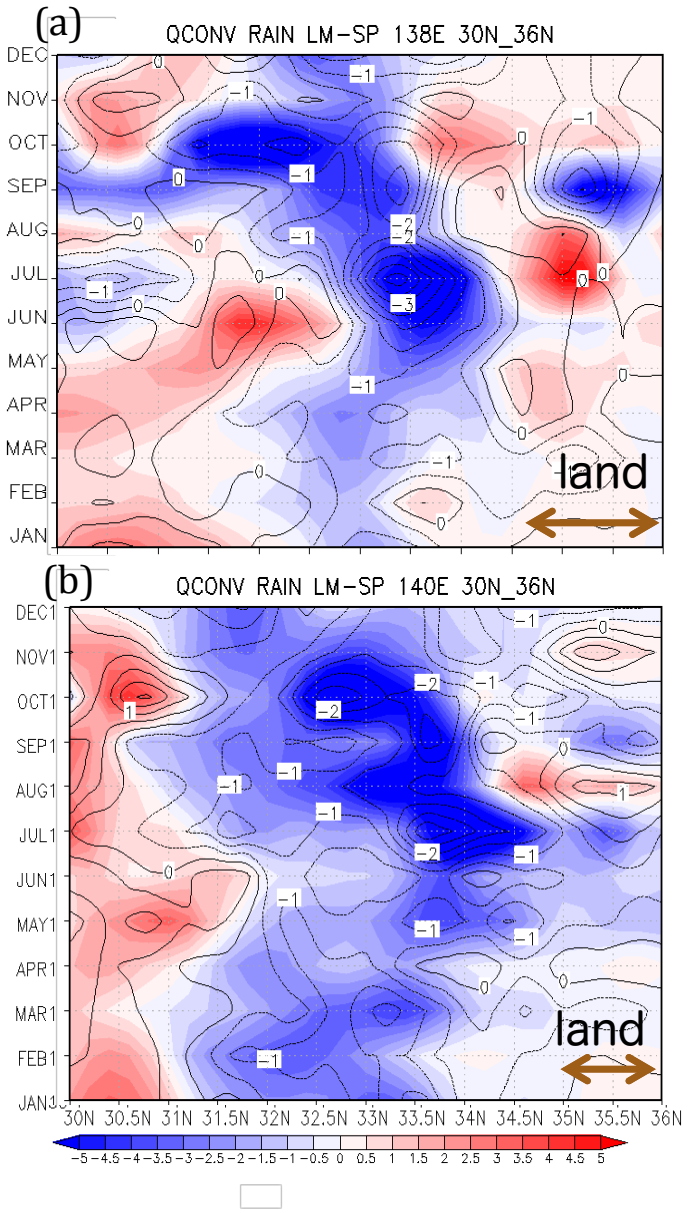

Fig. 5.9 Time-latitude cross section Qconv differences between the Kuroshio LM and SP phases along (a) the line A-B and (b) the line C-D in Fig. 5.7. The unit is mm day^{-1}. The contour of the both figures denotes SST change. The contour interval is 0.5 °C.

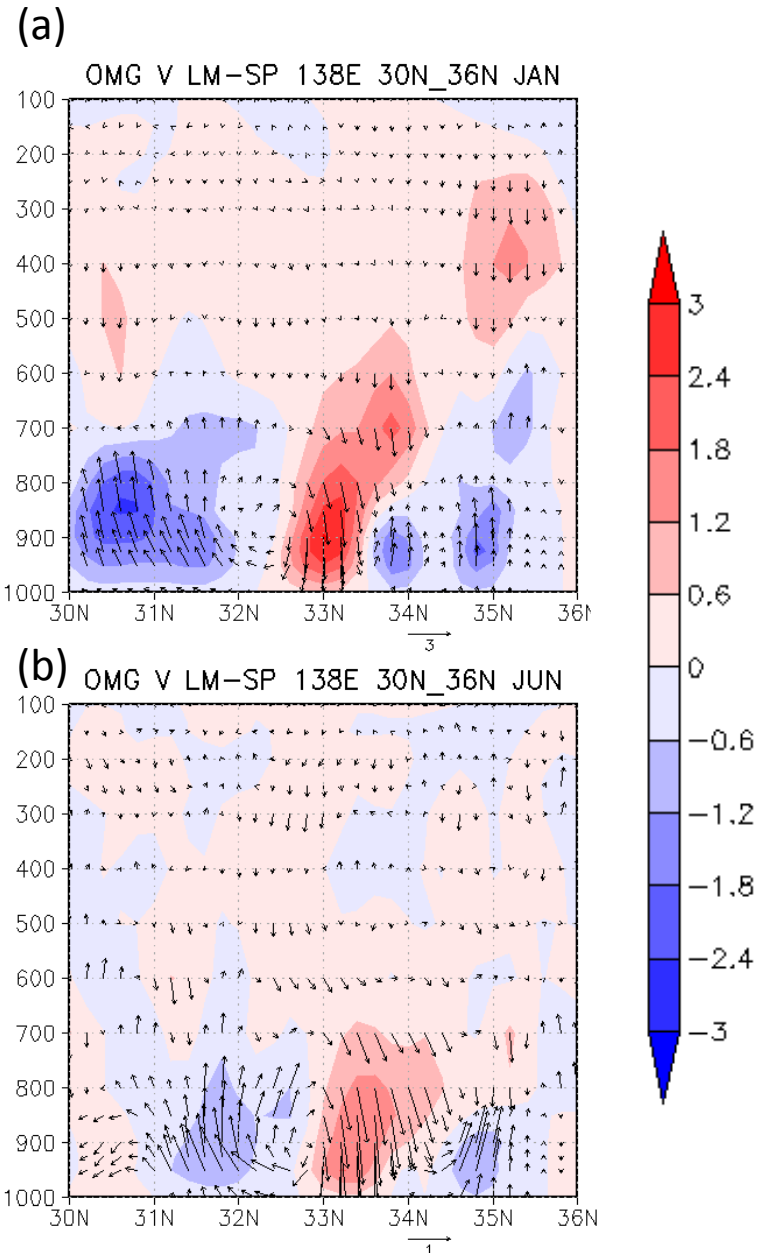

Fig.5.10 Altitude-logitude cross section of vertical wind differences between the Kuroshio LM and SP phases and vector change of meridional wind (v) and vertical wind (w) in (a) January and (b) June along the line A-B in Fig. 5.7. The unit vector represents the v components (3 m s^{-1}) and w (3 hP h^{-1}) in Fig. 5.9 (a), v (1 m s^{-1}) and w (3 hP h^{-1}) in Fig. 5.9 (b).

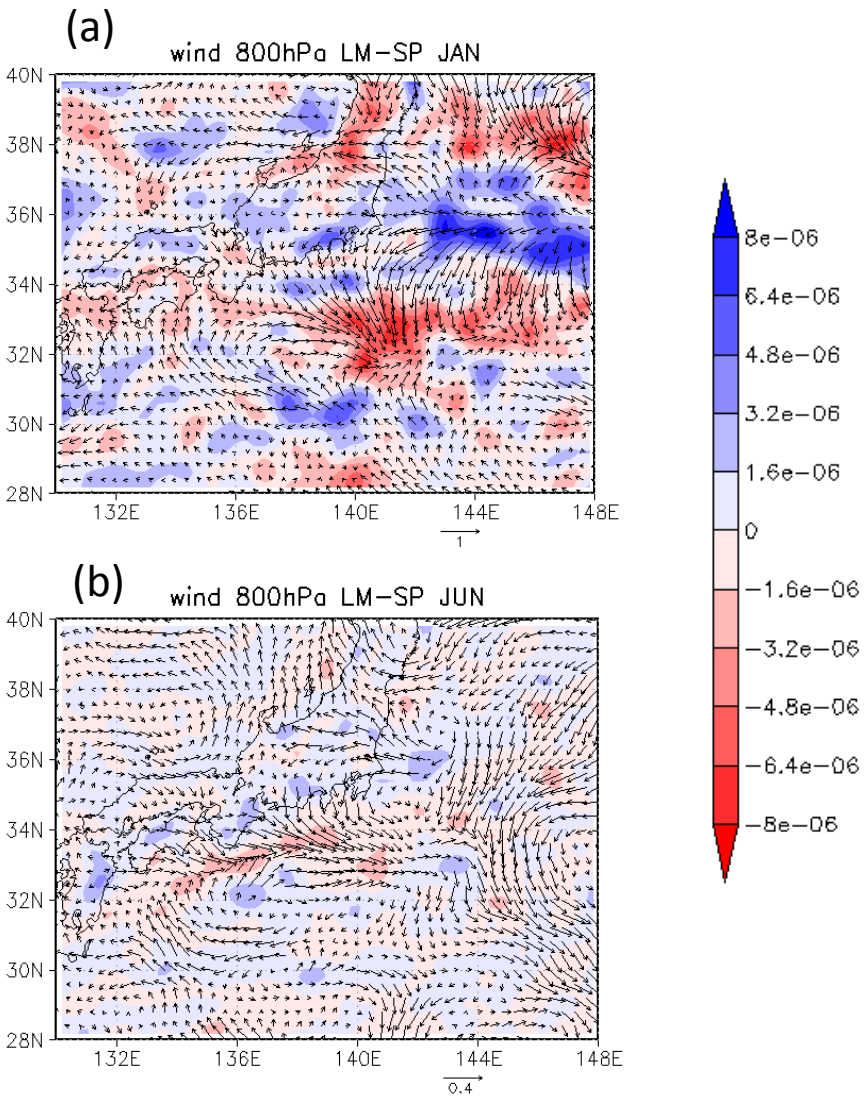

Fig. 5.11 Monthly difference in wind at 800 hPa level in (a) January and (b) June. Red and blue denote convergence and divergence of wind vectors (s^{-1}), respectively.

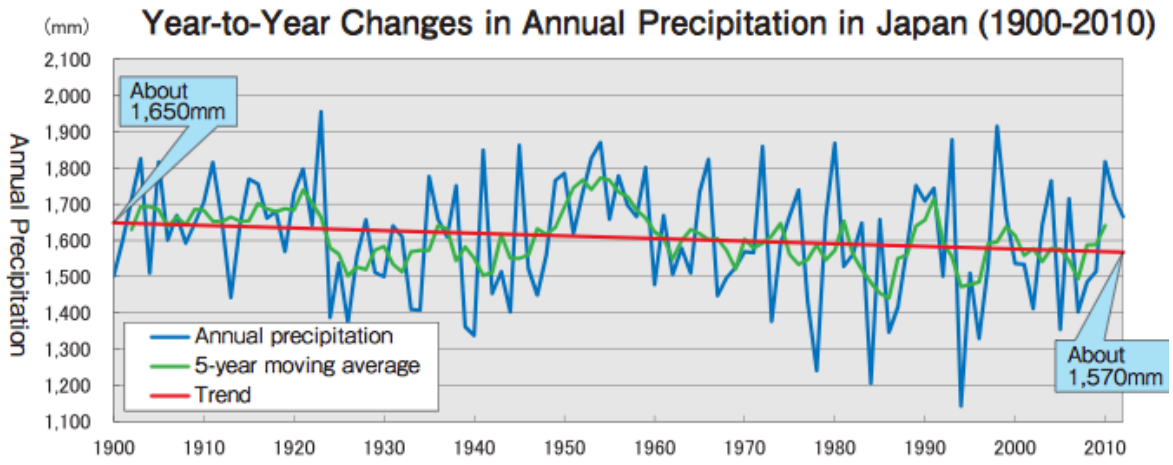

Fig. 5.12 Year-to-year changes in annual precipitation in Japan from 1900 to 2010.

The quotation is from MLIT (2014).

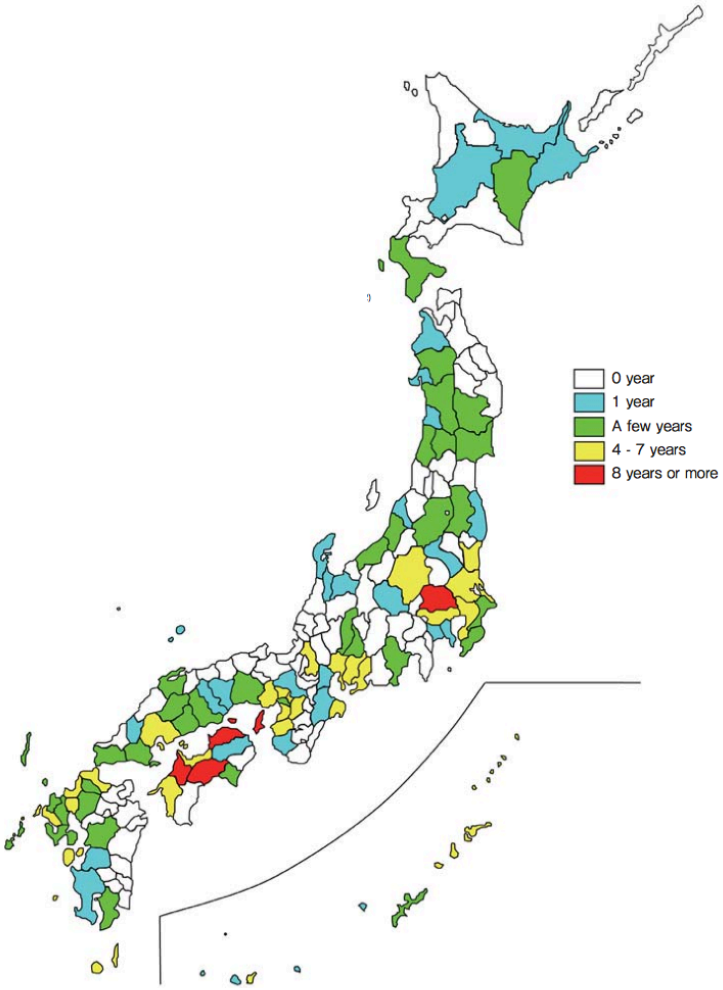

Fig. 5.13 the status of drought occurrence over 30 years from 1983 to 2012.

The quotation is from MLIT (2014).

	Ocean	A	B	C
Qconv	0.88	0.63	0.44	0.43
evaporation	−0.22	0.08	0.37	0.1

Table 5.1 Time correlation coefficients between area-averaged precipitation change and evaporation change, and area-averaged precipitation change and Qconv change. The definition of the three land areas and the ocean area is the same as in Fig. 4.22.

CHAPTER 6 Summary and conclusions

In this study, long-term numerical experiments driven by JRA-25 atmospheric forcing with different kinds of SST data using RCM20 were conducted to estimate the impact of the Kuroshio LM quantitatively and to clarify the mechanism how the cold pool influences on the neighboring convection activity.

Firstly, to investigate the performance of RCM20, we performed 26-years using the regional climate model, RCM20, which is nested within the global re-analysis data, JRA-25, and obtained downscaled climate data over Japan. We evaluated the monthly averaged precipitation for the 7 climatic areas. The result of RCM20 shows significantly improved performance in all areas except in area 7 (the Nansei Islands area). We also evaluated the RCM20 by assessing the accuracy of its precipitation intensity simulations. The results show that the RCM20 is superior to JRA-25 in simulating both daily precipitation intensity and its year-to-year variations, although RCM20 is biased towards lower rainfall events and fails to accurately simulate extreme events, where daily precipitation intensity exceeds 200 mm day^{-1}.

In second, to clarify the SST resolution dependency of RCM20, we conducted a year-long numerical integration using RCM20 with MGDSST which resolution is 0.25 °as a boundary condition. The result showed that the heat fluxes along the warm current clearly increased since Kuroshio and Tsushima warm current were represented more practically. The precipitation decreased by 10-20 % in the Pacific side of Japan and increased by 5-10 % in the side on the Sea of Japan. These results suggested that the SST expression, such as the warm currents, significantly influences the atmospheric elements.

Furthermore, we also investigated how differences in atmosphere forcings change SST in the ocean model. Two kinds of 10-year integration were simulated using a coupled atmosphere-ocean regional climate model (CRCM) to project climate change around Japan with more sophisticated atmosphere-ocean interaction. The model represented SST distribution

relatively well. An SST bias over the Sea of Japan was improved by 10 to 20 % compared to a non-coupled ocean model driven by atmospheric forcing in a GCM. The results indicate that realistic, high-resolution atmospheric conditions impacted positively on the reproduction and projection of oceanic conditions. However, the experiment also showed that the CRCM had a negative bias in the Kuroshio area of the Pacific Ocean side, and a southward bias in the location of the KE. This implies that the upgrade to the resolution of the boundary condition and elaboration from one-way to two-way does not necessarily improve the reproducibility of SST in the entire model area. SST in the future projection simulation was 1 to 6° C warmer than in the present climate run. A particularly remarkable warming signal was projected to the sea east of Hokkaido in both summer and winter. The model also simulated cooling SST off Sanriku (143 ˚E/ 39 ˚N) in winter, which has never obtained by non-coupled ocean model. These projected SST results are likely to be related to future changes in surface wind.

Finally, to quantitatively estimate the impact of the Kuroshio LM and to clarify the mechanism of how the cold SST pool influences neighboring convection activity, we conducted a long-term integration with NPOGCM, which can resolve eddies and currents in detail. NPOGCM effectively reproduced the two main states of the Kuroshio, although the simulated Kuroshio LM was somewhat exaggerated relative to observational data. Using the NPOGCM results as a lower boundary condition, we performed a 20-year simulation for 1985–2004 with RCM20. To detect variations in the atmospheric response to the LM and the SP states of the Kuroshio, we used the composite 8-year mean difference of the RCM to examine atmospheric parameters in regions where SST varied considerably between the two states.

The result showed that in every seasons, the cold SST pool caused substantial decreases in the upward surface turbulent heat flux, the frequency of precipitation, and the frequency of steep horizontal gradients in EPT over the ocean. The difference in the rate of frequency change of high intensity rainfall events between the OGCM-run and the JRA-run around the cold SST was approximately 30-35 % for summer and 20-25 % for winter.

Our simulation indicates that the cold SST pool may have two distinct effects on atmospheric convection and rainfall frequency. First, atmospheric properties, such as EPT, change as a result of decreases in latent and sensible heat fluxes. A decreasing vertical gradient in EPT (taking pressure as the vertical coordinate, i.e., positive downward) over the cold SST pool creates increased atmospheric stability in the lower boundary layer, which is closely related to convection activity. Furthermore, our experiment shows that the frequency of horizontal steep $|\nabla_h \theta_e|$ decreases at the northern edge of the cold pool, suggesting that the frequency of active weather fronts decreases there.

Second, SLP substantially increases, most likely as a result of the cold SST pool. The increase in SLP causes a divergent area over the cold pool and thereby changes surface wind strength via the pressure adjustment mechanism. Change of moisture flux occurring as a consequence of wind and evaporation has an influence on the rainfall frequency in the domain away from the cold pool area. Furthermore, the moisture balance investigation shows the change of precipitation is well correlated to the change of Qconv. This implies that moisture flux and Qconv, vertical integrated moisture flux convergence, are the key factors in explaining precipitation changes due to the Kuroshio LM.

In winter, the high atmospheric pressure anomaly due to the cold SST pool moves to the lee side of the seasonal wind. The change in wind is strengthened in the same direction as a seasonal wind and is offset in the opposite direction. This result is consistent with the preceding study. Conversely, this study showed that the influence of the cold pool area was extended to Kanto on the Tokai district coast and the lee side of the periodic wind in summer, which has been scarcely investigated thus far. Our results suggest the possibility that the occurrence frequency of precipitation also changes in the warmer season as a perspective of the SST variation between the Kuroshio LM and SP mode.

In addition, our results show the changes in surface air temperature, precipitation, and frequency of precipitation in the coastal region on the Pacific Ocean side of Japan during the Kuroshio LM phases. We detected surface air temperature decreases of 0.1 °C–0.2 °C in the

land area closest to the cold SST pool. We also reveal that the precipitation change ratio in the Kanto area was occasionally more than 10 % of the climate. The results imply that the Kuroshio LM may become an important factor for seasonal weather forecasting.

The results suggest that the Kuroshio LM changes atmospheric circulation in the mid-low troposphere. Figure 6.1 presents a conceptual figure of the effect of the Kuroshio LM to the atmosphere. The wind diverges around the cold SST pool and the air descends on the area near the surface, while convergence flow occurs around 800 hPa. There is an ascending motion next to the cold SST pool. The influence is limited in this small scale compared to tropical responses. Nevertheless, it would be worthwhile considering because the Kuroshio LM may affect convection activity through the change of moisture flux for the regional scale climate in Japan.

This research shows that the cold SST pool caused by the Kuroshio LM not only influences atmospheric convection around Japan in winter but also in other seasons, and the influence extends to the land area of Pacific side of Japan. These results will contribute to the studies of regional climate systems and seasonal weather forecasting. Although the atmospheric responses described in this study were the results from an ideal numerical modeling experiment, the lateral boundary condition in the experiment of this study was realistic re-analysis data, JRA-25, which includes various atmospheric fluctuations such as synoptic scale disturbances, monsoon strength, and the remote influences of ENSO. Thus, the problem of estrangement from the actual atmosphere, such as the virtual atmosphere in a coupled atmosphere–ocean model, was less likely to occur. The results of our experiments driven by the re-analysis data would be significant for understanding the mechanism of atmosphere-ocean interaction around Japan. To develop our study, we would like to investigate whether the features of our experiment can be detected in a latest version of re-analysis data with high-resolution SST.

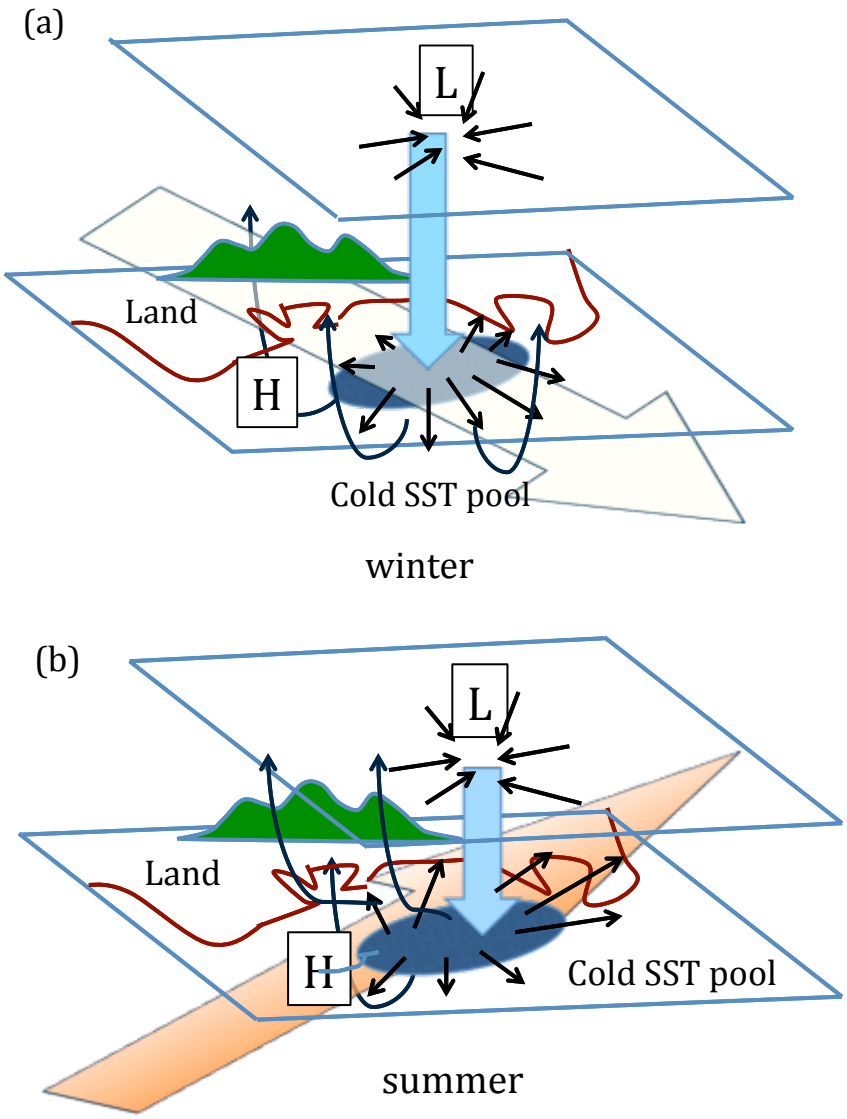

Fig.6.1 Conceptual figure of the wind change due to the Kuroshio LM in (a) winter and (b) summer.

Acknowledgment

I would like to express my best gratitude to all members who have helped to progress the study at Meteorological Research Institute and University of Tsukuba.

Firstly, I would like to express my sincere appreciation to Professor Hiroaki Ueda of the Faculty of Life and Environmental Sciences, University of Tsukuba, inspiration and stimulating advises in the this research. I also wish to express my heartly gratitude to Professors Kuniaki Miyamoto, Takeo Hama, Maki Tsujino, Kenichi Ueno, Hiroshi L. Tanaka, Akio Kito and Youichi Kamae for their valuable comments and careful reading of the manuscript. Special thanks also to Professors Hiroyuki Kusaka and Yasutaka Wakazuki for their valuable comments at the atmospheric division seminar. I also would like to thank Dr. Youichi Tanimoto of Hokkaido University for his insightful and constructive comments. Their detailed comments resulted in many substantial improvements.

Secondly, I would like to offer my special thanks to Drs. Hiroyuki Tsujino, Kazuo Kurihara, Hidetaka Sasaki, Izuru Takayabu of the Meteorological Research Institute, and Dr. Tatsuo Motoi of Meteorological Collage, Dr. Yasuo Sato, former director of environmental and applied meteorological research division of Meteorological research Institute, Professor Hisasi Nakamura, the University of Tokyo, for many helpful discussions regarding the research presented. I am indebted to Dr. Kobayashi, now at the Central Research Institute of Electric Power Industry, who encouraged me to get the doctorate. I deeply thank Dr.Takehiko Satomura, late Professor of Kyoto University, who gave insightful comments and suggestions. I owe my deepest gratitude to Dr. Hideji Kida, late Professor of Kyoto University, and Dr. Takeshi Kawamura, late Professor emeritus at the University of Tsukuba, who gave me an opportunity to start research. I am also grateful to Dr. Norihisa Usui who provided MGDSST datasets. I would like to express my special thanks to the members of “climate laboratory of Prof. Ueda” for their valuable advices and encouragements. I would like to show my great appreciation to Dr. Kazuo Saito, director of forecast research division, Dr. Tomoaki Ose, director of climate research

division, Dr. Seiji Yukimoto, chief of 4th laboratory at climate research division, and the members of climate research division and forecast research division of the Meteorological Research Institute, who cooperated me for the balance of work and university life. I would like to thank Ms. Toshiko Koyari, who supported me to submit a lot of paper works.

Finally, I wish to thank my family, my husband Ahoro, my children Asumu, Seren and Leon Adachi for their patience and warm support during long hours of disruption of family schedules. Special thank to my parents, Yoshinori and Keiko Murazaki, who raised me with love.

This research was supported in part by the MRI special research program “Comprehensive projection of climate change around Japan due to global warming” and supported by the Grant-in-Aid for scientific research #22106009 by the Ministry of Education, Culture, Sports, Science and Technology, Japan.

References

Arakawa, A., and W. H. Schubert, 1974: Interaction of a cumulus cloud ensemble with the large scale environment, Part I. *J. Atmos. Sci*., **31**, 674-701.

Alexander, M. A., I. Bladé, M. Newman, J. R. Lanzante, N-C. Lau, and J. D. Scott, 2002: The atmospheric bridge: The influence of ENSO teleconnections on air–sea interaction over the global oceans. *J. Climate*, **15,** 2205–2231.

Alexandru, A., R. Elia, and R. Laprise, 2007: Internal variability in regional climate downscaling at the seasonal scale. *Mon. Wea. Rev.*, **135**, 3221–3238.

Bond, A.A., and M. F. Cronin, 2008: Regional weather patterns during anomalous air-sea fluxes at the Kuroshio extension observatory (KEO). *J. Climate,* **21**,1680-1697.

Booth, J. F., L. Thompson, J. Patoux, K. A. Kelly, S. Dickinson, 2010: The signature of the midlatitude tropospheric storm tracks in the surface winds. *J. Climate*, **23**, 1160-1174.

Christensen, O. B., J. H. Christensen, B. Machenhauer, and M. Botzet, 1998: Very high-resolution regional climate simulations over Scandinavia—present climate. *J. Climate*, **11**, 3204–3229.

Eastman, J. L., M. B. Coughenour, and R. A. Pielke, 2001: Does grazing affect regional climate?, *J. Hydrometeor*, **2**, 243–253.

Gill, A. E., 1980: Some simple solutions for heat-induced tropical circulation. *Quat. J. Roy. Meteor. Soc.*, **106**, 447-462.

Giorgi, F. and Gary T. Bates, 1989: The climatological skill of a regional model over complex terrain. *Mon. Wea. Rev.*, **117**, 2325–2347.

Giorgi, F. and M. R. Marinucci, 1996: A investigation of the sensitivity of simulated precipitation to model resolution and its implications for climate studies. *Mon. Wea. Rev.*, **124**, 148–166.

Hayasaki, M., R. Kawamura, M. Mori, and M. Watanabe, 2013: Response of extratropical cyclone activity to the Kuroshio large meander in northern winter. *Geophys. Res. Lett.,* **40**, 2851–2855, doi:10.1002/grl.50546.

Hirakuchi, H., and F. Giorgi, 1995: Multiyear present-day and 2 × CO_2 simulations of monsoon climate over eastern Asia and Japan with a regional climate model nested in a general circulation model. *J. Geophys. Res*., **100(D10)**, 21105–21125, doi:10.1029/95JD01885.

Iizuka, S., M. Shiota, R. Kawamura, and H. Hatsu- shika, 2013: Influence of the monsoon variability and sea surface temperature front on the explosive cyclone activity in the vicinity of Japan during northern winter. *SOLA*, **9**, 1−4, doi:10.2151/sola. 2013-001.

Imawaki S., H. Uchida, H. Ichikawa, M. Fukasawa, S. Umatani, and the ASUKA Group, 2001: Satellite altimeter monitoring the Kuroshio transport south of Japan. *Geophys. Res. Lett*., **28**, 17-20.

Ishii, M., A. Shouji, S. Sugimoto, and T. Matsumoto, 2005: Objective analyses of sea-surface temperature and marine meteorological variables for the 20th century using ICOADS and the Kobe Collection. *Int. J. Climatol.,* **25**, 865–879, doi: 10.1002/joc.1169.

Ishikawa, I., H. Tsujino, M. Hirabara, H. Nakano, T. Yasuda, and H. Ishizaki, 2005: Meteorological research Institute community ocean model (MRI.COM) Manual. *Technical reports of the Meteorological Research Institute,* **No. 47**.

Ishizaki, H., and T. Motoi, 1999: Reevaluation of the Takano-Oonishi schemes for momentum advection on bottom relief in ocean models. *J. Atmos. Oceanic Technol*., **16**, 1994-2010.

Ishizaki N., I. Takayabu, M. Oh'izumi, H. Sasaki, K. Dairaku, S. Iizuka, F. Kimura, H. Kusaka, S. A. Adachi, K. Kurihara, K. Murazaki, and K. Tanaka, 2012: Improved performance of simulated Japanese climate with a multi-model ensemble. *J. Meteor. Soc. Japan,* **90**, 235-254.

Isobe. A., 1994: On the Tsushima warm current in the Tsushima strait. *Kaiyo Monthly*, **26**, 802-809 (in Japanese).

Jacobs, G. A., H. T.Perkins, W. J. Teagure, and P. J. Hogan, 2001:Summer transport through the Tsushima-Korea Strait. *J. Geophys. Res*., **106**, 6917-6929.

Japan Meteorological Agency, 2007: Ocean checkup report,

http://www.data.kishou.go.jp/shindan/sougou/html/2.2.2.html.

Japan Meteorological Agency, 2008: Global warming projection, **vol.7.**

Japan Meteorological Agency, 2013: Global warming projection, **vol.8.**

Kato, H., H. Hirakuchi, K. Nishizawa, andF. Giorgi, 1999, Performance of the NCAR RegCM in the simulation of June and January climates over eastern Asia and the high-resolution effect of the model. *J. Geophys. Res.*, **104(D6)**, 6455-6476.

Kato, T., 2009：Representative height of low-level water vapor field to examine the occurrence possibility of heavy rainfall. *East Asia proc. conf. on MCSs and high-impact weather/climate in East Asia*, 343-350.

Kato, T., 2011: Appearance frequency of high equivalent potential temperature field and large water vapor flux at the low level around Japan, H22 Weather forecasting techniques training text, **16**, 71-78 (in Japanese).

Kawabe, M., 1995: Variations of current path, velocity, and volume transport of the Kuroshio in relation with the large meander. *J. Phys. Oceanogr.*, **25**, 3103–3117.

Kawai, H., 1972: Hydrography of the Kuroshio Extension, Kuroshio–its physical aspects. University of Tokyo Press, 252–352.

Kelly, K. A., R. J. Small, R. M. Samelson, B. Qiu, T. M. Joyce, Y-O. Kwon, and M. Cronin, 2010: Western boundary currents and frontal air–sea interaction: Gulf Stream and Kuroshio Extension. *J. Climate*, **23**, 5644–5667.

Kida, H., T. Koide, H. Sasaki, and M. Chiba, 1991: A new approach to coupling a limited area model with a GCM for regional climate simulations. *J. Meteor. Soc. Japan*, **69**, 723-728.

Klein, S. A., D. L. Hartmann, and J. R. Norris, 1995: On the relationships among low-cloud structure, sea surface temperature and atmospheric circulation in the summertime northeast Pacific. *J. Climate*, **8,** 1140–1155.

Kondo, J., 1975: Air-sea bulk transfer coefficients in diabatic conditions. *Boundary Layer Meteorol.*, **9**, 91–112.

Kunoki, S., A. Manda, Y.-M. Kodama, S. Iizuka, K. Sato, I. Fathrio, T. Mitsui, H. Seko, Q. Moteki, S. Minobe, and Y. Tachibana, 2015: Oceanic influence on the Baiu frontal zone in the East China Sea. *J. Geophys. Res. Atmos*., **120**, 449–463, doi:10.1002/2014JD022234.

Kuragano, T., T. Umeda, Y. Kurihara, and T. Sakurai, 2007: Long-term change of sea surface temperatures in the global ocean using COBE-SST. *Sokko-jiho*, **74**, S19-S31.

Kurihara, Y., T. Sakurai, and T. Kuragano, 2006: Global daily sea surface temperature analysis using data from satellite microwave radiometer, satellite infrared radiometer and in-situ observations. *Sokko-jiho*, **73**, S1-S18 (in Japanese).

Kuwano-Yoshida, A., B. Taguchi, and S.-P. Xie, 2013: Baiu rainband termination in atmospheric and coupled atmosphere–ocean models. *J. Clim.*, **26 (24)**, 10,111–10,124, doi:10.1175/JCLI-D-13-00231.1.

Kwon, Y.-O., M. A. Alexander, N. A. Bond, C. Frankignoul, H. Nakamura, B. Qiu, and L. A. Thompson, 2010: Role of the Gulf Stream and Kuroshio–Oyashio systems in large-scale atmosphere–ocean interaction: A review. *J. Climate*, **23**, 3249–3281,

doi: http://dx.doi.org/10.1175/2010JCLI3343.1.

Lacis, A. A., and J. E. Hansen, 1974: A parameterization for the absorption of solar radiation in the Earth's atmosphere. *J. Atmos. Sci*., **31**, 118-133.

Large, W. G. and S. Pond, 1982: Sensible and latent heat flux measurements over the ocean. *J.phys. Oceanogr.,* **12**, 464-482.

Leonard, B. P., 1979: A stable and accurate convective modeling procedure based upon quadratic upstream interpolation. *J. Comput. Methods Appl. Mech., Eng*., **19**, 59-98.

Leonard, B. P., M. K. MacVean, and A. P. Lock, 1993, Positivity-preserving numerical schemes for multidimenensional advection. *NASA Tech. Memo.*, 106055, ICOMP-93-05 62pp.

Liang, X-Z., H. I. Choi, K. E. Kunkel, Y. Dai, E. Joseph, J. X. L. Wang, and P. Kumar, 2005: Surface Boundary Conditions for Mesoscale Regional Climate Models. *Earth Interact*, **9**, 1–28, doi: 10.1175/EI151.1.

Lindzen, R. S., and R. S. Nigam, 1987: On the role of sea surface temperature gradients in forcing low level winds and convergence in tropics. *J. Atmos. Sci*., **44,** 2418-2436.

Liu, Z., Y. Liu, L. Wu, and R. Jacob, 2007: Seasonal and long-term atmospheric responses to reemerging North Pacific Ocean variability: A combined dynamical and statistical assessment. *J. Climate*, **20,** 955–980.

Liu, Z., and M. Alexander, 2007: Atmospheric bridge, oceanic tunnel and global climatic teleconnections. *Rev. Geophys.*, **45,** RG2005. doi:10.1029/2005RG000172.

Liu, J.-W., S.-P. Zhang, S.-P. Xie, 2013: Two types of surface wind response to the East China Sea Kuroshio front. *J. Climate,* **26**, 8616–8627,

doi: http://dx.doi.org/10.1175/JCLI-D-12-00092.1.

Liu, Y., F. Giorgi, and W. M. Washington, 1994: Simulation of summer monsoon climate over East Asia with an NCAR regional climate model. *Mon. Wea. Rev.*, **122**, 2331–2348.

Matsuno, T., 1966: Quasi-geostrophic motions in the equatorial area. *J. Meteoro. Soc. Japan*, **44**, 24-42.

Mellor, G.L., and A.F. Blumberg, 2004: Wave breaking and ocean surface layer thermal response. *J. Phys. Oceanogr*., **34** 693-698.

Mellor, G. L., and T. Yamada, 1982: Development of a turbulence closure model for geophysical fluid problems. *Rev. Geophys. Space Phys*., **20**, 851-875.

Ministry of Land, Infrastructure and Transport and Tourism), 2014: Water in Japan, 7th World Water Forum 2015.

http://www.mlit.go.jp/mizukokudo/mizsei/mizukokudo_mizsei_tk2_000008.html.

Minobe, A., A. Kuwano-Yoshida, N. Komori, S.-P. Xie, and R.J. Small, 2008: Influence of the Gulf Stream on the troposphere. *Nature*, **452**, 206-209.

Miyama, T., M. Nonaka, H. Nakamura, and A. Kuwano-Yoshida, 2012: A striking early-summer event of a convective rainband persistent along the warm Kuroshio in the East China Sea. Tellus A, **64**, 18962, doi:10.3402/tellusa.v64i0.18962.

Murazaki, K., H. Sasaki, H. Tsujino, I. Takayabu, Y. Sato, H. Ishazaki, K. Kurihara, 2005: Climatic change projection for the ocean around Japan using a high-resolution coupled atmosphere-ocean regional climate model. *SOLA*, **1**, 101-104.

Murazaki, K., K. Kurihara, and H. Sasaki, 2010: Dynamical downscaling of JRA-25 precipitation over Japan using the MRI-regional climate model. *SOLA*, **6**, 141-144.

Murazaki, K., H. Tsujino, T. Motoi, K. Kurihara, 2015: Influence of the Kuroshio large meander on the climate around Japan based on a regional climate model. *J. Meteor. Soc. Japan*, **93**, No.2, 161-179.

Nakamura, H., A. Nishina, and S. Minobe, 2012: Response of storm tracks to bimodal Kuroshio path states south of Japan. *J. Climate*, **25**, 7772–7779, doi:10.1175/JCLI-D-12- 00326.1.

Nakamura, H., T. Sampe, Y. Tanimoto, and A. Shimpo, 2004: Observed associations among storm tracks, jet streams and midlatitude oceanic fronts. Earth's Climate: The Ocean–Atmosphere Interaction*, Geophys. Monogr.,* **147**, Amer. Geophys. Union, 329–346.

Nakamura, H., T. Sampe, A. Goto, W. Ohfuchi, and S-P. Xie, 2008: On the importance of midlatitude oceanic frontal zones for the mean state and dominant variability in the tropospheric circulation. *Geophys. Res. Lett.*, **35,** L15709. doi:10.1029/2008GL034010.

Nakamura, T., T. Toyoda, Y. Ishikawa, and T. Awaji, 2004: Tidal mixing in the Kuril Straits and its impact on ventilation of the North Pacific Ocean. *J. Oceanogr.*, **60**, 411-422.

Ninomiya, K., 1984: Characteristics of Baiu front as a predominant sub-tropical front in the summer Northern Hemisphere. *J. Meteor. Soc. Japan*, **62**, 880–894.

Ninomiya, K. and T. Akiyama, 1992: Multi-scale features of Baiu, the summer monsoon over Japan and the east Asia. *J. Meteor. Soc. Japan*, **70**, 467-495.

Nonaka, M., and S.-P. Xie, 2003: Covariations of sea surface temperature and wind over the Kuroshio and its extension: Evidence for ocean-to-atmosphere feedback. *J. Climate*, **16**, 1404–1413, doi:10.1175/1520-0442.

Nonaka, M., H. Nakamura, Y. Tanimoto, T. Kagimoto, and H. Sasaki, 2006: Decadal variability

in the Kuroshio–Oyashio Extension simulated in an eddy-resolving OGCM. *J. Climate*, **19,** 1970–1989.

Numerical Prediction Division/ Japan Meteorological Agency, 1997: Outline of the operational numerical weather prediction of the Japan Meteorological Agency, 126pp.

Onogi K., J.Tsutsui, H. Koide, M. Sakamoto, S. Kobayashi, H. Hatsushika, T. Matsumoto, N. Yamazaki, H. Kamahori, K. Takahashi, S. Kadokura, K. Wada,.K. Kato, R. Oyama, T. Ose, N. Mannoji, and R. Taira, 2007: The JRA-25 Reanalysis. *J. Meteor. Soc. Japan*, **85**, 369 - 432.

Pidwirny, M., 2006: Surface and Subsurface Ocean Currents: Ocean Current Map. *Fundamentals of Physical Geography, 2nd Edition,*

http://www.physicalgeography.net/fundamentals/8q_1.html.

Pielke, R. A., W. R. Cotton, R. L. Walko, C. J. Tremback, W. A. Lyons, L. D. Grasso, M. E. Nicholls, M. D. Moran, D. A. Wesley, T. J. Lee, and J. H. Copeland, 1992: A comprehensive meteorological modeling system- RAMS. *Meteor. Atmos. Phys.*, **49**, 69–91.

Qiu, B., 2003: Kuroshio Extension variability and forcing for the Pacific decadal oscillations: Responses and potential feedback. *J. Phys. Oceanogr.*, **33,** 2465–2482.

Sampe, T., and S.-P. Xie, 2010: Large-scale dynamics of the meiyu–baiu rainband: Environmental forcing by the westerly jet. *J. Climate*, **23**, 113–134.

Sasaki, H., H. Kida, T. Koide, and M. Chiba, 1995: The performance of long-term integration of a limited area model with the spectral boundary coupling method. *J. Meteor. Soc. Japan*, **73**, 165–181.

Sasaki, H., Y. Sato, K. Adachi, and H. Kida, 2000: Performance and evaluation of the MRI regional climate model with the spectral boundary coupling method, *J. Meteor. Soc. Japan,* **78**, 477–489.

Sasaki, H., K. Kurihara, I. Takayabu, K. Murazaki, Y. Sato, H. Tsujino, 2006: Preliminary results from the coupled atmosphere-ocean regional climate model at the Meteorological Research Institute. *J. Meteor. Soc. Japan,* **84**, 389–403.

Sasaki Y. N., S. Minobe, T. Asai, M. Inatsu, 2012: Influence of the Kuroshio in the East China Sea on the early summer (Baiu) rain. *J. Climate,* **25(19)**, 6627–6645,

doi:10.1175/jcli-d-11-00727.1.

Sato, Y., S. Yukimoto, H. Tsujino, H. Ishizaki, and A. Noda, 2006: Response of North Pacific

ocean circulation in a Kuroshio-resolving ocean model to an Arctic Oscillation (AO)-like change in Northern Hemisphere atmospheric circulation due to greenhouse-gas forcing. *J. Meteor. Soc. Japan*, **84**, 295-309.

Skamarock, W. C., J. B. Klemp, J. Dudhia, D. O. Gill, D. M. Barker, M. G. Duda, X.-Y. Huang, W. Wang, and J. G. Powers, 2008: A description of the advanced research WRF Version 3. *NCAR technical note*, NCAR/TN- 475+STR.

Solomon, S., D. Qin, M. Manning, R.B. Alley, T. Berntsen, N.L. Bindoff, Z. Chen, A. Chidthaisong, J.M. Gregory, G.C. Hegerl, M. Heimann, B. Hewitson, B.J. Hoskins, F. Joos, J. Jouzel, V. Kattsov, U. Lohmann, T. Matsuno, M. Molina, N. Nicholls, J. Overpeck, G. Raga, V. Ramaswamy, J. Ren, M. Rusticucci, R. Somerville, T.F. Stocker, P. Whetton, R.A. Wood and D. Wratt, 2007: Technical Summary. In: Climate Change 2007: The Physical Science Basis. Contribution of Working Group I to the Fourth Assessment Report of the Intergovernmental Panel on Climate Change [Solomon, S., D. Qin, M. Manning, Z. Chen, M. Marquis, K.B. Averyt, M. Tignor and H.L. Miller (eds.)]. *Cambridge University Press,* Cambridge, United Kingdom and New York, NY, USA.

St. Laurent, L. C., H. L. Simmons, and S. R. Jayne, 2002: Estimating tidally driven mixing in the deep ocean. *Geophys. Res. Lett.*, **29**, 2106-2100, doi:10.1029/2002GL015633.

Stommel H., 1948: The westward intensification of wind-driven ocean currents, *Transactions, American Geophysical union*, **29**, 2, 202-206.

Sugi, M., K. Kuma, K. Tada., K. Tamiya, N. Hasegawa, T. Iwasaki, S. Yamada, and T. Kitade, 1990: Description and performance of the JMA operational global spectral model (JMA-GSM88). *Geophys. Mag.,* **43**, (3) 105–130.

Takatsuki, Y., T. Kuragano, T. Shiga, Y. Bungi, H. Inoue, H. Fujiwara, M. Ariyoshi, 2007: Long-term trends in sea surface temperature adjustment to Japan. *Sokko-jiho*, **74**, S33-S84.

Takayabu, I., H. Kato, K. Nishizawa, S. Emori, K. Dairaku, Y. Sato, H. Sasaki, and K. Kurihara, 2004: Simulation of Asian climate by using regional climate models nested in global circulation models. *Proc.2004 Symposium on water resource and Its Variability in Asia in the 21st Century*, 94-97.

Takikawa, T., J.-H. Yoon, and K.-D. Cho 2003:Tidal currents in the Tsushima straits estimated from ADCP data by ferryboat. *J. Oceanogr.*, **59**, 37-47.

Tanimoto, Y., S-P. Xie, K. Kai, H. Okajima, H. Tokinaga, T. Murayama, M. Nonaka, and H. Nakamura, 2009: Observations of marine atmospheric boundary layer transitions across the summer Kuroshio Extension. *J. Climate*, **22,** 1360–1374.

Tokinaga, H., Y. Tanimoto, S-P. Xie, T. Sampe, H. Tomita, and H. Ichikawa, 2009: Ocean frontal effects on the vertical development of clouds over the western North Pacific: In situ and satellite observations. *J. Climate*, **22,** 4241–4260.

Taylor, K. E., 2001: Summarizing multiple aspects of model performance in a single diagram. *J. Geophys. Res.*, **106**, 7183–7192.

Tsujino, H., and T. Yasuda, 2004: Formation and circulation of mode waters of the north pacific in a high-resolution GCM. *J. Phys. Oceanogr,,* **34**, 399-415.

Tsujino, H., N. Usui, and H. Nakano, 2006: Dynamics of Kuroshio path variations in a high-resolution GCM. *J. Geophys. Res.*, **111**, C11001, doi:10.1029/2005JC003118.

Tsujino, H., S. Nishikawa, K. Sakamoto, N. Usui, H. Nakano, G. Yamanaka, 2013: Effects of large-scale wind on the Kuroshio path south of Japan in a 60-year historical OGCM simulation. *Clim. Dyn.,* **41**, 2287-2318, doi:10.1007/s00382-012-1641-4.

Trenberth, K. E., G. W. Branstator, D. Karoly, A. Kumar, N-C. Lau, and C. Ropelewski, 1998: Progress during TOGA in understanding and modeling global teleconnections associated with tropical sea surface temperatures. *J. Geophys. Res.*, **103(C7)**, 14291–14324.

Ueda, H., T. Yasunari, and R. Kawamura, 1995: Abrupt seasonal change of large-scale convective activity over the western Pacific in the northern summer. *J. Meteor. Soc. Japan*, **73**, 795–809.

Ueda, H, 2014, Climate System Study –Global monsoon perspective–. *University of Tsukuba Press*, 217pp.

Usui, N., H. Tsujino, Y. Fujii, and M. Kamachi, 2008: Generation of a trigger meander for the 2004 Kuroshio large meander. *J. Geophys. Res.*, **113**, C01012,

doi:10.1029/2007JC004266.

Usui, N., H. Tsujino, and H. Nakano, 2013: Long-term variability of the Kuroshio path south of Japan. *J Oceanogr.,* **69**, 647–670, doi: 10.1007/s10872-013-0197-1.

Wallace, J.M., and T. P. Mitchell, and C. Deser, 1989: The influence of sea surface temperature on sea surface wind in the eastern equatorial Pacific: Seasonal and interannual variability. *J. Climate*, **2**, 1492-1499.

Walsh, K. and J. L. McGregor, 1995: January and July climate simulations over the Australian region using a limited-area model. *J. Climate*, **8**, 2387–2403.

Xie, S.-P., J. Hafner, Y. Tanimoto, W. T. Liu, H. Tokinaga, a,d H. Xu, 2002: Bathymetric effect on the winter sea surface temperature and climate of the Yellow and East China Seas.

Geophys. Res. Lett., **29**, doi:10.1029/2002GL0158.

Xu, H., H. Tokinaga, and S.-P. Xie, 2010: Atmospheric effects of the Kuroshio large meander during 2004–05. *J. Climate*, **23**, 4704–4715.

Xu, H., M. Xu, S.-P. Xie, and Y. Wang, 2011: Deep atmospheric response to the spring Kuroshio current over the East China Sea. *J. Climate,* **24**, 4959–4972.

Yoshiike, S., and R. Kawamura, 2009: Influence of wintertime large-scale circulation on the explosively developing cyclones over the western North Pacific and their downstream effects. *J. Geophys. Res.*, **114,** D13110, doi:10.1029/2009JD011820.

Yoshimura, K., and M. Kanamitsu, 2009: Specification of external forcing for regional model integrations. *Mon. Wea. Rev.*, **137**, 1409–1421. doi: 10.1175/2008MWR2654.1.

Yoshino, M., 1968: Kikougaku, *Chijinshokan*, pp258 (in Japanese).

Yukimoto, S., A. Noda, A. Kitoh, M. Sugi, Y. Kitamura, M. Hosaka, K. Shibata, S. Maeda, and T. Uchiyama, 2001: The new meteorological research institute coupled GCM (MRI-CGCM2) -Model climate and variability-. *Pap. Meteor. Geophys*., **51**, 47–88.

Yukimoto, S., H. Yoshimura, M. Hosaka, T. Sakami, H. Tsujino, M. Hirabara, T. Y. Tanaka, M. Deushi, A. Obata, H. Nakano, Y. Adachi, E. Shindo, S. Yabu, T. Ose, A. Kitoh, 2011: Meteorological Research Institute-Earth System Model Version 1 (MRI-ESM1) ― Model Description. *Technical Reports of the Meteorological Research Institute,* **64**, 1-96.

Zhou, Y.,S. Gao, and S-S.P. Shen, 2004: A diagnostic study of formation and structures of the Meiyu front system over East Asia. *J. Meteor. Soc. Japan*, **82**, 1565-1576.

Publication List

Peer reviewed articles

(The mark * indicates the papers based on the doctorate thesis.)

1. Sato, J., H. Sasaki, K. Adachi, Performance and Its Evaluation of the MRI Long Range Transport Model For ATMES-II Phase of ETEX. *J. Meteor. Soc. Japan*, **77**,1161-1176.

2. Sasaki, H., Y. Sato, K. Adachi, H. Kida, 2000: Performance and Evaluation of the MRI Regional Climate Model with the Spectral Boundary Coupling Method. *J. Meteor. Soc. Japan*, **78**, 477-489.

3. Murazaki, K., M. Chiba, H. Kida, 2002: Interhemispheric mass exchange due toideal tropical Hadley circulations simulated by an axially symmetric 2-D global model. *Pap. Meteor. Geophys*., **52**, 67-80.

4. Kurihara, K., K. Ishihara, H. sasaki, Y. Fukuyama, H. Saitou, I. Takayabu, K. Murazaki, Y. Sato, S. Yukimoto, A. Noda, 2005: Projection of climatic change over Japan due to global warming by High-Resolution Regional Climate Model in MRI. *SOLA,* **1**, 97-100.

5*. Murazaki, K., H. Sasaki, H. Tsujino, I. Takayabu, Y. Sato, H. Ishazaki, K. Kurihara, 2005: Climatic change projection for the ocean around Japan using a high-resolution coupled atmosphere-ocean regional climate model. *SOLA*, **1**, 101-104.

6. Murazaki, K, P. Hess, 2006: How does climate change contribute to surface ozone change over the United States?*, J. Geophys. Res.*, **111**, D05301.

7. Sasaki, H., K. Kurihara, I. Takayabu, K. Murazaki, Y. Sato, H. Tsujino, 2006, Preliminary results from the Coupled Atmosphere-Ocean Regional Climate Model at the Meteorological Research Institute. *J. Meteor. Soc. Japan*, **84**, 389-403.

8*. Murazaki, K., K. Kurihara, H. Sasaki, 2010: Dynamical Downscaling of JRA-25 Precipitation over Japan Using the MRI-Regional Climate Model. *SOLA*, **6**, 141-144.

9. Ishizaki, N. N., I. Takayabu, M. Oh'izumi, H. Sasaki, K. Dairaku, S. Iizuka, F. Kimura, H. Kusaka, S.A. Adachi, K. Kurihara, K. Murazaki, K. Tanaka, 2012: Improved Performance of Simulated Japanese Climate with a Multi-Model Ensemble. *J. Meteor. Soc. Japan*, **90**, 235-254.

10*. Murazaki, K, H. Tsujino, T. Motoi, K. Kurihara, 2015: Influence of the Kuroshio large meander on the climate around Japan based on a regional climate model. *J. Meteor. Soc. Japan*, **93**, No.2, 161-179.

Unrefereed articles

11. Adachi, K., H. Sasaki, Y. Sato, 1998 ; Climate projection experiment using a limited area mode, 1998: *14th IGBP/GAIM meeting, IGBP/GAIM communication* (in Japanese).

12. Sato, Y., H. Sasaki, K. Adachi, A. Noda, S. Yukimoto, 1999: A 2xCO2 regional climate prediction experiment over Japan in winter with an MRI regional climate model, 1999, *IUGG 1999*, Birmingham, U. K., B. 299.

13. Murazaki, K., H. Sasaki, Y. Sato, 2000: Climate simulations over Japan in summer with an MRI regional climatemodel: Present day and 2xCO2 experiments, *Preprint Volume of the 11th Symposium on Global Change Studies*, 9-14 January 2000, Longbeach, Cal., 332-335

14. Sato, Y. and MRI regional climate modeling group, 2001: Present view on Development of MRI Regional Climate Models. IPRC, Univ. of Hawai, *Proceedings of the First IPRC Regional Climate Modeling*, p6, http://iprc.soest.hawaii.edu/meetings/workshops/abstracts.pdf.

15.Murazaki, K., K. Kurihara, H. Sasaki, I. Takayabu, T. Uchiyama, 2008: A regional Climate simulation over Japan nested with JRA-25. *Third WCRP International Conference on Reanalysis*, 2008, P20-22.

16. Murazaki, K., 2012: Evaluation of the Temperature Predictive Accuracy of Winter Hokuriku by JMA-NHM. *2nd International Workshop on Nonhydrostatic Numerical Models*. 87-88.

Appendix

Abbreviation list

AMeDAS Automated meteorological data acquisition system

COBE SST Central *in situ* observation-based estimates Sea surface temperature

CGCM Coupled general circulation model

CRCM Coupled atmosphere-ocean regional climate model

CRIEPI Central Research Institute of the Electric Power Industry

ECS East China Sea

ENSO **El Niño-Southern Oscillation**

EPT Equivalent potential temperature

GCM General circulation model

JMA Japan Meteorological Agency

JRA-25 Japanese re-analysis for 25 years

KE Kuroshio extention

LM Large meander (of Kuroshio)

LBM Linear baroclinic model

MABL Marine atmospheric boundary layer

MGDSST Merged satellite and in situ data global daily SST

NIED National research Institute for Earth Science and Disaster prevention

NPD Numerical Prediction Division

NPOGCM North Pacific Ocean general circulation model

MRI Meteorological research Institute

MRI-CGCM2 Meteorological research Institute- coupled general circulation model v.2

MRI-ESM Meteorological research Institute-Earth system model.

PCR Precipitation frequency coverage rate

Qconv Vertical integrated moisture flux convergence

RAMS Regional atmospheric modeling system

RCM Regional climate model

RCM20 20km-resolution regional climate model

RMSE Root mean square error

SAT Surface air temperature

SBC Spectral boundary coupling

SP Straight path (of Kuroshio)

SST Sea surface temperature

Steep $|\nabla_h \theta_e|$ horizontal EPT gradients exceeding 0.1 K km^{-1}

WBC Western boundary currents

WRF Weather research and forecasting model

Experiments list

	JRA-run	MGDSST-run	CGCM-run	CRCM-run	OGCM-run
Lateral boundary	JRA-25	JRA-25	none	RCM60 nested with CGCMv2.2	JRA-25
Lower boundary	JRA-SST	MGDSST	none	coupling NPOGCM	NPOGCMv2 driven by the JRA-25
SST resolution	about 1°	0.25°	lon: 2.5° , lat: 0.5° – 2°	lon 1/4° , lat1/6 °	1/10° (around Japan)
Internal model	RCM20	RCM20	CGCMv2.2	RCM20	RCM20
Experimental period	1979-2004	2000.1.1-12.31	1990-2070	present; 1991-2000, future; 2061-2070	1985-2004
One-way or two way	one-way	one-way	two-way	two-way	one-way
Referred chapter	3.1, 4 and 5	3.2	3.3	3.3	4 and 5